Politecnico di Milano
Scuola di Ingegneria Industriale e dell’Informazione
Corso di Laurea Magistrale in Ingegneria Fisica
Dipartimento di Fisica

TOWARDS A MAGNETORESISTIVE PLATFORM FOR NEURAL SIGNAL RECORDING

Relatore: Daniela Petti
Correlatore: Parikshit Pratim Sharma

Tesi di Laurea di:
Filippo D’Ercoli
837010

Anno Accademico 2015-2016

List of Figures

List of Tables

Sommario

Lo sviluppo di sistemi di fabbricazione di film sottili ha permesso la diffusione e l'utilizzo estensivo di materiali nanostrutturati. Con la scoperta della magnetoresistenza gigante nel 1988, i fenomeni magnetoresistivi hanno iniziato a diventare il nucleo di diversi dispositivi spintronici. Tra questi, i sensori magnetoresistivi sono particolarmente adatti per applicazioni biologiche grazie alla loro elevata sensibilità e alla facilità di integrazione in piattaforme compatte.

Questo lavoro si inserisce nel contesto del progetto UMANA, il cui obiettivo è l'applicazione di sensori magnetoresistivi per il rilevamento dei segnali originati dai potenziali d'azione in colture neuronali *in-vitro*. Lo schema di rilevamento si basa sulla misura dei campi magnetici generati dalle correnti ioniche associate alla propagazione dei potenziali d'azione. In confronto ai metodi convenzionali, l'alta sensibilità, la risoluzione spaziale e la bassa invasività dei sensori magnetoresistivi li rende uno strumento promettente per queste indagini.

La prima parte di questa tesi è dedicata allo studio di differenti sensori con lo scopo di determinare quello con le migliori prestazioni, il quale in seguito a ulteriori ottimizzazioni potrà essere usato nell'ambito del progetto UMANA. In questa parte vengono descritte le analisi di rumore sui sensori e le misure di rilevamento del campo magnetico generato da linee di corrente, costruite direttamente sopra il sensore al fine di simulare le correnti neuronali.

Nella seconda parte, vengono affrontante gli esperimenti biologici. Viene quindi descritta la realizzazione di una piattaforma per la registrazione dei segnali neuronali che provengono da fettine di ippocampo ottenute da ratti da laboratorio e infine vengono riportati i risultati degli esperimenti *in-vitro*.

Per riassumere, durante questa tesi sono stati affrontati i seguenti argomenti:

- Microfabbricazione di sensori basati su giunzioni a effetto tunnel magnetico (MTJ) tramite deposizione con *magnetron sputtering* e litografia ottica.
- Caratterizzazione di sensori tramite misure magnetoresistive.
- Misure di rumore su sensori magnetoresistivi utilizzando un analizzatore a cross-correlazione.
- Rivelazione della propagazione di corrente in linee d'oro fabbricate tramite litografia ottica sopra i sensori per simulare le correnti neuronali.
- Validazione di una piattaforma elettronica dedicata per misure di campo magnetico a basso rumore con sensori magnetoresistivi.
- Esperimenti *in-vitro* su fettine di ippocampo di ratto.

Il lavoro sperimentale è stato eseguito con il gruppo NaBiS al Centro PoliFab del Dipartimento di Fisica del Politecnico di Milano sotto la supervisione della Dottoressa Daniela Petti e del Professore Riccardo Bertacco, responsabile del gruppo. L'elettronica integrata utilizzata per la rivelazione dei segnali è stata sviluppata dal gruppo I3N del

Dipartimento di Elettronica, Informazione e Bioingegneria of the Politecnico che ha anche condotto le misure di rumore. Gli aspetti biologici sono stati gestiti dal Centro per le Neuroscienze e le Tecnologie Sinptiche dell'IIT di Genova che si è occupato della preparazione delle fettine di cervello.

Questa tesi è organizzata in 5 capitoli. Il primo fornisce una panoramica sui sensori magnetoresistivi e sulle loro applicazioni biologiche. Il secondo capitolo esamina i principi fisici alla base dei sensori analizzati. Il terzo capitolo illustra i metodi sperimentali utilizzati nel corso di questo lavoro di tesi. Nel quarto capitolo, quattro differenti sensori sono analizzati e comparati in termini di prestazioni di rumore e minimo campo misurabile. Nell'ultimo capitolo, sono riportati i risultati degli esperimenti *in-vitro*, insieme alla procedura di fabbricazione dei sensori MTJ impiegati.

Abstract

The evolution in the fabrication of thin films allowed the development of nanostructured systems and, with the discovery of giant magnetoresistance in 1988, magnetoresistive phenomena started to become the core of a variety of spintronic devices. Among them, magnetoresistive sensors are particularly suited for biosensing applications due to their high sensitivity and ease of integration in compact platforms.

This thesis work fits in the framework of UMANA project, whose goal is the application of magnetoresistive sensors to the detection of the signal arising from the action potential generated by *in-vitro* neuronal cultures. The detection scheme relies on the measurement of the magnetic field generated by the ionic currents associated to the propagation of action potentials. With respect to conventional methods, their high sensibility, spatial resolution and low invasiveness make them a promising device for such investigations.

The first part of the thesis is devoted to the study of different sensors, in order to determine the one with the best performances, suitable for further optimization, to be employed for the UMANA project. In this part, noise measurements are described. In addition, the detection of the magnetic field generated by current lines grown above the sensors to simulate the neuronal currents is presented.

In the second part, the biological issues related to this experiment are discussed. Then, the realization of a platform for the recording of neuronal signals arising from rat hippocampal slices is reported and the results from the *in-vitro* experiments are reviewed.

To summarize, the following topics have been addressed during this thesis work:

- Microfabrication of MTJ (Magnetic Tunneling Junction)-based sensors through magnetron sputtering deposition and optical lithographic patterning.
- Sensors characterization through magnetoresistance measurements.
- Noise measurement on magnetoresistive sensors using a cross-correlation spectrum analyzer.
- Detection of the propagation of a current across current lines fabricated through optical lithography on top of the sensors, in order to simulate the biological currents.

- Validation of a dedicated electronic platform for low-noise measurements of magnetic field with MR sensor.
- *In-vitro* experiments on rat hippocampal slices.

The experimental work was carried out with the NaBiS group at the PoliFab Center of Dipartimento di Fisica of the Politecnico di Milano under the supervision of Doctor Daniela Petti and Professor Riccardo Bertacco, responsible for the group. The integrated electronics employed for the signal detection has been developed by the I3N group of the Dipartimento di Elettronica, Informazione e Bioingegneria of the Politecnico di Milano which led also the noise measurements. The biological aspects of the work were dealt with by IIT’s Center

for Synaptic Neuroscience and Technology of Genova, which took care of the preparation of rat hippocampal slices.

This thesis is organized in 5 chapters. The first chapter gives an overview on magnetoresistive sensors and their biological applications. The second chapter reviews the physical principles behind the sensors employed. The third chapter explains the experimental methods employed during this thesis work. In the fourth chapter, four different sensors are analyzed and compared in term of noise performances and minimum detectable field. In the last chapter, the results of the *in-vitro* experiments are reported, along with the fabrication procedure of the employed MTJ sensors.

Table of Contents

Chapter 1: Introduction

This experimental master thesis deals with the biological applications of magnetoresistive sensors, focusing on their employment in brain activity sensing. After a brief description of the evolution of magnetoresistive devices, this introduction gives an overview on the state of the art in biosensing technology, illustrating the context and motivations of this work. Finally, an outline of the topics presented in each section of the thesis is given.

1.1 Development and applications of magnetoresistance in magnetic multilayers

In the past years, the development of processes able to grow thin films with well-controlled thickness (as low as few Å), driven by the semiconductor industry, allowed the spread of nanotechnology applications. The discovery of giant magnetoresistance by Fert and Grunberg in 1988 gave birth to Spintronics, which consist in the generation and manipulation of spin-polarized electrons in magnetic multilayered thin-film structures. These composite materials can act as extremely sensitive magnetic field sensors, because their electrical resistance changes in presence of magnetic fields by factors much larger than conventional magnetic materials. Magnetoresistive (MR) sensors, with their tunable response and adjustable operation range [1], are the ideal candidates for room temperature, small footprint and cost-effective applications at the pico to milli tesla (10^{-12} to 10^{-3} T) range. Field sensing can be done in an extremely small, lithographically-patterned area, reducing size and power consumption requirements and thus being suitable for array applications. Multiple MR sensors can be electronically addressed and multiplexed with on-board electronics. This thin film technology is compatible with standard silicon integrated circuit (IC) technology, allowing for large scale fabrication and close-packed implementations, ideal for portable solutions. Nowadays, several commercial products using MR sensors provide high performance at a reasonable cost.

A newly-arising interesting MR application is brain activity sensing, where field signals are of very low intensity and at low-frequency (nT-fT range, below 1 kHz), requiring sensing devices with challenging detectivity limits, at room temperature. Some major breakthroughs have already been achieved, leading the way to portable neural activity sensing [2], [3].

1.1.1 Magnetoresistive mechanism

Magnetoresistance is the change in the electrical resistivity of a material under the influence of an external magnetic field. The first observation of such effect was carried out in 1856 by Lord Kelvin, who noticed a change in the resistance of Ni and Fe according to the orientation of the applied magnetic field with respect to the direction of the current flow. The physical origin of such effect, the Anisotropic Magnetoresistance (AMR), which is characteristic of transition ferromagnetic materials, lies in the spin-orbit coupling, reflecting the interaction between the spin of the conduction electrons and the crystal lattice. As the magnetization rotates, the conduction electrons undergo a different amount of scattering when traversing the lattice; macroscopically this effect is a change in the electrical resistance of the material. The change in the resistance, at room temperature, due to AMR is about 5% for NiFe and CoFe bulk alloys [4] and lower for patterned thin films (~2%) [5], due to additional scattering, leading spin flip. The low magnitude of the AMR effect and its intrinsic bulk nature were the major drawbacks of AMR in technological challenging applications and these are the main reasons why sensors based on this effect have been gradually replaced by Giant Magnetoresistance (GMR) and Tunneling Magnetoresistance (TMR) devices.

The advancements in thin film deposition techniques led to the development of a new class of devices based on GMR. This effect, discovered in 1988, is observed in multilayered thin-film structures composed of alternating ferromagnetic and non-magnetic layers. It consists in a change in the electrical resistance determined by the spin-dependent scattering at the interfaces of the multilayer depending on whether the magnetizations of consecutive ferromagnetic layers are parallel or anti-parallel [6]. The GMR effect was first observed in Fe/Cr multilayers in the so called current-in-plane configuration (CIP), i.e. with a current flowing parallel to the multilayer interfaces [7]. In Fe/Cr multilayers (Figure 1.1(a)), with no applied field, the magnetizations of adjacent ferromagnetic layers are aligned antiferromagnetically due to the interlayer coupling through the Cr spacer, leading to an increased scattering and thus to a higher resistance [6]. Applying a sufficiently large external magnetic field, the magnetizations become aligned and thus a low resistance state is reached due to the lower scattering at the interfaces. Nowadays, GMR values up to around 20% are obtained at room temperature in optimized spin-valve structures [8].

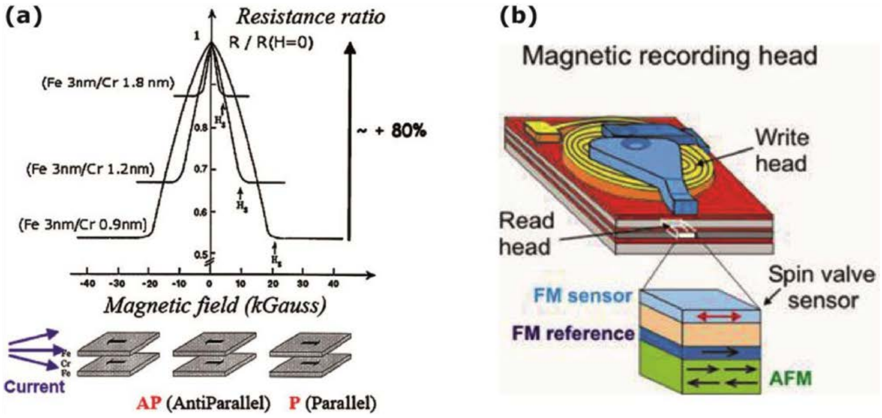

Figure 1.1: *(a) First observation of GMR effect in Fe/Cr multilayers at 4.2 K. Adapted from [6]. (b) Spin-valve structure as a magnetic field sensor in the read-head of magnetic hard drives.*

As in the GMR multilayer, spin-valve devices consist of two ferromagnetic layers separated by a non-magnetic spacer, but in this case, the magnetization of one layer is fixed through exchange bias coupling with an antiferromagnet [9], while the other is free to rotate with the external magnetic field. The most effective early application of GMR devices was as magnetic field sensors in the read head of hard disks (Figure 1.1(b)) replacing AMR heads, which led to a substantial increase in the density of stored information [10].

Before the discovery of the GMR effect, it was already known that the electrical resistance of a Magnetic Tunnel Junction (MTJ) depends on the relative orientation of its ferromagnetic layers, similarly to GMR [11]. This effect is called Tunneling Magnetoresistance (TMR) and has a different physical origin from the GMR effect. It occurs in junctions consisting of two ferromagnetic electrodes (FM) separated by a thin insulating spacer (I), FM/I/FM-like structure. In these structures the electric current flows perpendicular to the layer plane (current perpendicular to plane, CPP configuration). The TMR effect is a result of the spin-dependent tunneling probability. If the spacer is thin enough, upon the application of a potential difference across the junction, the electrons at the Fermi level of the first FM tunnel into free equivalent electronic states at the Fermi level of the second FM and vice-versa. Due to the spin-dependent tunneling effect (see Section 2.1.2), the tunneling resistance of the junction depends on the relative orientation of the magnetizations of the two electrodes (Figure 1.2(a)).

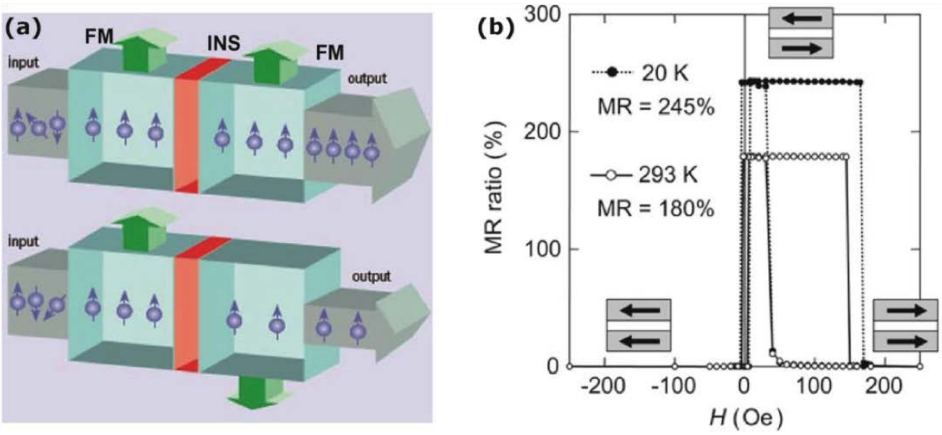

Figure 1.2: *(a) Sketch of the spin-dependent tunneling transport in magnetic tunneling junctions. The resistance is low (high) when the magnetizations are parallel (antiparallel). (b) First observation of the giant TMR effect in epitaxial MgO-based magnetic tunneling junctions. From [12].*

After its first discovery in 1975 [11], for more than a decade, TMR received little attention because it was not observed at room temperature. It attracted renewed attention with the discovery of GMR and its applications. Overall, TMR yields a resistance variation one-two orders of magnitude higher than GMR technology, and thus is steadily replacing the other MR technologies in most applications. Initially, amorphous aluminum oxide (AlO_x) tunneling barriers exhibited TMR values as high as 70% at room temperature [13]. Half metal electrodes (e.g. manganites such as $La_{0.67}Sr_{0.33}MnO_3$ (LSMO)), have been employed because of their 100% spin polarization, reaching TMR ratios up to 1800% at 4.2 K [14]; however, at higher temperatures half-metallicity decreases rapidly, resulting in a drop of the magnetoresistance.

A great boost in TMR technology was given in 2001 by Butler [15] and Mathon [16], who predicted with first-principle calculations that epitaxial MTJs with a crystalline magnesium oxide (MgO) tunneling barrier would give rise to TMR ratios of over 1000%. The inclusion of crystalline MgO barriers and textured MTJ stacks allowed to obtain TMR values up to 600% at room temperature for simple CoFeB/MgO/CoFeB structures [17], while optimum values decrease to 250% for complex engineered stacks developed for device applications [18]–[21]. The reported high TMR values in MgO-based MTJs are enabled by the combination of coherent tunneling through the crystalline MgO barrier and spin-filtering effect of MgO, in contrast with the non-coherent tunneling across amorphous alumina barriers (see Section 2.1.4).

1.2 Biological application of magnetoresistive sensors

The brain is by far the most complex organ in the human body. Understanding brain working principles through the investigation of neural signals from single neurons or neural arrays is a key aspect for further studies on neurologic diseases and related therapies. Nowadays, neurologic diseases constitute an enormous social and economic burden and little effective treatment is available for many of them. Many drugs used for neurologic therapy target ion channels, but the full spectrum of their effects is poorly understood and serious side effects are sometimes observed. A general hindrance towards quicker advance in this area is related to the experimental difficulties encountered in correlating the functions at the subcellular, cellular and network levels.

1.2.1 Neuronal physiology

Information processing in the brain is presumed to arise from interactions and correlations across several orders of magnitude of temporal and spatial scales and tens of thousands to billions of computational units [22]. The smallest computational unit is the synapse, with sub-micron structures involved in chemical and electrical signaling. Changes in synaptic dynamics are the basis of learning and memory. Neurons are organized in networks with complex, and largely unknown, connection rules. Networks may contain over a dozen of different neuron types, each with their own dynamics and connection rules.

To support the general functioning of the nervous system, neurons have evolved capabilities for intracellular and intercellular signaling. A neuron comprises a cell body (soma) and two extensions: the dendrites that receive neuronal inputs (input components) and the axons that carry the information to other neurons (output components) (Figure 1.3). The soma (integrative component) is the metabolic center that contains the nucleus, allowing storage of the genes and synthesis of cell’s proteins. To achieve long-distance rapid communications, neurons send electrical signals, called Action Potentials (APs), along axons. This mechanism, called conduction, is how the cell body of a neuron communicates with its own terminals via the axons. Communication between neurons is instead achieved at synapses by the process of neurotransmission.

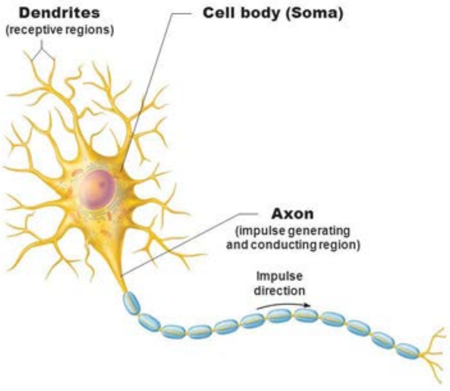

Figure 1.3: *Typical neuron structure. The action potential propagates along the axon.*

To begin conduction, an action potential is generated near the cell-body (soma) portion of the axon. An action potential is an electrical signal very much like the electrical signals in electronic devices. But whereas an electrical signal in an electronic device occurs because electrons move along a wire, an electrical signal in a neuron occurs because ions move across the neuronal membrane. Since the membrane acts as a barrier to ions, they move across it through ion channels that open and close thank to the presence of neurotransmitters. When the concentration of ions on the inside of the neuron changes, the electrical property of the membrane itself changes. Normally, the membrane potential of a neuron rests at -65 mV (resting potential) with respect to the extracellular environment and the membrane is said to be polarized. The inflow and outflow of ions (through ion channels during neurotransmission) will make the inside of the target neuron more positive (hence, depolarized). When this depolarization reaches a threshold, an electrical signal is generated. A sketch of the described mechanism is represented in Figure 1.4(top) while Figure 1.4(bottom) shows a typical action potential signal.

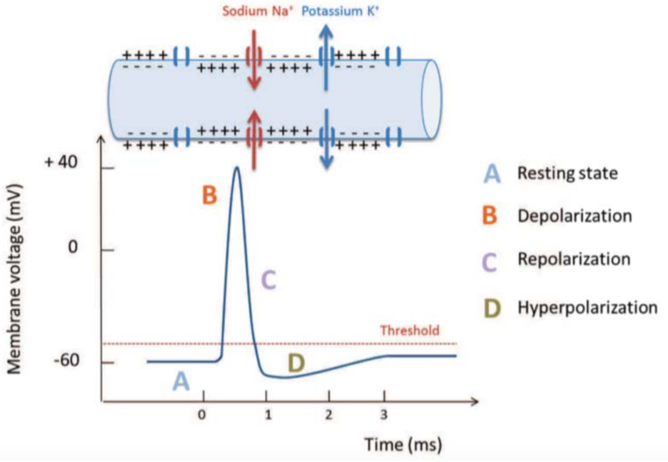

Figure 1.4: *(top) Sketch of the action potential generation and propagation mechanism along the axon. (bottom) Typical action potential signal. When* Na^+ *ions enter through the membrane, the local potential (which was at its resting value (A)) increases and reaches a strong positive value (B); the opening of the* K^+ *channels which drives positive ions from the inside to the outside of the cell induces a decrease in the membrane potential (C). The last phase is the hyperpolarization (D) where the potential returns to its resting value [23].*

This signal then propagates along the axon until it reaches the axon terminals. Conduction ends at the axon terminals and intercellular neurotransmission begins (Figure 1.5).

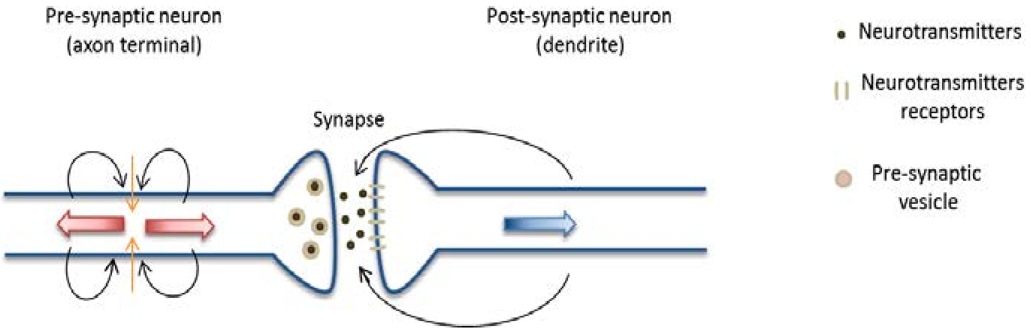

Figure 1.5: *AP transmission between a pre-synaptic neuron and a post-synaptic dendrite. When the depolarization (AP) arises in the axon terminal, neurotransmitters are released, generating a Post-Synaptic Current (PSC). The red arrows are the action potential currents; the blue arrow is the PSC; the orange arrows are the transmembrane currents.*

While local conditions in the neuron determine signal flow into and out of synapses, complex signal integration and filtering occurs independently in different branches in the dendritic tree (the neuronal input structure). The decision to trigger an output is made in the axon (Figure 1.6).

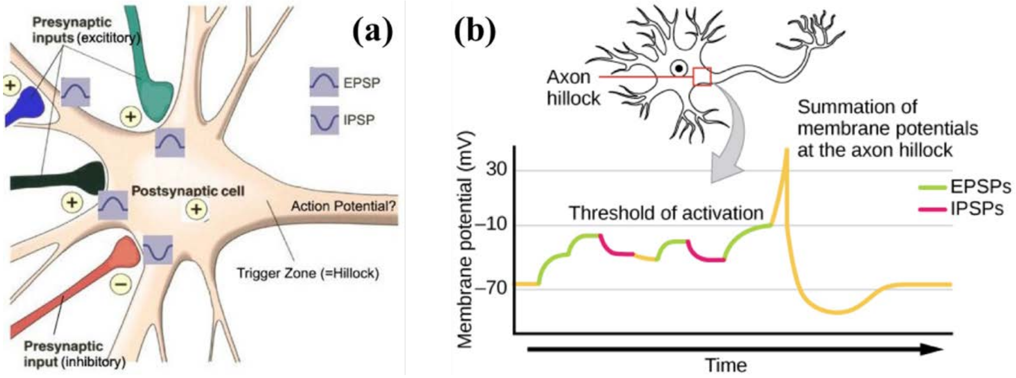

Figure 1.6: *(a) A neuron receives both excitatory postsynaptic potentials (EPSPs) and inhibitory postsynaptic potentials (IPSPs). EPSPs are depolarizing and increase the likelihood that the neuron will fire an action potential; inhibitory postsynaptic potentials (IPSPs) are hyperpolarizing, decreasing the likelihood that the neuron will fire. From [24]. (b) At axon hillock the summation of membrane potentials occurs. The neuron will fire if the excitatory signals overcome the inhibitory signals reaching the threshold.*

Understanding the behavior of these systems requires understanding the interactions between computational units at different scales [25], [26].

1.3 Magnetic field generated by neurons

Any currents flowing inside the brain can create a magnetic field. Hence, intracellular axial currents can be considered the first source, but return extracellular currents play, as well, a relevant role. Seen at a very large distance, all the currents cancel out and no net magnetic field is created. Locally, the intracellular axial currents will have a dominant contribution in the detected magnetic field (Figure 1.7). An important issue related to this work is to evaluate the amplitude and direction of the magnetic field created by a single neuron or by an assembly of neurons.

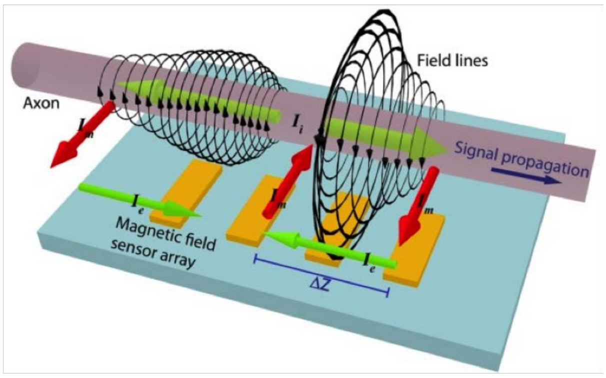

Figure 1.7: *Sketch of the spatial distribution of magnetic field and currents during the propagation of action potentials. Red arrow is the transmembrane ionic current* I_m*, large green arrow is the intracellular current* I_i*, small green arrow is the extracellular current* I_e*.*

1.3.1 Simple model

Let us consider a single neuron. To obtain just a gross estimate of the orders of magnitude involved, we will consider a cylindrical axon of diameter $d = 2$ μm and internal resistivity $\rho \cong 2$ Ωm. When an action potential is created, the potential difference along the neuron induces a net current given simply by the Ohm's law. Thus, assuming a $\Delta V = 100$ mV between depolarized and resting regions, on a distance $l = 200$ μm (spatial length of depolarization phase of action potential), the net current is:

$$I = \frac{\pi d^2 \Delta V}{4 \rho l} \cong 1\, nA \tag{5.1}$$

This current induces an Oersted's magnetic field according to the Biot-Savart law. For a very small distances r compared to the neuron length, the field is orthoradial and simply given by:

$$B = \frac{\mu_0 I}{2\pi r} \cong 20\, pT \tag{5.2}$$

for a 10 μm distance. As long as $r \ll l$, the r^{-1} is still valid, but for long distances the dependence becomes r^{-3}.

1.3.2 Volume conductor model

A more accurate model should take into account the actual geometry of an axon, far from being a cylinder, the frequency dependence of transport in biological media and the time variation of the signal taking into account the capacitances and resistances (cable theory).

The volume conductor model has proven that the magnetic field of a nerve axon can be accurately calculated from the transmembrane potential, provided the resistance of the axon is known. In the work of Roth and Wikswo [27], it is shown the comparison between the measured and calculated magnetic field for the medial giant axon of a crayfish. As one can see from Figure 1.8, the accordance is very good.

Using the same parameters as the reference, i.e. $d = 107$ m, $\rho = 0.5\ \Omega$m, $r = 1.48$ mm and a measured transmembrane potential $\Delta V = 100$ mV, in the simple model one get a field of about 80 pT that is a factor 2 smaller of the experimental value, showing the coarseness of the model.

Some areas of the brain, such as the hippocampus, present the fundamental physiological advantage of having hundreds of neuronal axons running parallel to each other. Then the magnetic signals coming from each axon sum up resulting in a magnetic field of the order of 10 nT.

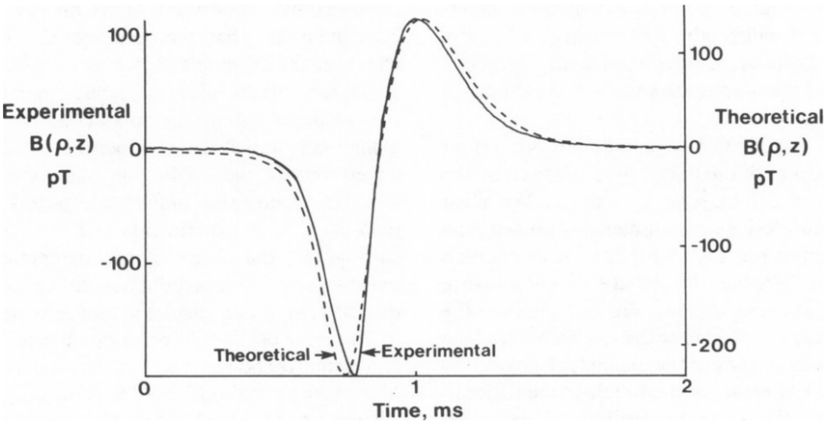

Figure 1.8: *Comparison of the measured magnetic field from the axon of a crayfish (solid) and that calculated from the transmembrane potential using the volume conductor model (dashed). From [27].*

Using the same parameters as the reference, i.e. $d = 107$ m, $\rho = 0.5\ \Omega$m, $r = 1.48$ mm and a measured transmembrane potential $\Delta V = 100$ mV, in the simple model one get a field of about 80 pT that is a factor 2 smaller of the experimental value, showing the coarseness of the model.

1.4 Neuronal signal detection

To address the latter topic, many technological solutions have been proposed. Currently, the detection techniques are grouped in two big families: the ones based on electrophysiology and the ones based on magnetophysiology.

The most widespread neural signal scheme relies on an electrophysiological approach, which is used since the 18th century when Luigi Galvani discovered the link between nervous system and electric activity. Electrophysiology tools measure the electrical activity in living cells (nerve and muscle [28]) and in the extracellular medium [29] and comprises techniques such as electroencephalography (EEG), patch-clamp, local field potential (LFP) recording. All these techniques allow to span different spatial scales for the system to study.

The EEG work on a macroscopic scale. It is the oldest and most widely used non-invasive method investigating cerebral electrical activity through a net of hundreds of electrodes (up to 256) mounted at the surface of the scalp. EEG is commonly used in clinical diagnostic (Parkinson's disease, epilepsy) as well as for cognitive research (perception, movement, language, memory) [30], [31]. It achieves a temporal resolution in the ms range but the spatial resolution is limited by distortion and attenuation form the surroundings tissues (~1 cm). At a mesoscopic to microscopic scale (down to µm range), one finds the LFP recording and patch-clamp. These techniques consist in inserting electrodes to stimulate the cells and recording the real-time voltage drop across the cell membrane that occurs due to the ionic channels opening. The recording is carried out from the extracellular medium or directly within the cell (Figure 1.9(a)), respectively. Such methods achieve a considerable sensitivity but fails to provide signals simultaneously from more than a couple of neurons [32]. The strong progress of micro-fabrication facilities has allowed the development of alternative methods like multi electrode arrays (MEAs) and high density MEAs (hdMEAs) (Figure 1.9(b)) which consist of numerous electrode-containing plates and grant the recording at a network level [33]–[35]. However, such approach is inefficient in providing a one-to-one correlation between the investigated neurons and the acquired signals [36]. Moreover, at such level, the electrophysiology methods are quite invasive, needing contact with the medium. To compensate for this problem, recently emerging techniques are based on optical detection. For example, voltage-sensitive dye imaging (VSDI) is an indirect method that exploits the change in spectral properties in response to a voltage variation of certain molecule. It gives a considerable spatial and temporal resolution, but such compounds are toxic, thus preventing long-term *in-vivo* measurements [37].

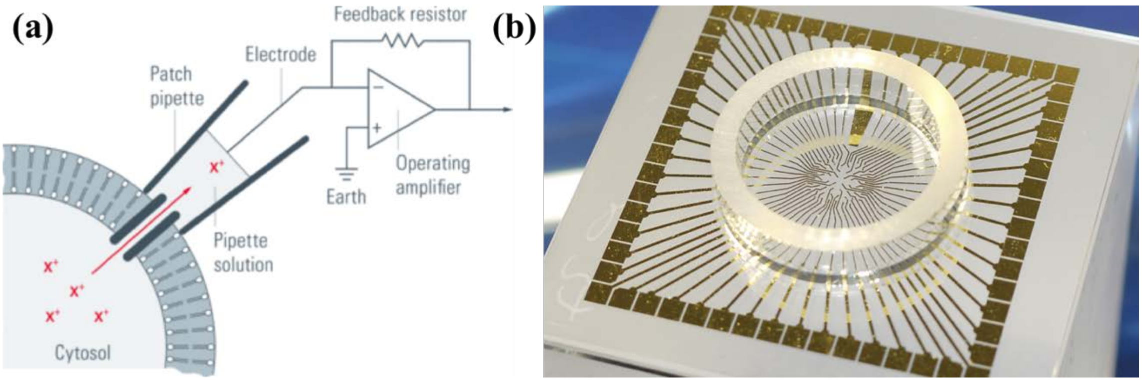

Figure 1.9: *Main methods for recording and stimulating the electric activity of neurons. (a) General principle of patch-clamp recordings. (b) Multi-electrode array.*

A complete absence of invasiveness together with good spatial resolution can be assured by using a magnetic approach. Instead of directly measuring the voltage across the cell membrane, magnetophysiology can detect the magnetic field generated by the neural current along the axon. The essential problem of biomagnetism is the weakness of the signal relative to the sensitivity of the detectors and to the competing environmental noise. The signal ranges from 10 fT to few nT, while the ambient noise is about 100 nT. The magnetic equivalent of the EEG is the magnetoencephalography (MEG). Due to the aforementioned problems, MEG must be performed in a magnetically shielded room employing arrays of cm-sized SQUID (Superconductive Quantum Interference Device) magnetometers, which in addition require liquid-nitrogen temperature [38]. Compared to EEG, recent advances in MEG promise improved spatial resolution (~1 mm) coupled with extremely high temporal resolution (better than 1 ms). Indeed, magnetic fields are less distorted than electric fields by the skull and scalp, which results in a better spatial resolution [39]. On the other hand, the faster decay of magnetic fields as a function of distance (r^{-3} vs r^{-2}) makes MEG very surface-sensitive. Moreover, due to the extreme low working temperature, this technique cannot be easily applied to perform *in-vitro* study, so that different magnetic sensors should be applied when moving to the microscopic scale. A recently developed approach based on nitrogen-vacancy (NV) quantum defects in diamond has been suggested in order to measure the time-dependent magnetic fields produced by single-neuron APs. The NV center is a remarkable optical defect in diamond, which allows discrimination of its magnetic sublevels through its fluorescence under illumination ('bright' spin) [22]. Ultimately, synapse-scale (~10 nm) resolution. circuit-scale (~1 cm) field-of-view and nT-range signal recording can be achieved with such technique [40]. Nevertheless, the latter method lacks in terms of temporal resolution [41].

1.4.1 Ultrasensitive Magnetic Array for recording of Neuronal Activity (UMANA)

To tackle the aforementioned issues, magnetoresistive (MR) devices offer valuable perspectives by virtue of their high sensitivities [42]. Furthermore, since this technology is easily integrable with conventional electronics, they grant a real-time monitoring [43]. Finally, as the detection is mainly surface-based, they guarantee a complete absence of invasiveness during the recording step, as well. Such technique has been firstly introduced by J. Amaral et al. where spin valve featuring giant magnetoresistance (GMR) effect were used as magnetic sensors [44]. The authors, however, reported the presence of spurious capacitive signal and could not confirm an effective magnetic detection.

Despite the emerging interest towards the magnetic recording, this field is still in its infancy. In this context, this thesis work is inserted in the UMANA project framework whose proposal is to introduce a magnetic approach with nanotechnology-based platforms for the in-vitro investigation of the activity of individual cells inside a network. Ultrasensitive magnetic transducers based on magnetoresistive effect integrated on chip can be employed to locally measure the sequence of magnetic pulses produced by neuronal currents.

When the action potential pulses propagate along the axons or dendrites, local electric current loops are generated by the displacement of ions across the neural membrane. For typical neurons the distance Δz between the input and output points of transmembrane ionic currents I_m can be of the order of 800 μm, so that the produced magnetic field (see Paragraph 1.3) essentially arises from the axial intracellular currents I_i [22], whose distribution is showed in Figure 1.7. Then a proper alignment of the axon with the magnetic sensors is fundamental.

In this work, a platform based on Magnetic Tunneling Junctions (MTJs) and dedicated electronics for the detection of neuronal pulses generated by single neurons, neural networks and brain slice is presented.

1.5 Thesis outlook

This thesis work is inserted in the project UMANA. This project aims to develop an Ultrasensitive Magnetic Array for recording of Neuronal Activity (UMANA): a magnetic array-based platform which features highly sensitive magnetoresistive (MR) devices for on-chip detection of low field (pT-nT) generated from the propagation of neuronal current, enabling non-invasive *in-vitro* investigation from single neuronal cells to a network level, with high temporal and spatial resolution.

Sensors' fabrication and preliminary experiments were carried out by the NaBiS group at the PoliFab Center of Dipartimento di Fisica of the Politecnico di Milano under the supervision of Doctor Daniela Petti and Professor Riccardo Bertacco, responsible for the group. The integrated electronics employed for the signal detection has been developed by the I3N group of the Dipartimento di Elettronica, Informazione e Bioingegneria of the Politecnico di Milano which also led the noise measurements. The biological aspects of the work were dealt with by IIT's Center for Synaptic Neuroscience and Technology of Genova, which took care of the preparation of rat hippocampal slices. A paper on the work carried out during this thesis has been written and recently accepted for publication on AIP Advances [45].

In this framework, my thesis work has focused on the fabrication of the magnetic platform, the characterization in terms of noise and sensing performances and then the testing in *in-vitro* experiments.

The thesis consists of 6 chapters:

1.**Introduction:** the motivation, context and organization of the work are presented.

2.**Theoretical background:** the physics behind MTJ-based sensors is reviewed, presenting theoretical and experimental studies.

3.**Experimental methods:** this chapter is dedicated to the description of the principles of thin film deposition, micro- and nano-fabrication and characterization techniques employed in this work for the realization and characterization of the MTJ-based devices.

4.**Towards low-field sensitive sensors for neuronal signal detection:** different sensor's architectures are investigated, in terms of noise and magnetic field sensitivity, to find out which is the best for our aims.

5.***In-vitro* experiments:** the main biological issues are reported together with the growth and fabrication of a MTJ-based sensors array optimized for neurons signal detection and the results of the experiments on brain slices.

6.**Conclusions:** in this chapter the conclusions of this thesis work and the future perspectives are summarized.

Chapter 2: Theoretical background

Magnetic transducers are widely used in modern electronics in many applications, from data storage to sensing applications. Different kinds of sensors exist. In particular, magnetoresistive sensors based on Magnetic Tunnel Junction and Giant MagnetoResistance (GMR) have been investigated in this thesis work.

A Magnetic Tunnel Junction (MTJ) is based on a thin film of a non-magnetic insulating material (I) sandwiched between two ferromagnetic electrodes (FM). This FM/I/FM tri-layer represents the core of the sensor. Upon the application of a bias voltage across the structure, a spin-polarized tunneling current flows perpendicularly to the layers. The amplitude of this current strictly depends on the relative orientation of the magnetizations of the FM layers: when they are parallel, the current will be the highest, while it will be the lowest if antiparallel. When MTJs are employed as magnetic field sensors, the magnetization of one of the FM layers has to be pinned to act as a reference, while the other is free to move accordingly to the external magnetic field to be sensed.

GMR sensors are composed of ferromagnetic layers separated by a non-magnetic (NM) metallic layer (FM/NM/FM). When one of the FM electrodes is used as a reference direction and the other FM is free to rotate, allowing the controlled presence of two, parallel and antiparallel, magnetization configurations, the GMR based structure is called Spin Valve [46]. The magnetoresistance effect observed in these structures is phenomenologically the same of the MTJs, however the physical origin behind is different. While for the MTJ it is due to the tunneling of polarized electron density of states, in the case of the GMR it is related to the spin-dependent scattering.

In this chapter, the theoretical background, on which the operation of these devices is based, is reviewed. In the first part, the principles of tunneling magnetoresistance and giant magnetoresistance are investigated, while the second part deals with the sensor engineering, describing the magnetic effects beneath a MR sensor.

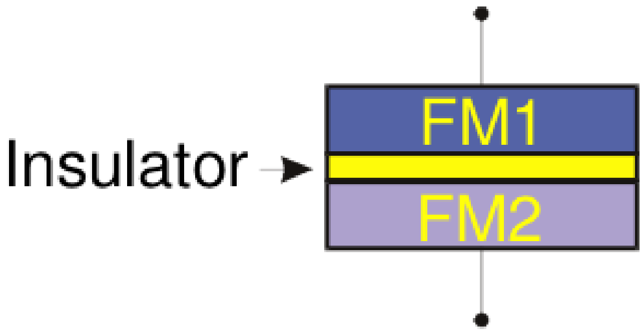

***Figure 2.1:** Schematic illustration of a Magnetic Tunneling Junction (MTJ).*

2.1 Tunneling magnetoresistance theory

Tunneling MagnetoResistance (TMR) is a magnetoresistive effect, which takes place in MTJs. If the insulating barrier is thin enough, electrons can tunnel from one FM layer to the other giving rise to a tunneling current.

2.1.1 Tunneling current model

A classical tunneling junction is made up of two metallic layers (M) separated by an insulating barrier (I). This simple structure is useful to understand the critical parameters involved in the tunneling process.

With no bias applied, the system is in thermodynamic equilibrium (Figure 2.2(a)). This means that the Fermi levels of the two metals are at the same energy and no net current is flowing. When a bias voltage *V* is applied (Figure 2.2(b)), the Fermi levels are displaced of an amount *eV*, where *e* is the electron charge. In this condition, some occupied states of the negative-biased electrode are isoenergetic with empty states of the positive one, giving rise to a non-zero probability for the electron to tunnel through the insulating layer.

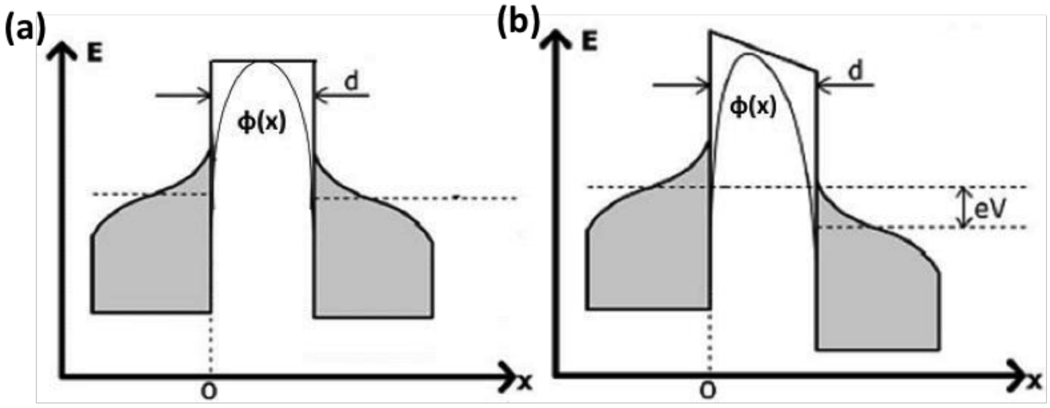

Figure 2.2: *Bandstructure of a M/I/M (a) without and (b) with applied bias V. From [47].*

The net flowing current is given by the difference between the two opposite-moving tunneling current densities:

$$j = j_{l\rightarrow r} - j_{r\rightarrow l} \tag{2.1}$$

Each of these terms depend on the density of states of the electrodes, on the tunnel probability and the occupancy of the energy levels described by the Fermi distribution:

$$j = \frac{e}{2\pi\hbar}\sum_k \int_{-\infty}^{+\infty} dE \rho_l(E - eV)\rho_r(E)|M(E)|^2[f(E) - f(E - eV)] \tag{2.2}$$

where the sum is performed on the transversal components k_x and k_y of the wavevector, $\rho(E)$ is the density of state at energy E (with respect to the Fermi level) and $f(E)$ is the Fermi distribution. As far as the matrix element $M(E)$ is concerned, it is proportional to the transmission coefficient $T(E)$, which is calculated with the Wentzel–Kramers–Brillouin (WKB) approximation. The WKB approximation states that a barrier of any shape can be considered constant as long as it is slowly varying with respect to the wavelength of the electron [47]. In such cases, it holds:

$$|T(E)|^2 \approx e^{-\frac{2}{\hbar}\int_0^d \sqrt{2m(\phi(x)-E)}dx} \tag{2.3}$$

where ϕ is the potential barrier, i.e. the energy gap of the insulator, and m is the mass of the electron.

The problem of evaluating the general formula of Eq. (2.2), has been tackled by several different simplified models [48], [49]. In the work of Simmons [50], an analytical expression for the dependence of j on the applied voltage V was derived. The model assumes T = 0 K, approximating the Fermi distribution with step functions; furthermore, it considers a potential barrier of arbitrary shape $\phi(x)$ and it employs free-electron relations for the density of states. The resulting $j(V)$ characteristic is linear for $V \ll \phi$, but becomes cubic ($j \propto \alpha V+\beta V^3$) for slightly higher potentials, leading to a parabolic conductance (Figure 2.3). Furthermore, the exponential dependence of the current on the barrier height and on the square root of the barrier width is conserved. However, the application of a free electron model leads to a cancellation of the density of states (DOS) of the two electrodes in the expression for the tunneling current. If this were true, there could be no TMR effect. In order to accurately calculate the tunneling current, more sophisticated models have to be applied.

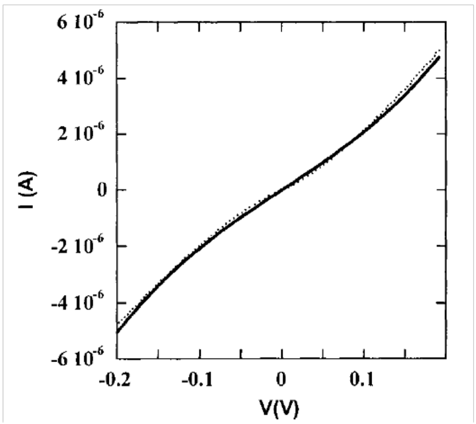

Figure 2.3: *I(V) characteristic at T = 13 K for a tunnel junction of the type CrO2/barrier/Co fitted to the Simmons model (solid black line). From [40].*

2.1.2 Spin-dependent tunneling

Spin-dependent tunneling (SDT) is an imbalance in the electric current carried by up- and down-spin electrons tunneling from a ferromagnet through an insulating barrier. SDT origins from the exchange splitting of electronic bands in ferromagnets, which implies different density of states at the Fermi level for up- and down-spin electrons. Therefore, the number of electrons that can tunnel through the barrier and consequently the tunneling conductance depend on spin.

The accurate description of this phenomenon involves the spin-dependent transmission across the FM/I interface that leads to the spin polarization of tunneling conductance. Let us consider a simpler model, the two currents model by Mott [51]. In this case, some assumptions are needed: spin flip scattering and spin mixing events at the interface are frozen out; magnetizations are referred to a common quantization axis; the temperature of the system is well below its Curie temperature; the conduction is mainly due to *s* electrons since their effective mass is smaller than *d* ones. Under this hypothesis, the conductivities due to majority- and minority-spin electrons can be regarded as independent parallel channels. A graphical representation of this mechanism is given in Figure 2.4. When the magnetizations of FM electrodes are parallel, minority electrons (i.e. those with spin parallel to the magnetization) from the cathode have a large availability of free state for tunneling. On the contrary, majority electrons (spin antiparallel to magnetization) have at disposal fewer states. This result in a small tunneling resistance for minorities and a large one for majorities. Thus, since the two channel are in parallel, the overall tunneling resistance for the parallel configuration R_P is low. On the other hand, in the antiparallel configuration minority and majority electrons are in the same situation. Then their resistance is comparable and the total tunneling resistance $R_{AP} > R_P$.

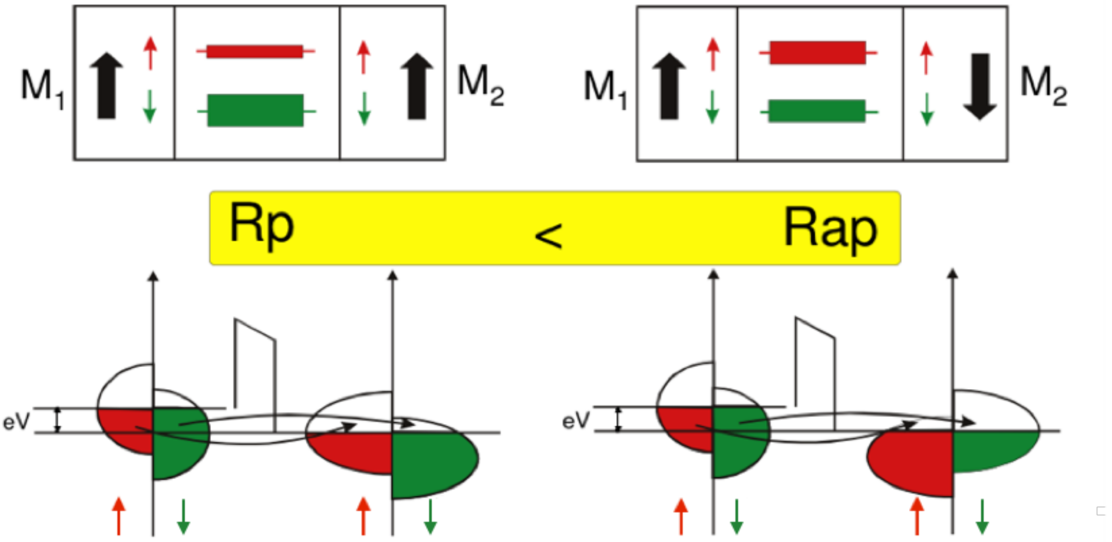

Figure 2.4: *Representation of spin dependent transport mechanism for parallel and antiparallel magnetization configurations.*

2.1.3 Jullière model

The Jullière model [11] gives a phenomenological explanation of tunneling effect in FM/I/FM systems. It is based on three main assumptions: spin conserves during the tunneling; the transmission coefficient is basically independent of energy and magnetization; the applied voltage is small. Then the conductivities for the two independent channels can be written as:

$$G_P \;=\; G_{\uparrow\uparrow} + G_{\downarrow\downarrow} \propto (\rho_{l\uparrow}\rho_{r\uparrow} + \rho_{l\downarrow}\rho_{r\downarrow})|M|^2 \tag{2.4}$$

$$G_{AP} \;=\; G_{\uparrow\downarrow} + G_{\downarrow\uparrow} \propto (\rho_{l\uparrow}\rho_{r\downarrow} + \rho_{l\downarrow}\rho_{r\uparrow})|M|^2 \tag{2.5}$$

where $\rho_{\uparrow(\downarrow)}$ is the density of states of majority (minority) electrons at the Fermi energy, assuming it constant for small bias voltages.

An important figure of merit of MTJs is the TMR ratio that measures the difference between the high and low resistance states and can be expressed as:

$$TMR = \frac{R_{AP} - R_P}{R_P} = \frac{G_P - G_{AP}}{G_{AP}} \tag{2.6}$$

The Jullière model also define the spin polarization *P* as the imbalance in spin-up and spin-down populations at the Fermi level:

$$P = \frac{\rho_\uparrow - \rho_\downarrow}{\rho_\uparrow + \rho_\downarrow} \tag{2.7}$$

Using the last expression, the TMR ratio can be rewritten as a function of the polarization *P*:

$$TMR = \frac{2P_lP_r}{1 - P_lP_r} \tag{2.8}$$

The Jullière model is commonly used to describe the behavior of spin-dependent tunneling process, but it does not take into account the properties of the insulating barrier. Then the model well describes the incoherent tunneling process typical of amorphous barriers, but it fails when dealing with the coherent transport of a crystalline insulators.

2.1.4 Coherent tunneling and spin filtering

In *3d* ferromagnet, at Fermi level, different symmetries in the electronic states arise from the hybridization of the orbitals. Majority and minority carriers have both four Bloch states. In the majority channel, there are *spd* hybridized orbitals (Δ_1), doubly degenerate *sp* orbitals (Δ_5) and *d* orbitals ($\Delta_{2'}$). The minority channel has four states with the same symmetries as the states of the majority channel with the crucial exception that the majority Δ_1 state is replaced by a Δ_2 (*d* hybridized) minority state [15].

In presence of a crystalline insulator, Bloch states of different symmetries decay at different rates within the barrier. This is what is referred to as coherent tunneling. On the contrary, in an amorphous barrier there is no crystallographic symmetry. Then as sketched in Figure 2.5 (a), all Bloch states, regardless their symmetry, can couple to an evanescent state of the amorphous layer and therefore have a finite tunneling probability. The latter case is well described by Jullière model. On the other hand, in case of coherent tunneling only states with the same symmetry can couple to each other and those slowly decaying dominate the tunneling process (Figure 2.5b)). Such an ideal behavior is expected to be observed in epitaxial Fe(001) /MgO(001) /Fe(001).

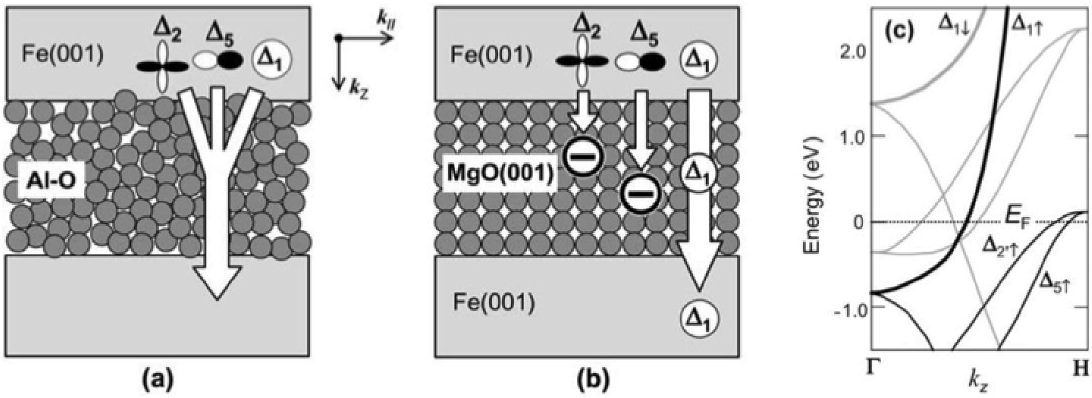

Figure 2.5: *Schematic comparison between (a) amorphous Al-O and (b) crystalline MgO (001) junctions. The electrodes consist of Fe (001), as an example of a 3d metal. (c) Electronic bandstructure of bcc Fe (001) along the* $k_{//} = 0$ *(Γ-H) direction* [16]

Figure 2.6 illustrates the tunneling density of states (TDOS) obtained by first-principle calculations of the evanescent states in MgO layer. In the parallel configuration, the Δ_1 majority states from the first electrode couples to the corresponding evanescent state in the barrier and then can tunnel to the second electrode. The Δ_5 states as well couple to MgO states but they decay much faster, therefore the conduction is dominated by Δ_1 states. Instead, in case of antiparallel alignment, once the majority Δ_1 states have coupled to the barrier's state, they do not find any state with the same symmetry in the second electrode and they are reflected. Then the conduction is led by the Δ_5 minority states, but they decay very fast in the insulating layer thus the conductivity is low. The states with different symmetries (Δ_2, $\Delta_{2'}$) decay even faster, therefore they are negligible as far as conduction is concerned. This is the so-called spin-filtering effect of the MgO crystalline barrier that gives rise to predicted TMR ratios up to 1000% [16].

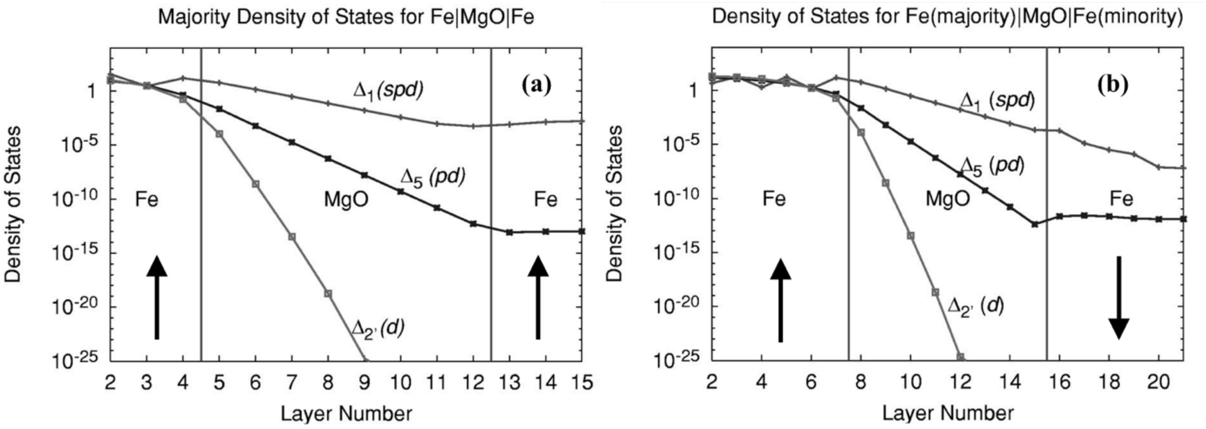

Figure 2.6: *(a) Tunneling DOS of majority-spin states for Fe(001)/ MgO(001)/ Fe(001) with parallel magnetic state. (b) TDOS for Fe(001)/ MgO(001)/ Fe(001) with antiparallel alignment. From [11].*

2.1.5 Sputtered CoFeB/MgO/CoFeB MTJs

The junctions employed in this thesis work are based on the sputtered tri-layer $Co_{0.4}Fe_{0.4}B_{0.2}$/ MgO/ $Co_{0.4}Fe_{0.4}B_{0.2}$ since in principle is the structure with the higher TMR ratio at room temperature [17], [52]. These layers are typically grown by sputtering, so that $Co_{0.4}Fe_{0.4}B_{0.2}$ is amorphous and MgO has a low crystalline quality in they as deposited condition. Therefore, for such system, a thermal annealing process is crucial in order to improve the crystallization of the MgO and $Co_{0.4}Fe_{0.4}B_{0.2}$ layers, making it possible to exploit the spin-filtering properties of the barrier. Thus after this thermal process the TMR increases from 20-30%, typical in amorphous systems, up to several hundred percent [12], [53].

A common figure of merit for MTJs is the resistance-area product (RA), which depends only on the barrier thickness and increases exponentially with it (Figure 2.7(a)). Instead, for a given barrier thickness, resistivity of the junction is inversely proportional to the area. This is due to the fact the number of tunneling electrons is directly proportional to the total electrode area. Therefore, the larger the area the higher the tunneling current, leading to a low resistance state.

Figure 2.7(b) shows the TMR dependence on the barrier thickness for different annealing temperatures. In the ranges from 1.35 to 2.2 nm, the TMR ratio slightly increases with the thickness and dramatically increases with the annealing temperature. This is due to the improvement of the crystalline quality of the barrier for increasing thicknesses and annealing temperatures. Indeed, with thicker barrier, the presence of defects plays a minor role in the conduction mechanism, leaving the coherent process the only tunneling channel.

The TMR of a MTJ depends also on the applied voltage as can be seen in Figure 2.7(d).

Generally, it is almost constant until 25-30 mV and then it starts to decrease for increasing bias voltage. Different models have been proposed in order to explain this dependence. One of them, which correctly predicts the TMR behavior as a function of the applied voltage, has been proposed by Zhang et al. When the bias voltage increases, the "hot electrons", having an excess of energy *eV*, can disexcite transferring this energy excess to collective excitations of local spins, the magnons. This causes spin flip events and spin mixing, decreasing the spin polarization and thereby the TMR ratio [54].

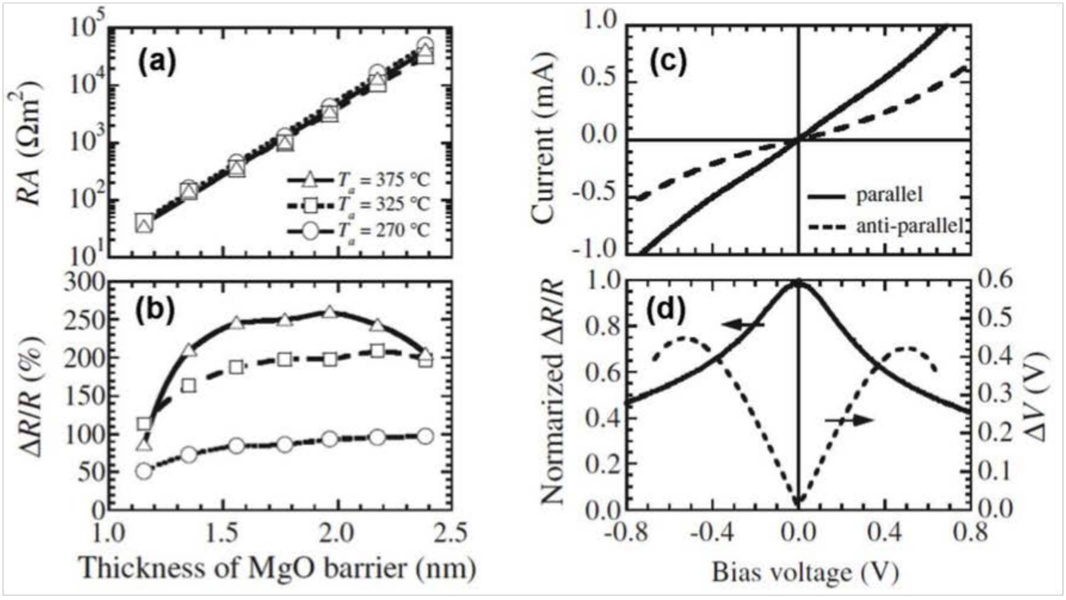

Figure 2.7: *(a) RA and (b) ΔR/R at room temperature as functions of the thickness of the MgO barrier. Dotted, dashed, and solid lines show data for MTJs annealed at 270, 325, and 375 °C. (c) I-V curves of MTJs in parallel (solid line) and in anti-parallel [55].*

A dependence of the TMR on the applied voltage can arise also because of some non-ideality factors. The decrease of the TMR ratio may be due to the presence of defects in the barrier, which starts to conduct as the voltage increases opening of new conductive channels, which reduce the spin-dependent contribution to the tunneling. Moreover, the barrier of the MTJ is a dielectric and dielectric breakdown can occur when the bias voltage increases beyond a certain value. In this regime, pinholes are formed, providing low resistance metallic conduction channels, resulting in the loss of TMR. The voltage at which this phenomenon occurs is called the breakdown voltage and is related to the dielectric strength of the insulator.

2.2 GMR

Giant magnetoresistance (GMR) is a quantum mechanical magnetoresistance effect observed in thin film multilayered structures composed of alternating ferromagnetic and non-magnetic layers. It was discovered in 1988 by the team of Albert Fert in France [6] on Fe/Cr(001) multilayers and, independently, by Peter Grünberg and coworkers in Germany on Fe/Cr/Fe(001) tri-layers [56]. The observed effect is a significant change in the electrical resistance of such structures depending on whether the magnetizations of consecutive ferromagnetic layers are parallel or anti-parallel. Figure 2.8 shows an example of GMR curve in Fe/Cr layers.

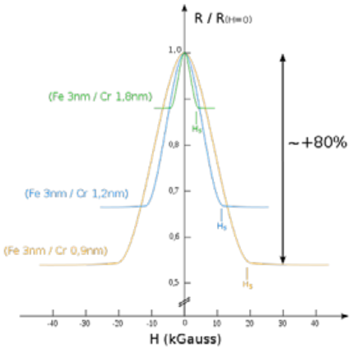

Figure 2.8: *Change in the resistance of Fe/Cr superlattices at 4.2 K in external magnetic field H. The current and magnetic field are parallel to the [110] axis. The arrow to the right shows maximum resistance change. Hs is saturation field [6].*

The origin of this effect is the electron spin-dependent scattering within the ferromagnetic layers and at their interfaces. As shown in Figure 2.9, depending on the magnetization direction of the ferromagnetic layers, there is an electron scattering asymmetry, which results in different resistances for each spin channel. If the magnetizations of the ferromagnetic layers are parallel, one of the spin channel will be weakly scattered in the ferromagnetic layers and there will be a shorting of the conduction by the corresponding channel. On the contrary, if the magnetizations are antiparallel, the electrons of both channels will be strongly scattered, resulting into two parallel high-resistance channels, giving rise to a high resistance state.

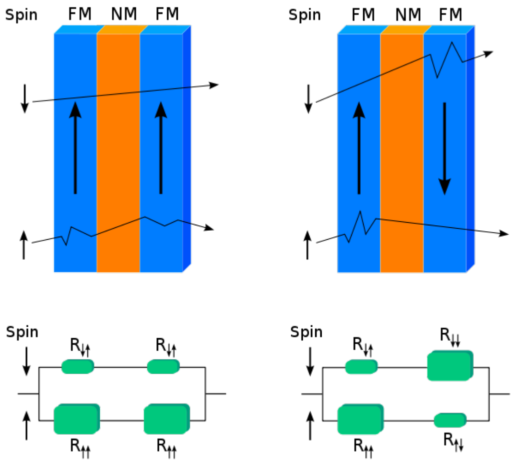

Figure 2.9: *Spin valve based on the GMR effect. FM: ferromagnetic layer (arrows indicate the direction of magnetization), NM: non-magnetic layer. Electrons with spin up or down scatter differently in the valve. In the resistance scheme, the first arrow refers to the spin, while the second to the magnetization*

As shown in Figure 2.10, GMR effect can arise from two current configurations: current-in-plane (CIP) and current-perpendicular-to-plane (CPP). In the CIP geometry, the current runs parallel to the layers; in the CPP configuration, the current flows perpendicular to the layers [57]. The CPP geometry results in more than twice higher GMR, but is more difficult to realize in practice than the CIP configuration [58].

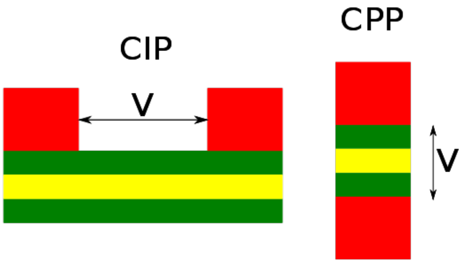

Figure 2.10: Spin valves in the reading head of a sensor in the CIP (left) and CPP (right) geometries. Red: leads providing current to the sensor. Green and yellow: ferromagnetic and non-magnetic layers. V: potential difference.

2.2.1 CIP configuration

During this thesis work, GMR sensors with CIP configuration have been studied. In this kind of sensors, the MR effect arises from the asymmetry in the spin-dependent transmission coefficient at the FM/NM interface.

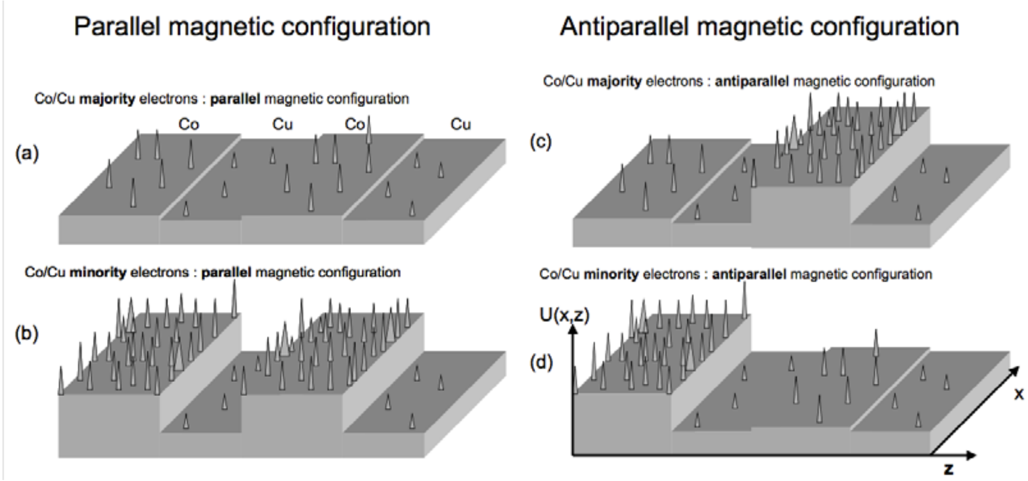

Figure 2.11: *Potential landscape seen by spin ↑ and spin ↓ conduction electrons in the P and AP configurations. The intrinsic potential is represented by a periodic array of steps. The bulk and interface scattering potentials are represented by spikes. From* [59].

Figure 2.11 represents schematically the potential landscape seen by the electrons: (a) and (b) are for the spin ↑ and spin ↓ electrons in the parallel (P) configuration while (c) and (d) are for the antiparallel (AP) configuration. Two contributes to the potential can be distinguished: the intrinsic lattice potential modulation of the perfect multilayered structure (superlattice) due to difference between Fermi energy and bottom of conduction band, which determines the wave functions of the electrons carrying the current; the scattering (extrinsic) potentials due to defects (atomic disorder, impurities, interface roughness) represented by spikes. Even though in a magnetic multilayer both the intrinsic and extrinsic potentials are spin-dependent and contribute to the GMR effect [60], the main results can be obtained just considering the intrinsic potential (semi-classical model).

The problem can be tackled using the Boltzmann's equations for transport. Under the hypothesis of linearization and relaxation time approximations, the equation reduces to [61]:

$$\frac{\partial g_\sigma(z,\boldsymbol{v})}{\partial z}+\frac{g_\sigma(z,\boldsymbol{v})}{\tau v_z}=\frac{eE}{m v_z}\frac{\partial f_0(\boldsymbol{v})}{\partial v_x} \tag{2.9}$$

where f_0 is the equilibrium distribution function, g is the correction to the distribution function due to scattering and the external electric field E (in the x direction), σ indicates the spin of the electron (majority ↑ or minority ↓), τ is the scattering relaxation time and the indexes refer to the situation depicted in Figure 2.12. In particular, in a simpler case one can assume τ to be the same in FM and NM materials and independent from spin.

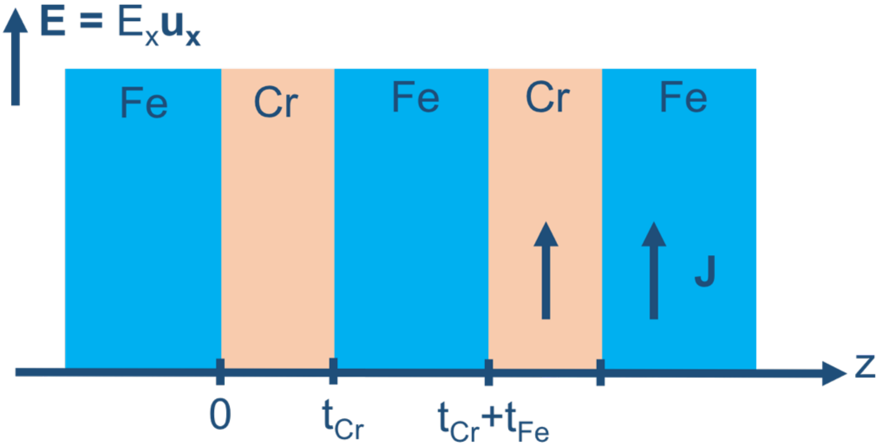

Figure 2.12: *Sketch of a Fe/Cr-multilayered structure. The stack is oriented along the z axis, while the current J flows in x direction.*

Then for electrons with a positive + (negative -) v_z and spin σ, the boundary condition at the interface $z = 0$ is written:

$$g_\sigma^\pm(\boldsymbol{v}, z=0^\pm) = T_\sigma g_\sigma^\pm(\boldsymbol{v}, z=0^\mp) \tag{2.10}$$

The boundary conditions mean that, because a fraction of the electrons T_σ is coherently transmitted while a fraction $(1-T_\sigma)$ is diffusely scattered by the interface roughness, the departure from the equilibrium distribution is reduced by the factor T_σ just after an interface crossing. The dependence of T_σ on the spin arises from the lattice potential modulation that creates barrier of different heights for different spin states (Figure 2.11). Such difference gives rise to the magnetoresistance.

The general solution for Eq. 2.9 is:

$$g_\sigma^\pm(\boldsymbol{v}, z) = e\tau E v_x \frac{\partial f_0(\boldsymbol{v})}{\partial v_x} G_\sigma^\pm(\boldsymbol{v}, z) \tag{2.11}$$

with

$$G_\sigma^\pm(\boldsymbol{v}, z) = 1 - A^\pm exp\left(\mp \frac{z}{\tau|v_z|}\right) \tag{2.12}$$

where A is an integration constant.

Assuming for example $T_\uparrow < T_\downarrow$, as it is in Fe/Cr structures [62], the situation is as shown in Figure 2.13 for the P configuration. Far from an interface, $G_\sigma^\pm$ assumes its bulk value $G_\sigma^\pm = 1$, while just after the interface it becomes $G_\sigma^\pm = T_\sigma$. Since majority electrons are more scattered, the conductance for minority carriers is, on average on the whole structure, higher than the conductance for majorities. Then it follows that $j_\uparrow < j_\downarrow$, $\rho_\uparrow > \rho_\downarrow$ and consequently $R_P = \rho_\downarrow$. On the other hand, in the AP alignment spin ↑ and spin ↓ electrons are alternatively majority and minority carriers, then their resistances are equal and $R_{AP} > R_P$.

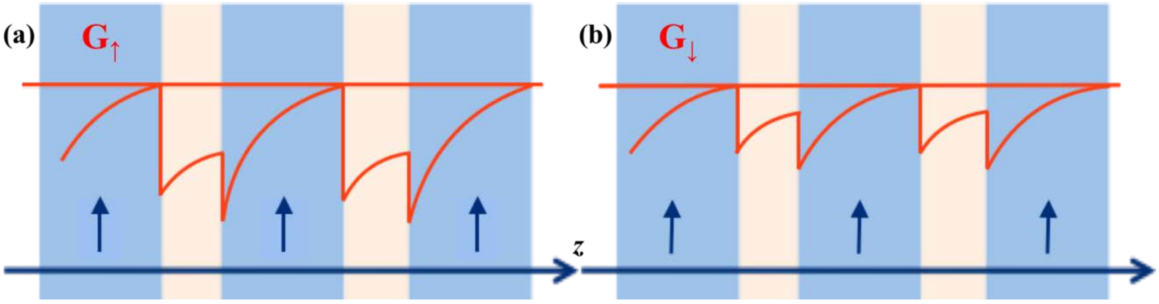

Figure 2.13: *Illustration of the semi-classical model for CIP-GMR in case of parallel alignment. The red curves are the conductances of (a) majority and (b) minority electron; the horizontal line is the bulk value of conductance. Majority electrons undergo a stronger scattering at interface, then on average the conductance is lower. This means the minority channel has higher current and lower resistance.*

It is worth noting that the conductance recovers the bulk value with an exponential behavior on a length scale given by the scattering relaxation length $\lambda_s = \tau|v_z| \leq \lambda = \tau v_F$, λ being the electron mean free path (MFP). Thus, the MFP is the characteristic length of the process for the CIP-GMR and in order to have MR effects, the NM layers must be thinner than λ_s.

2.2.2 CPP configuration

For what concern the CPP geometry, the GMR is not only definitely higher than in CIP but also subsists in multilayers with relatively thick layers, up to the micron range. Actually, as explained in the Valet-Fert model of the CPP-GMR [7], spin-polarized currents flowing perpendicularly to the layers induce spin accumulation effects at the interfaces and the final result is that the length scale governing the thickness dependence becomes the spin diffusion length l_s (related to the spin relaxation) in place of the electron mean free path of the CIP-geometry. Since $l_s \ggg \lambda$ [7], it follows that the layers in the CPP architecture can be much thicker.

The physics of the spin accumulation, occurring when an electron flux crosses an interface between a ferromagnetic (FM) and a nonmagnetic (NM) material, is explained in Figure 2.14 for a simple situation (single interface, no interface resistance, no band bending, single polarity). In Figure 2.14(a), the incoming electron flux is predominantly carried by the spin-up direction whereas the outgoing flux is carried equally by both spins. Consequently, there is accumulation of spin-up electrons at the interface and this accumulation diffuses on both sides of a FM/NM interface to a distance of the order of the spin diffusion length. In terms of electrons distribution, the spin accumulation is described as a splitting of the spin up and spin down Fermi energies (chemical potentials), as shown in Figure 2.14 (b). The spin-flips generated by this out-of-equilibrium electron distribution in the spin accumulation zone provide the mechanism of the adjustment between the incoming and outgoing spin currents. Thus, the spin polarization of the current decreases progressively as it goes through this broad spin accumulation zone. In a similar way, for the current in the opposite direction, the opposite mechanism progressively polarizes the current. In both cases, the spin-polarization of the current just at the interface depends on the proportion of the depolarizing (or polarizing, depending on the direction of the current) spin-flips induced by the spin accumulation.

In a similar fashion to what done for the CIP-GMR, the Boltzmann's equation can be solved for the ideal case of isolated interface between two FM with opposite magnetizations. First, let us assume that the chemical potential can be written as:

$$\bar{\mu}_{\pm} = \bar{\mu} + \Delta\mu \tag{2.13}$$

where $\bar{\mu}$ and $\Delta\mu$ are respectively the spin-independent and spin-dependent terms and note that:

$$F(z) = \frac{1}{e}\frac{\partial\bar{\mu}}{\partial z} \tag{2.14}$$

is equivalent to an electric field.

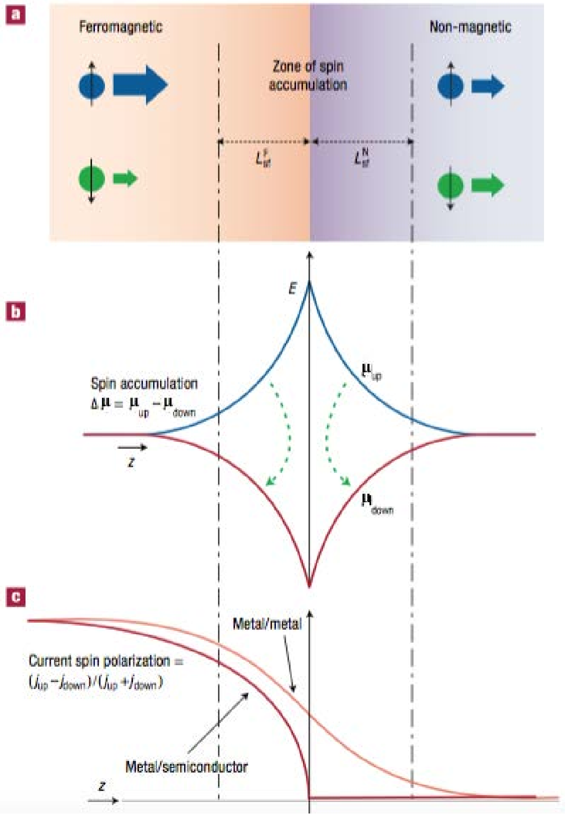

Figure 2.14: *Schematic representation of the spin accumulation at an interface between a ferromagnetic metal and a non-magnetic conductor. (a) Incoming and outgoing spin-up and spin-down currents. (b) Splitting of the chemical potentials,* μ_{up} *and* μ_{down}*, in the interface region (spin accumulation). The arrows symbolize the spin flips induced by this out of equilibrium distribution. These spin-flips govern the progressive depolarization of the current. With an opposite direction of the current, the spin accumulation is in the opposite direction and opposite spin flips polarize progressively the current. (c) Variation of the spin polarization of the current when there is an approximate balance between the spin flips on both sides (metal/metal curve) and when the spin flips on the magnetic side are predominant (metal/semiconductor curve) in the situation without spin-dependent interface resistance. Adapted from* [57].

Then what one obtains for the perturbations of the spin accumulation $\Delta\mu$, the electric field F inside the solids and the current density J is:

$$\Delta\mu = \frac{\beta}{1-\beta^2} e E_0 l_s e^{|z|/l_s} \tag{2.15}$$

$$F = E_0\left(1 + \frac{\beta^2}{1-\beta^2} e^{|z|/l_s}\right) \tag{2.16}$$

$$J_{\pm} = (1 \mp \beta)\frac{J}{2}\left(1 \pm \frac{\beta}{1 \mp \beta} e^{|z|/l_s}\right) \tag{2.17}$$

where E_0 is the unperturbed applied electric field, l_s is the average length of spin relaxation, *e* is the electron charge, β is the spin asymmetry coefficient $\beta = \frac{\rho_\downarrow - \rho_\uparrow}{\rho_\downarrow + \rho_\uparrow}$, $\rho_{\uparrow(\downarrow)}$ being the resistivity of the spin ↑(↓) carriers, and the ± for the current refers to the two possible spin states. The behaviors as functions of *z* are reported in Figure 2.15.

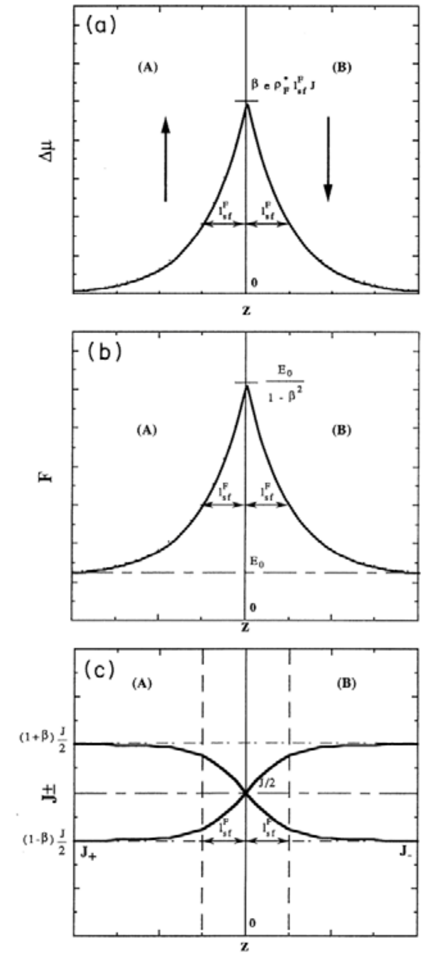

Figure 2.15: *Graphical representation of spin accumulation, electric field and current density as function of z at the interface of two FM with opposite magnetizations. The spin accumulation significantly reduces the current asymmetry and increases the electric field over a length* l_s *on both sides of the interface.*

It can be noted that the reversal of magnetizations introduces an additional voltage drop:

$$\Delta V_I = \int_{-\infty}^{+\infty} [F(z) - E_0] dz = 2\beta^2 \rho_{FM} l_s J \tag{2.18}$$

where ρ_{FM} is the bulk resistance of the FM material. This implies the presence of an interfacial resistance per unit area r_{SI}, called spin-coupled interface resistance [63]:

$$r_{SI} = 2\beta^2 \rho_{FM} l_s \tag{2.19}$$

Its physical meaning is that the spin accumulation significantly reduces the current asymmetry over a length l_s on both sides of the interface.

The same reasoning can be applied to the more complex case of multilayer composed of ferromagnetic layers (ρ_{FM}, thickness t_F) alternating with non-magnetic layers (ρ_{NM}, thickness t_N). The results are illustrated in Figure 2.16.

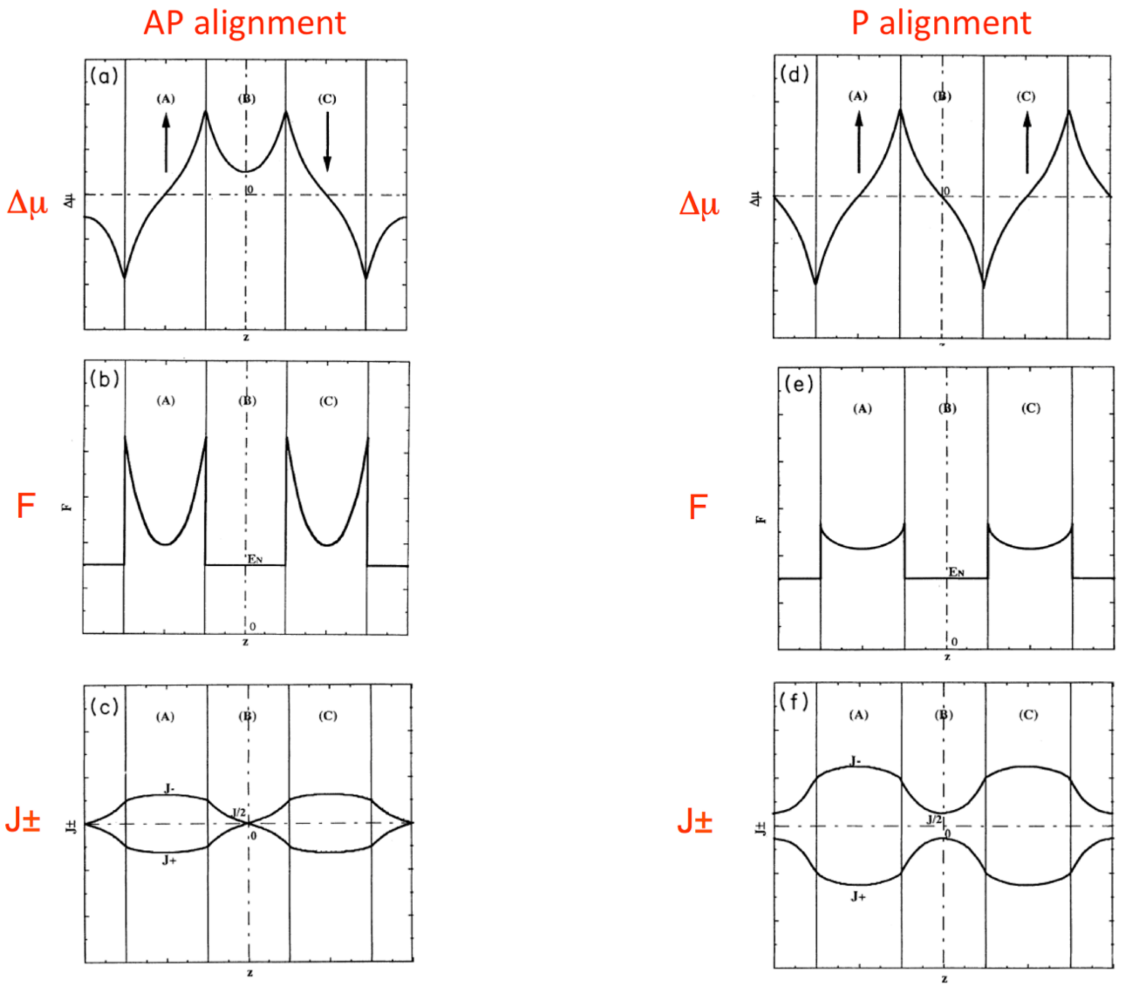

Figure 2.16: *Comparison between spin accumulation, electric field and current density for AP and P alignment of the FM layers in a multilayered structure. The spin accumulation in a non-magnetic layer is more relevant for an AP magnetic configuration in which the easily injected spin direction is the less easily extracted; this affects also F and J. The higher F causes the difference in resistance between the two opposite configurations from which the GMR origins; the current asymmetry is strongly reduced.*

The main difference with respect to the previous case is the proportionality to hyperbolic functions (*cosh*, *sinh*) instead of an exponential behavior. In the multi-interface structure of a CPP-GMR, there is an interplay between the spin accumulation effects at successive interfaces. The spin accumulation in a non-magnetic layer is more relevant for an AP magnetic configuration in which the easily-injected spin direction is the less easily extracted. The CPP-GMR is indeed related to the difference between the spin accumulation in the P and AP configuration. The total resistance of the structure can be calculated as:

$$r^{AP/P} = \frac{\int_{-\infty}^{+\infty} F^{AP/P} dz}{J} \tag{2.20}$$

and finally, since $F^{AP} > F^{P}$, one obtains that $r^{AP} > r^{P}$. The GMR ratio vanishes only when the thickness becomes larger than the spin diffusion length l_s.

More generally, the spin accumulation effects govern the propagation of a spin-polarized current through any succession of magnetic and non-magnetic materials and play an important role in all most recent developments of spintronics.

2.3 Sensor engineering

The MTJs sensors consist in a multilayered structure, each layer realized with the suitable features (material, thickness) to achieve precise functionalities. In Figure 2.17 the MTJ structure is presented: in addition to the core junction (FM/I/FM), buffer layers, capping layers and the so-called synthetic antiferromagnet (SAF) layers complete the sensor structure.

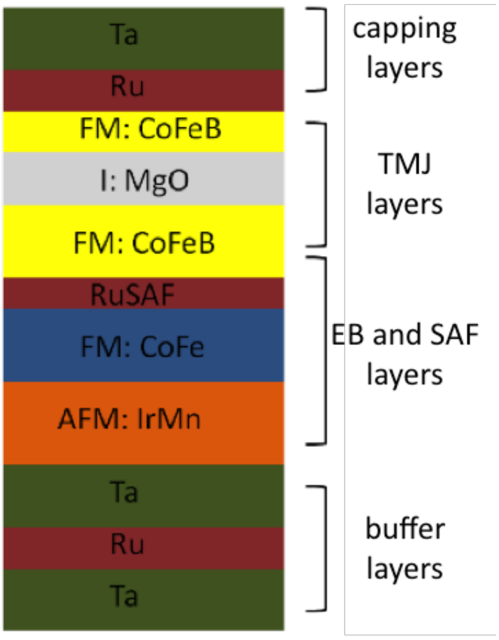

Figure 2.17: *Schematic representation of a MTJ-based sensor stack.*

The buffer tri-layer Ta/Ru/Ta and the capping bi-layer Ta/Ru are critical for having high TMR ratio values since they positively affect the crystallization of both the $Co_{0.4}Fe_{0.4}B_{0.2}$ electrodes [64], [65]. Moreover, the capping layer protects the junction from oxidation.

In order to carry out the detection of an external magnetic field, the relative orientation of the two FM layer must be well defined. This condition is achieved defining a fixed reference layer and a free sensing layer.

In the MTJs developed in this work, the pinning of the reference $Co_{0.4}Fe_{0.4}B_{0.2}$ layer (bottom one) is achieved exploiting two important interfacial phenomena: the exchange bias and the bilinear coupling. The $Co_{0.4}Fe_{0.4}B_{0.2}$ bottom layer is antiferromagnetically coupled to the $Co_{0.6}Fe_{0.4}$ layer through the Ru spacer layer by bilinear coupling. In turn, the $Co_{0.6}Fe_{0.4}$ layer is coupled through exchange bias to the $Ir_{0.2}Mn_{0.8}$ antiferromagnetic layer. Such a complex structure is used principally to minimize the stray field generated from the reference layer, which alters the magnetic response of the free layer. In fact, the ensemble of $Co_{0.4}Fe_{0.4}B_{0.2}$ and $Co_{0.6}Fe_{0.4}$ layers, which are in antiparallel alignment, and the antiferromagnetic $Ir_{0.2}Mn_{0.8}$ layer has an overall magnetic moment that is basically null. That is why it is called synthetic antiferromagnet (SAF). Furthermore, the use of a SAF structure improves the thermal stability of the sensor since the Ru layer prevents Mn to diffuse toward the junction [66]. As far as the sensing layer is concerned, a linear R vs H response is highly desirable in order to perform a correct detection. This condition is met exploiting the superparamagnetic behavior of thin FM films.

The GMR sensors in the CIP configuration employed in this work have been provided by the INESC laboratory of Braga and their stack structure is sketched in Figure 2.18. The core of the devices is the $Co_{0.6}Fe_{0.4}/Cu/Co_{0.6}Fe_{0.4}$ tri-layer, grown on a buffer layer. In this case, the pinning of the top pinned layer is obtained via direct exchange bias with a $Ir_{0.2}Mn_{0.8}$ AFM layer. The structure is terminated by a capping bilayer.

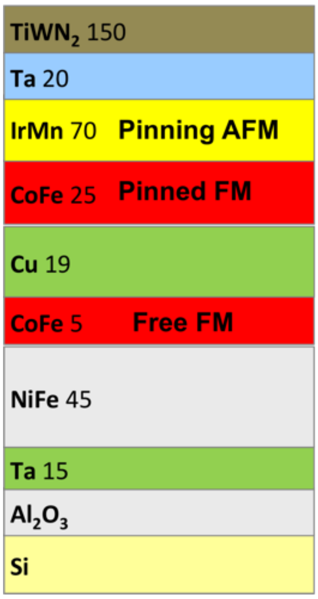

Figure 2.18: *Sketch of the GMR-based sensor stack. Thickness in Å.*

2.3.1 Exchange bias

The exchange bias is an interfacial phenomenon that occurs between a ferromagnet (FM) and an antiferromagnet (AFM). Usually a FM with a Curie temperature T_C greater than the Néel temperature T_N of the AFM is chosen in order to establish the exchange bias through the so-called field cooling process.

The field cooling consists in heating the sample above T_N (but below T_C) in presence of an external magnetic field strong enough to orient the FM. Being the AFM order partially lost (Figure 2.19 (a)), when the temperature is slowly lowered below T_N, the FM is still well oriented and the topmost atomic layer of the AFM tends to align parallel to the closest FM atomic layer establishing the exchange bias (Figure 2.19(b)). The rest of the AFM lattice will arrange accordingly. The macroscopic phenomenology of this effect is the shifting of the hysteresis loop by a quantity H_E called exchange bias field and the FM is said to be pinned by the AFM. The exchange bias field can act in competition or in agreement with the external field H. If they are opposite (Figure 2.19(c)), a stronger field is required to move the FM magnetization resulting in the shift of the loop. When H_E is parallel to H (Figure 2.19(e)), it makes it easier to revert the FM magnetization.

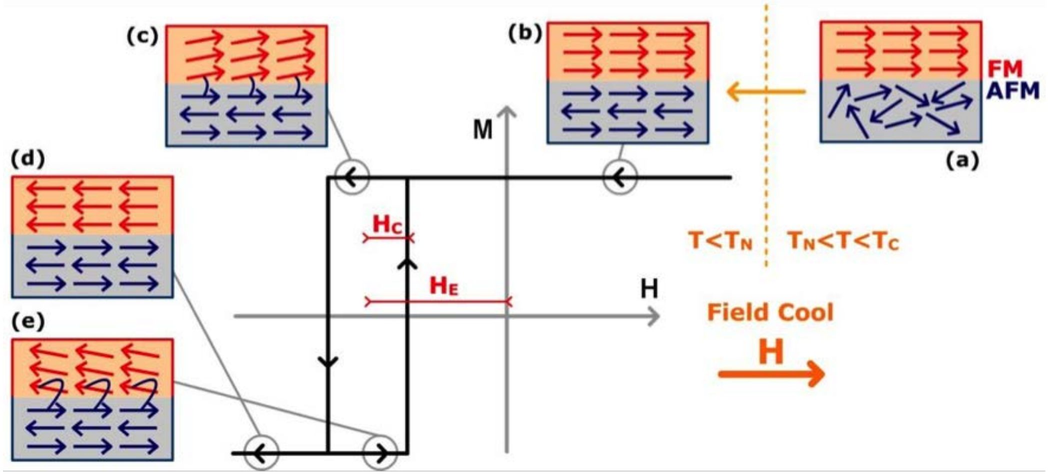

Figure 2.19: Diagram of the spin configuration of a FM/AFM bilayer as a result of a field cooling process. To be noted that spin orientations do not represent the actual behavior of FM and AFM magnetizations [67].

From the energetic point of view, one can refer to the model of Meiklejohn, who first described the exchange bias anisotropy [68], [69]. His model is based on three assumptions: the FM and AFM layers are single magnetic domains; the AFM and FM anisotropy axis are parallel; the interface coupling is FM. In this picture, the Gibbs free energy per unit area of an exchange bias system, assuming coherent rotation of the magnetization, can be written as:

$$g = -HM_{FM}t_{FM}\cos(\theta-\beta) + k_{FM}t_{FM}\sin\beta^2 +$$

$$+k_{AFM} t_{AFM} \sin \alpha^2 - J_{EB} \cos(\beta - \alpha) \tag{2.21}$$

where H is the applied field, M_{FM} and t_{FM} are the magnetization saturation and the thickness of the FM respectively, t_{AFM} is the thickness of the AFM, k_{FM} and k_{AFM} are the anisotropy constants of FM and AFM layers and J_{EB} is the interfacial coupling constant. The angles refer to Figure 2.20: α, β and θ are the angles of M_{AFM}, M_{FM} and H respectively with respect to the anisotropy axis. The first term of the equation accounts for the Zeeman energy, the second and third terms for the FM and AFM anisotropies, the last one for the interfacial coupling. To simplify the expression, often the FM anisotropy can be neglected since $k_{FM} t_{FM} \ll k_{AFM} t_{AFM}$. Then, the expression becomes:

$$g = -H M_{FM} t_{FM} \cos(\theta - \beta) + k_{AFM} t_{AFM} \sin^2 \alpha - J_{EB} \cos(\beta - \alpha) \tag{2.22}$$

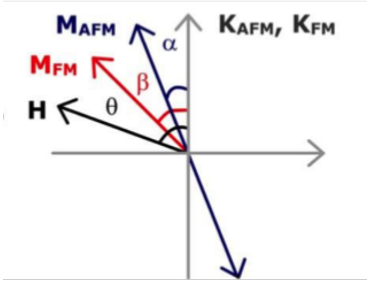

Figure 2.20: Diagram of angles involved in an exchanged bias system.

Now minimizing with respect to α and β, one obtains the expression for the exchange bias field:

$$H_E = \frac{J_{EB}}{M_{FM} t_{FM}} \tag{2.23}$$

It is important to notice that the exchange bias coupling is established only if the condition $k_{AFM} t_{AFM} \geq J_{EB}$ is satisfied. If this is not the case, the AFM sublattices will follow the movement of the FM layer, therefore no shift of the hysteresis loop is observed but only an increase in its coercivity.

As one can see from Eq. 2.23, H_E is inversely proportional to the FM layer thickness, indicating that exchange bias is an interface effect. Instead, the dependence on the AFM thickness is more complex. For thick layers (>20 nm), H_E is basically constant. As the thickness is reduced, H_E dramatically decreases until it goes to zero for few nanometer of thickness (Figure 2.21(a)).

Actually, in our devices, the layers are not single-domain crystals, but consist of a polycrystalline structure. Then in this case, the critical parameter of the AFM is not T_N but the blocking temperature T_B, above which the exchange bias vanishes. The blocking temperature strictly depends on the grain size and on the layer thickness of the AFM material and can be significantly lower than T_N (Figure 2.21(b)).

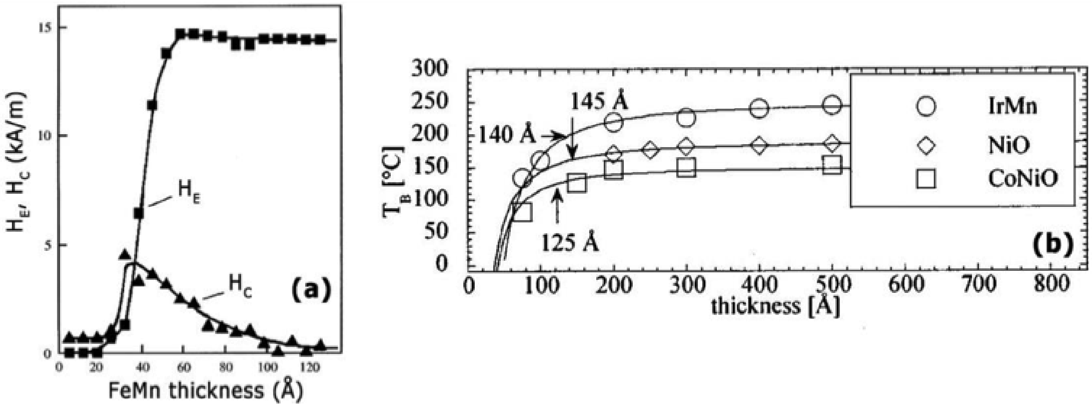

***Figure 2.21**: (a) Plots of H_E and H_C as functions of AFM layer thickness for 7 nm $Fe_{80}Ni_{20}$ on FeMn. From [68]. (b) Dependence of the blocking temperature on the AFM thickness.*

From Eq. 2.23, it is also clear that the exchange bias field is proportional to J_{EB}. If one assumes the magnitude of J_{EB} to be similar to the FM exchange constant, what is found is that H_E results several order of magnitude larger than the experimental results. this simple ideal model, despite providing a useful and intuitive explanation of the phenomenon, does not represent in a proper way the FM/AFM interfacial environment. Meiklejohn's model assumes a perfectly smooth interface and a totally uncompensated spin configuration (Figure 2.22, left panel) at the AFM/FM interface, i.e. it considers all the AFM interfacial spins aligned in the same direction. Since the predictions far exceed the actual exchange bias magnitudes, the totally uncompensated spin configuration seems unlikely. Recently, micromagnetic models have been proposed to study the AFM/FM interface ground spin configuration varying the number of uncompensated moments [70] (Figure 2.22, right panel). It is widely accepted that breaking the in-plane translational symmetry for having uncompensated spins is required to explain exchange bias in most systems [71]. This symmetry breaking can either be the result of interface roughness, magnetic domains, defects, the grain structure, or of a combination of these four factors. Despite the multitude of models developed, the exchange anisotropy remains an open issue especially concerning the interfacial interactions at the atomic scale, which are still unclear. Furthermore, even narrowing down to the macroscopic behavior for having reliable predictions, the general models must be accompanied by considerations about the specific system.

***Figure 2.22**: Spin configuration at a smooth ferromagnet-antiferromagnet interface in case of (left) uncompensated moment structure and (right) compensated moment structure.*

2.3.2 Bilinear coupling

Bilinear coupling or interlayer exchange coupling is the effect responsible for the antiferromagnetic coupling of two FM layers separated by a non-magnetic spacer as first described by Grunberg in 1986 [72]. Its name derives from the fact that the coupling energy per unit area is proportional to both the magnetizations of the FM layers $\boldsymbol{m}_i$:

$$\frac{E}{A} = -J\boldsymbol{m}_1 \cdot \boldsymbol{m}_2 \tag{2.24}$$

where J is a parameter given by the difference in energy between the antiparallel and the parallel alignment of the magnetizations:

$$J = \frac{1}{2A}(E_{AP} - E_P) \tag{2.25}$$

where A is the exchange stiffness. With this form of the interaction expression, positive (negative) values of the coupling constant J favor parallel (antiparallel) alignment of the magnetizations.

Parkin discovered that the sign of J and, as consequence, the preferred alignment of the ferromagnets magnetizations oscillate as a function of the spacer thickness as shown in Figure 2.23 [73]. Several models were proposed in order to explain the interlayer exchange interaction and in 1993 the *quantum well model* allowed a unification of the previous works [74], [75].

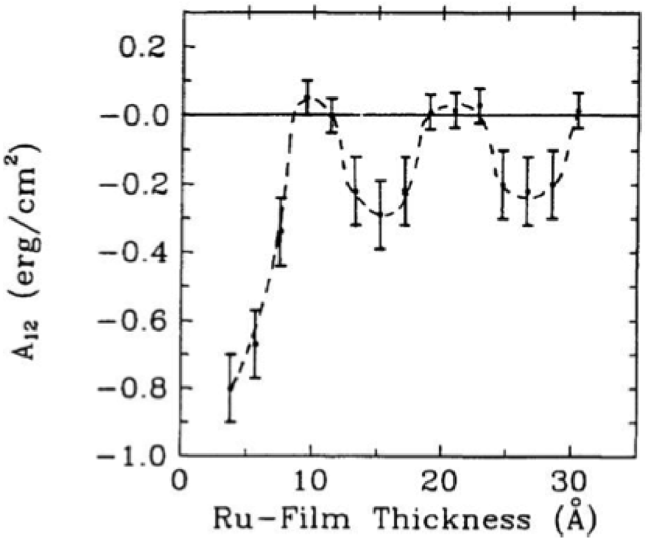

Figure 2.23: *Determined values of the interlayer exchange stiffness, A_{12}, as a function of the Ru layer thickness in Co/Ru superlattices deposited by magnetron sputtering. From* [76].

Such model is based on spin-dependent reflection of electrons at the boundaries of the spacer metal with the ferromagnetic layers. The conduction electrons are confined in the spacer and this leads to a modification of the density of states in the spacer and to a change in the system energy (Figure 2.24).

The reflection coefficients are spin-dependent and consequently, the change in energy will be different for ferromagnetic and antiferromagnetic alignment of the magnetizations of the two ferromagnetic layers. In this framework, the oscillatory behavior of the coupling is due to the change in the energy and occupation of quantized states with the thickness of the spacer, which causes alternatively the parallel or the antiparallel configurations to have the lowest energy.

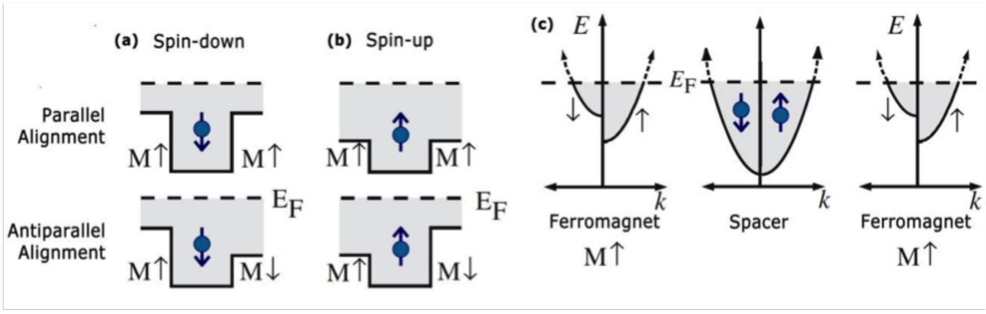

Figure 2.24: *Spin-dependent quantum wells seen by a spin-up (a) and spin-down (b) confined electron for parallel and antiparallel magnetizations of the ferromagnetic layers. In (c) the spin-split bandstructure for the ferromagnetic layers and the spin-independent one of the spacer.*

2.3.3 Superparamagnetism

In the sub-micron size range, magnetic objects are often in a single domain configuration. In the simplest approximation, a single domain particle with uniaxial anisotropy have two possible magnetization state: parallel or antiparallel to the direction of the easy axis. These two state are separated by an energy barrier, which is related to the anisotropy of the material and is a function of the angle between the magnetization and the easy axis:

$$E(\theta) = kV\sin^2\theta \tag{2.26}$$

where k is the material anisotropy constant and V is the volume of the particle.

If the activation energy kV, necessary to rotate the magnetization from $\theta = 0$ to $\theta = \pi$, is comparable with the thermal agitation energy $k_B T$, the particle does not stay frozen in one configuration but continuously flips from one configuration to the other (Figure 2.25(a)). The average time between two consecutive flip events is:

$$\tau = \tau_0 \exp\left(\frac{kV}{k_B T}\right) \tag{2.27}$$

with k_B is the Boltzmann constant, T the absolute temperature and τ_0 a time constant of the order of 10^{-9}-10^{-10} s for non-interacting particles. This is also the relaxation time in response to an applied magnetic field.

As the particle size is reduced, the energy barrier decreases and the rate of switching goes up. When $\frac{kV}{k_B T} = 25$, the switching time goes below 1 s and the particles are called superparamagnetic. The diameter at which a particle becomes superparamagnetic lies in the 5-10 nm range. In this condition, the magnetic moment of the particle, as a whole, is free to fluctuate in response to the thermal activation, while the individual atomic moments maintain their ferromagnetic state relative to each other.

The occurrence of superparamagnetism depends on the temperature as well as on the experimental observation time. The superparamagnetic blocking temperature T_B of a particle is defined as the temperature at which the superparamagnetic relaxation time equals the observation time of the experiment. Below the blocking temperature, the ferromagnetic order appears because the magnetization relaxation process becomes slow in comparison to the time required by a particular investigation technique. In absence of external magnetic field, the resulting fluctuations in the direction of the magnetization cause the total magnetic moment average to be zero. This means that superparamagnetic particles have no remnant magnetization and, when inserted in a field, their magnetic moment will tend to align to the field lines. In addition, in contrast to paramagnetic materials, whose relative magnetic susceptibility is significantly lower, the magnetization of superparamagnetic materials can easily attain at saturation (M_S) values comparable to those of ferromagnetic materials (Figure 2.25(b)).

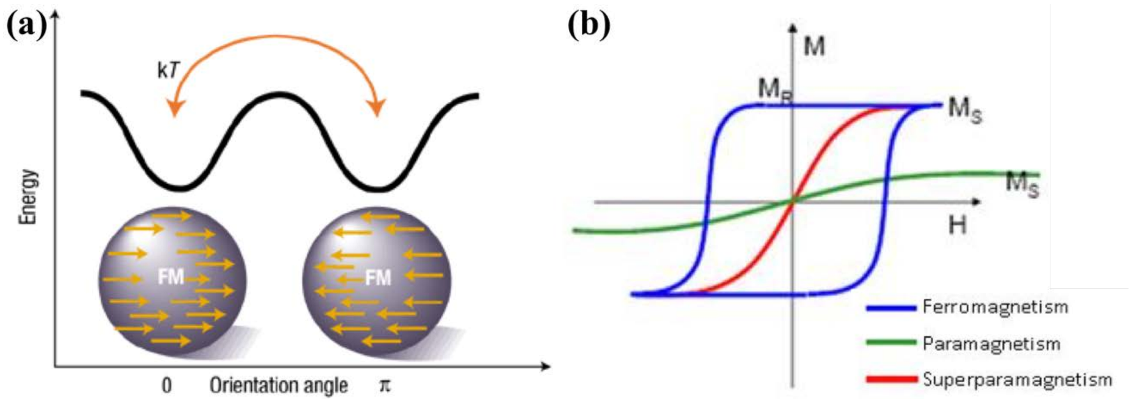

Figure 2.25: *(a) Flipping of the magnetization between the two magnetic configurations due to thermal fluctuation. (b) Comparison of the M vs H behavior between ferromagnetic, superparamagnetic and paramagnetic regimes [77].*

Superparamagnetism is observed also in magnetic thin films, below a critical thickness, which depends on the material, deposition conditions and the substrate on which it is grown. The weakening of ferromagnetism in thin films can be attributed to different mechanisms. As a thin film transitions from three-dimensional to two-dimensional ferromagnetism, the magnetic ordering temperature T_C is often reduced. If a thin film's T_C drops below room temperature, the measured room temperature coercivity of the hysteresis loop will vanish. On the other hand, when a thin enough film is deposited, it can form magnetic islands or clusters rather than a continuous film. These magnetic clusters will be superparamagnetic as long as the ambient thermal energy is large enough to cause relaxation of the magnetization vectors of the clusters.

In this thesis work, superparamagnetism in thin $Co_{0.4}Fe_{0.4}B_{0.2}$ layers (few nm) grown on MgO is exploited, together with the shape anisotropy in order to have a linear and hysteresis-free sensor response [78].

2.4 Sensor response

The magnetic response of a material is the result of many competing physical processes. The easiest way for predicting the magnetization *M(H)* of a material under the influence of an external field is to find its equilibrium configurations. This can be done summing all the energy contributions to the system, namely the exchange energy, magnetocrystalline anisotropy, magnetostatic interaction and Zeeman energy, and then minimizing the expression with respect to $\boldsymbol{M}$.

The exchange interaction lies at the heart of the phenomenon of long range magnetic order. It is described by the Heisenberg Hamiltonian:

$$H = -\sum_{i \neq j = 1}^{N} J_{ij} \boldsymbol{S_i} \boldsymbol{S_j} \tag{2.28}$$

where S_i is the spin angular momentum of the ion localized in the lattice position i and J_{ij} is the exchange constant between the i and j moments. Usually, in cubic crystals, the exchange integral decreases rapidly as the distance between atoms increases, so the sum is performed only among first neighbors.

The magnetocrystalline anisotropy gives rise to a magnetic easy axis and a hard axis in crystals: along certain crystallographic directions, it is easier to magnetize the crystal than along others. This fact has a major influence on the shape and properties of the hysteresis loop of the magnetization. The magnetocrystalline anisotropic energy is defined as the work needed to align the magnetization along one direction starting from the easy axis. In the system with only one preferred direction (uniaxial anisotropy), the energy density E/V can be written as a power series of $sin\theta$, where θ is the angle between the magnetization and the preferential direction of the crystal z [79]:

$$\frac{E}{V} = k_0 + k_1 \sin^2 \theta + k_2 \sin^4 \theta + \cdots \tag{2.29}$$

where k_0, k_1 and k_2 are the anisotropy constants and θ is the angle between the magnetization and the preferential direction of the crystal z. If $k_1 > 0$ the energy is minimized when moments align along z, which becomes the easy-axis; if $k_1 < 0$ there is an easy-plane where the energy is equally low perpendicular to z. The anisotropy constant k is related to the anisotropic field by $H_k = 2k/(\mu_0 M_S)$.

An additional energy term is due to the magnetostatic interaction between the magnetic moments and the dipolar field created by the neighboring moments. When the sample has finite dimensions, magnetic poles form at the surface giving rise to a stray field outside and inside the material. The lowest energy configuration is the one minimizing this stray field by confining it in the sample, in a sort of closed flux configuration, according to the general expression for the magnetostatic energy:

$$E = -\frac{\mu_0}{2} \int_{all\ space} H^2\, dV \tag{2.30}$$

The presence of magnetic domains in the system is mainly the result of the competition between the exchange interaction and magnetic anisotropy, which tend to align the moments, and the magnetostatic interaction, which tries to minimize the stray field favoring close paths for the magnetization inside the material, as shown in Figure 2.26. This results in the formation of the so-called magnetic domains, regions in which the atomic magnetic moments are aligned.

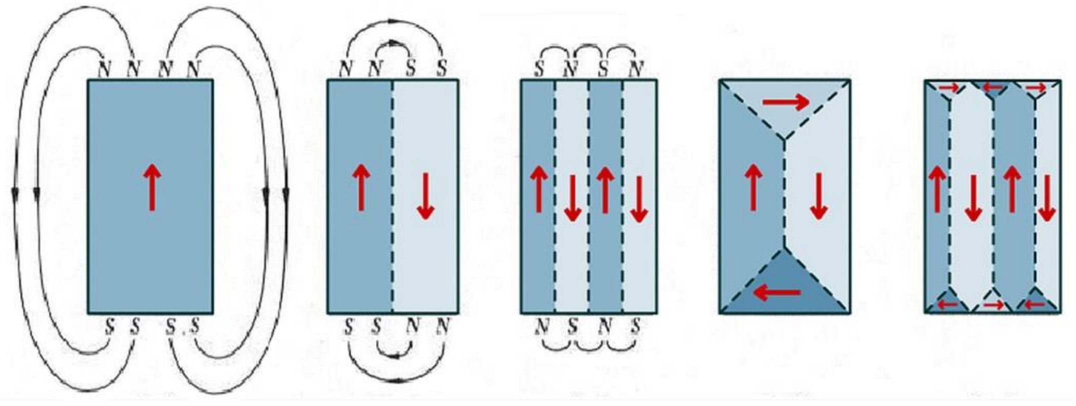

Figure 2.26: *Domain formation: from left to right, reduction of the stray field and of magnetostatic energy by domain creation.*

For magnetic bodies with second order surface the demagnetizing field can be expressed through the following relation: $\boldsymbol{H_D} = N \cdot \boldsymbol{M}$, where $\boldsymbol{M}$ is the magnetization vector and N the demagnetizing tensor, which is strongly related to the shape of the material. The shape dependence of the demagnetizing field can be exploited in patterned systems for inducing shape-dependent preferential directions for the magnetization, i.e. the so-called shape anisotropy. In general, the demagnetizing field will be stronger along the direction corresponding to a small extension of the sample, because the stray field to counteract is larger. On the contrary, the magnetization will be forced to align along the long side of the sample. This is also the reason why thin-films usually show preferentially in-plane magnetization.

The Zeeman energy is the one possessed by the sample in an external applied field $\boldsymbol{H}$. This can be expressed as:

$$E = -\mu_0 \int_V \boldsymbol{M} \cdot \boldsymbol{H} dV \tag{2.31}$$

where $\boldsymbol{M}$ is the magnetization and V the sample volume.

The transfer curve of a magnetoresistive (MR) sensor is the resistance response obtained by applying a voltage across the system while varying the magnetic field. If θ is the angle between the magnetization directions of the ferromagnetic electrodes, the total resistance of the sensor is given by:

$$R(\theta) = \frac{R_P + R_{AP}}{2} + \frac{R_P - R_{AP}}{2} \cos\theta \tag{2.32}$$

For sensing applications, a linear sensor response with low hysteresis is favorable because it enables a straightforward relationship between changes in the external magnetic field and changes in the electric signal acquired from the sensor. Since the magnetization of the bottom magnetic layer is pinned and thus insensitive to the external magnetic field, in order to obtain this kind of response $R(H)$, the magnetization of the free layer should vary linearly with the magnetic field, which means that $cos\theta$ must linearly vary with $\boldsymbol{H}$.

The sensor sensitivity S_{sens}, which corresponds to the slope of the transfer curve, is a critical parameter that characterizes MR sensor and is defined as:

$$S_{sens} = \frac{dR}{R_0} \frac{1}{dH} \tag{2.33}$$

where R_0 is the resistance at zero external field, dR is the sensor resistance change for an external field variation dH.

Maintaining high field sensitivity with reduced hysteresis is a challenge for devices with linear response. This can be achieved by controlling the shape anisotropy or changing the free layer thickness, at the cost of a smaller MR ratio.

The conditions for a linear transfer curve of a MR sensor are described through energy terms calculations, under the assumption that the free layer is a single magnetic domain and thus the magnetization rotates uniformly with the external field. The total energy of the free layer is given by the sum of:

-Zeeman term: $-\mu_0 \boldsymbol{H} \cdot \boldsymbol{M_S^f}$.

-Magnetocrystalline anisotropy term: $k \sin^2 \theta$ in case of parallel anisotropies and $k \cos^2 \theta$ in the case of crossed anisotropies.

-Demagnetizing field of the free layer which is the field produced inside the material to counteract the stray field and can be included as a Zeeman-like term: $-\frac{\mu_0}{2} \boldsymbol{H_d^f} \cdot \boldsymbol{M_S^f}$ where $\boldsymbol{H_d^f}$ is the demagnetizing field of the free layer.

-Demagnetizing field of the pinned layer that similarly to the previous term accounts for $-\mu_0 \boldsymbol{H_d^p} \cdot \boldsymbol{M_S^f}$ where $\boldsymbol{H_d^p}$ is the demagnetizing field of the pinned layer.

-Néel coupling term: $-\mu_0 \boldsymbol{H_N} \cdot \boldsymbol{M_S^f}$ where $\boldsymbol{H_N}$ is the Néel coupling field.

2.4.1 Parallel anisotropies

Let's consider the case in which both the pinned and the free layers have the easy axes induced by the magnetocrystalline anisotropy along the short edge of a rectangle Figure 2.27(a). This condition can be easily obtained in sputtered system by applying a magnetic field during the growth.

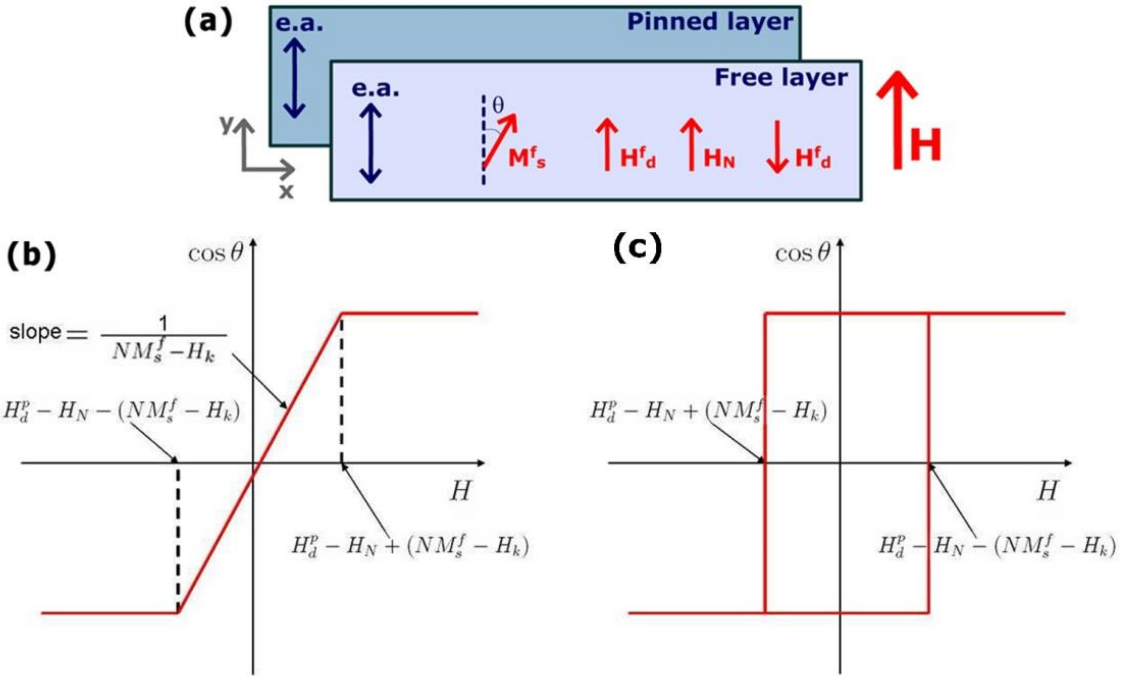

Figure 2.27: *(a) Sketch of rectangular-shaped pinned and free layers with parallel magnetocrystalline anisotropies. "e.a." indicates the easy axis directions. (b) Free layer response*

curve if $H_k < N \cdot M_S^f$*; the response is linear and shows no hysteresis; (c) if* $H_k < N \cdot M_S^f$*, the response is hysteretic. Adapted from* [80].

The total energy of the free layer is given by:

$$E^f = -\mu_0 \boldsymbol{H} \cdot \boldsymbol{M_S^f} + k \sin^2 \theta - \frac{\mu_0}{2} \boldsymbol{H_d^f} \cdot \boldsymbol{M_S^f} - \mu_0 \boldsymbol{H_d^p} \cdot \boldsymbol{M_S^f} - \mu_0 \boldsymbol{H_N} \cdot \boldsymbol{M_S^f} \qquad (2.34)$$

The energy minima and thus the stable magnetic configuration for each value of the external field can be obtained by setting $\frac{\partial E^f}{\partial \theta} = 0$ and $\frac{\partial^2 E^f}{\partial \theta^2} > 0$:

$$if\ H_k < N \cdot M_S^f \Rightarrow \begin{cases} \theta = 0, & H > H_0 \\ \cos\theta = \dfrac{H - H_d^p + H_N}{N \cdot M_S^f - H_k} & \\ \theta = \pi, & H < H_\pi \end{cases} \qquad (2.35)$$

$$if\ H_k > N \cdot M_S^f \ \Rightarrow \begin{cases} \theta = 0, & H > H_0 \\ \theta = \pi, & H < H_\pi \end{cases} \qquad (2.36)$$

where $H_{0\,(\pi)} = H_d^p - H_N + (-)\left(N \cdot M_S^f - H_k\right)$.

Figure 2.27(b)-(c) shows the response curves for linear (Eq. 2.35) and hysteretic (Eq. 2.36) cases respectively. It is worth noting that the Néel field and the demagnetizing field of the pinned layer ($H_d^p - H_N$) shift the curve, while the competing effects of the shape anisotropy and the magnetocrystalline anisotropy ($N \cdot M_S^f - H_k$) determine the shape and the limits of the curve. In fact, the shape anisotropy favors an alignment parallel to the long edge of the rectangle, whereas the magnetocrystalline anisotropy induces an easy axis along the short edge.

As earlier said, the solutions are valid under the assumption that the free layer is a single magnetic domain and thus the magnetization rotates uniformly with the external field. In layers with small lateral dimensions (< 500 nm), this is a good assumption because the energy cost of domain formation is too high and the layers will be essentially "single domain". For larger areas, these results should be treated carefully, and integrated with specific micromagnetic simulations for providing more reliable results.

2.4.2 Crossed anisotropies

In this case the total energy of the free layer is:

$$E^f = -\mu_0 \boldsymbol{H} \cdot \boldsymbol{M_S^f} + k \cos^2 \theta - \frac{\mu_0}{2} \boldsymbol{H_d^f} \cdot \boldsymbol{M_S^f} - \mu_0 \boldsymbol{H_d^p} \cdot \boldsymbol{M_S^f} - \mu_0 \boldsymbol{H_N} \cdot \boldsymbol{M_S^f} \qquad (2.37)$$

Minimizing the energy, the following solutions are obtained:

$$\begin{cases} \theta = 0, & H > H_0 \\ \cos\theta = \dfrac{H - H_d^p + H_N}{N \cdot M_S^f + H_k} & \\ \theta = \pi, & H < H_\pi \end{cases} \tag{2.38}$$

In this case. the only possible solution is a linear magnetic response because the shape and magnetocrystalline anisotropies are not competing factors but they both favor the alignment along the same direction. Indeed, this is the configuration exploited in this work in order to realize magnetic field sensors.

Chapter 3: Experimental methods

In this chapter the main experimental methods used during this thesis work are presented.

3.1 Magnetron sputtering

Magnetron sputtering is a physical vapor deposition technique. It is a versatile technique which allows a good film adhesion to the substrate and a high control on thickness, uniformity and composition of the deposited material. Furthermore, materials with high melting point and low vapor pressure can be sputtered as well, while it is very difficult with other evaporation methods.

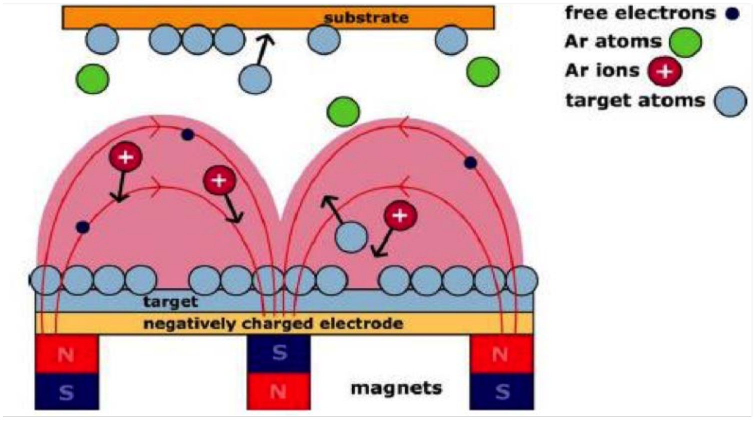

Figure 3.1: Schematic illustration of how the process works.

Into the sputtering chamber, a plasma of an inert gas (usually Ar) is ignited. The plasma is kept on by a cascade process: Ar^+ ions and free electrons continuously collide with Ar atoms generating more ions and electrons. Plasma ions are then accelerated towards the source material (also called target) and atoms or cluster of atoms are ejected due to moment transfer. The ejected material follows a ballistic trajectory until it reaches the substrate, such as a Si wafer. Since any unwanted particle could scatter the target atoms reducing the deposition rate, the sputtering chamber requires High Vacuum (HV) regime, about 10^{-9} Torr.

The peculiarity of magnetron sputtering is that plasma is confined in a small region around the target. This is achieved by means of an intense magnetic field to curve the trajectories of charged particles (electrons and ions) which therefore remain close to the target.

The first advantage of this configuration is that the probability of ionization strongly increases allowing a lower partial pressure of Ar to ignite the plasma. Moreover, the density of the plasma is orders of magnitude higher with respect to other technique so that the erosion velocity increase and so does the deposition rate. Lastly, the localization of the plasma prevents the substrate and the walls of the chamber from being eroded.

A particular care must be taken when insulating or ferromagnetic targets are used. In the former case, charging effects obstruct the erosion mechanism. To avoid this problem, the target is biased with RF power so that the fast changing of polarization prevents charge build-ups. But in this circumstance a high-pressure Ar strike is required to ignite the plasma. In the second case, the problem lies in the stray magnetic field leaking from the target. To counteract this field, a specifically designed magnet is placed behind the target.

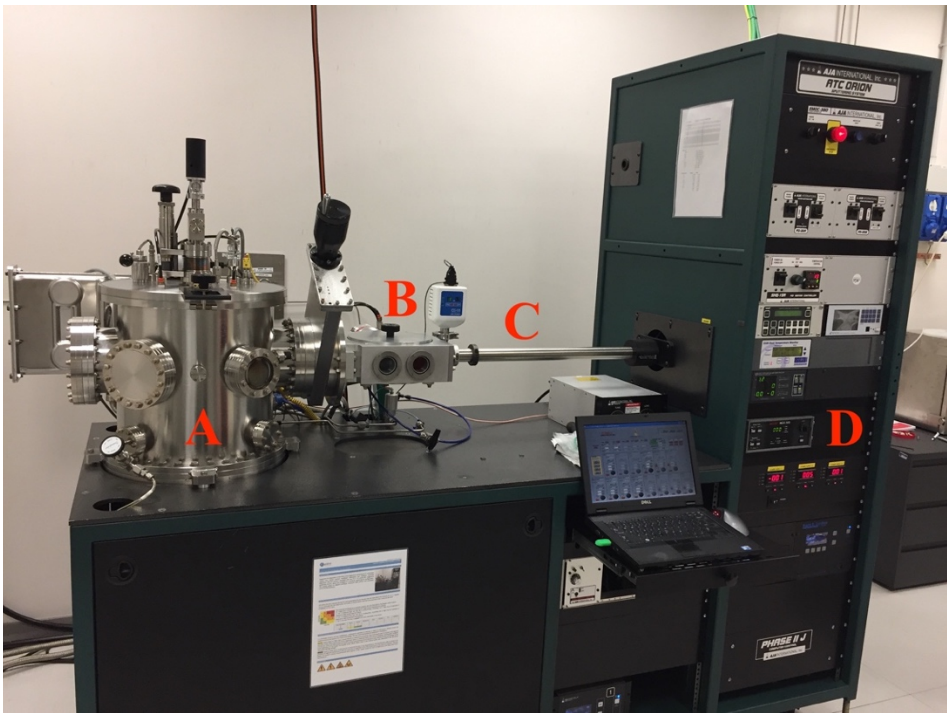

***Figure 3.2:** AJA ATC Orion magnetron sputtering system. (A) Deposition chamber. (B) Load-lock chamber. (C) Transfer arm. (D) Generators and controllers.*

In this work, the sputtering has been performed with an AJA ATC Orion system (Figure 3.2). This machine is presented with 10 different sources which are arranged in a specific circular pattern so that they all point to the substrate placed in the common focal point. The targets are located at the bottom of the chamber in the so-called sputtering-up configuration. In such a configuration, the sputtered material travels upwards, preventing downfall on the substrate and giving a cleaner sample with respect to sputtering-down systems. On the other hand, material redepositing on the surface of the target can produce shortcuts of the guns and a specific cleaning procedure of the chamber after a long period of use is recommended. The AJA system can perform either DC sputtering of Ru, Ta, $Ir_{0.2}Mn_{0.8}$, Ti, Au and $Co_{0.4}Fe_{0.4}B_{0.2}$ or RF sputtering of SiO_2, MgO, Al_2O_3 and $Co_{0.6}Fe_{0.4}$. The deposition chamber is kept in HV (~10^{-9} Torr) by a cryopump. The substrate holder allows to adjust the substrate-target distance, the latter affecting uniformity and deposition rate. Moreover, during the process the holder is kept in rotation to further guarantee a high uniformity of the film. A permanent magnet (H ~ 300 Oe) can be added to the sample holder in order to induce a uniaxial anisotropy direction in the ferromagnetic films. The substrate is inserted into the deposition chamber through an introduction chamber which is turbo-pumped down to 10^{-6} Torr and connected to the main chamber. This is necessary to keep the main chamber as clean as possible.

The whole deposition process is remotely controlled by the Phase II Labview software which can be operated in both manual and automatic modes. In the former the parameters are set real-time during the deposition, while in automatic mode they are saved in a file recalled during the process allowing high reproducibility. The calibration of deposition rates is performed with a quartz micro-balance mounted on the side of the main chamber. Its working principle is based on the shift of the resonance frequency of a quartz crystal due to the deposition of new material.

An alternative to the AJA machine is the Leybold-Heraeus LH Z400 MS (Figure 3.3). It is a magnetron sputtering with three available targets and the possibility to insert different gases into the chamber. Since the distance target-sample is lower and the targets are bigger with respect to the AJA system, the Leybold system is employed for long and quantitatively demanding depositions.

Figure 3.3: *Leybold-Heraeus LH Z400 MS magnetron sputtering.*

3.2 Optical lithography

Optical lithography is a widespread microfabrication process combining high throughput to high resolution (below 1µm, depending on the wavelength of light source and mode employed). With this technique, a geometric bi-dimensional pattern is transferred from a template, the mask, to the sample thanks to the photoresist, a light-sensitive polymer previously deposited onto the surface of the sample.

The photoresist has the property to change its solubility upon exposure to UV light. It is made up of three components: a resin, accounting for mechanical and chemical properties, a sensitizer, the photoactive compound, and a solvent, which keeps the polymer in liquid form. A photoresist can be positive or negative, if made soluble or insoluble by UV radiation, respectively. In the first case the light triggers a photochemical reaction that causes the splitting of polymer chains, thus enhancing solubility and consequent removal. In the other case, the exposure promotes cross-linking between chains making the region less soluble than unexposed ones. The difference in solubility between exposed and non-exposed regions is called contrast and it is an important parameter of the photoresist.

There are direct and image reversal photolithography. The former yields an exact copy of the mask, while the latter gives a negative image of the pattern.

3.2.1 Direct lithography

The lithographic process consists of many steps (Figure 3.4). In the following paragraph, each step will be described.

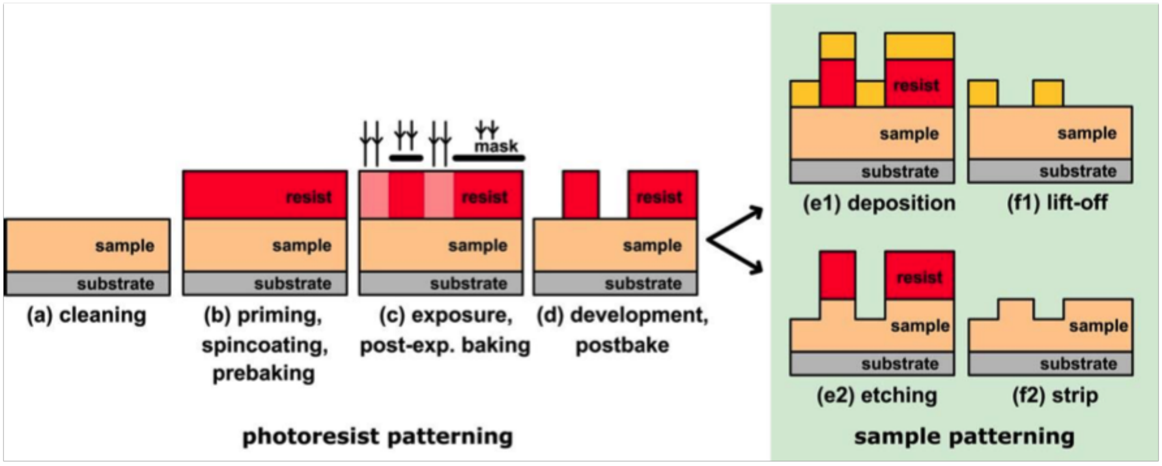

Figure 3.4: *Main steps of direct optical lithography with positive resist.*

-Cleaning and preparation of the sample: the presence of organic or inorganic contaminants on the substrate surface can compromise the adhesion and then the pattern transfer. The standard cleaning procedure consists of an ultrasonic bath in acetone followed by an isopropanol rinsing to remove all the residual and avoid the formation of halos on the surface. The sample is then dried in N_2.

Since the photoresist is a non-polar compound, a better adhesion is achieved on hydrophobic surfaces. In order to promote hydrophobicity, an additional layer of Primer can be deposited on the sample in the same way as the polymer. An alternative to chemical priming is etching. In this case, mechanical adhesion is obtained inducing micro-roughness on the surface.

-Spinning process: in order to obtain a uniform resist film, the deposition occurs via spin coating. Some drops of resist are dispensed on the sample. Then it is put in rotation at high speed, around 5000 rpm, so that the coating material is spread uniformly over the surface by centrifugal force. The final thickness t of the film depends on the angular speed of rotation ω and the viscosity of the polymer η according to the empirical formula:

$$t = K\frac{C^{\alpha}\eta^{\beta}}{\omega^{\delta}} \tag{3.1}$$

where K, α, β, η are parameters related to the employed system.

After the spin coating, a soft baking seconds eliminates the casting solvent containing the polymer, allows to reduce the mechanical stress induced by the spinning and enhances the resist adhesion to the substrate.

In this work the positive photoresist AZ5214E is employed.

-UV exposure: there are three possible modes of exposure as shown in Figure 3.5:

- Contact printing: the mask is put in contact with the resist on the sample. It guarantees the best resolution but both the mask and the sample can get dirty during the process;
- Proximity printing: a small gap separates the photomask and the substrate. Resolution is slightly worse due to diffraction;
- Projection printing: the mask is far from the substrate and an objective lens is used to focus the light on the sample counteracting the diffraction.

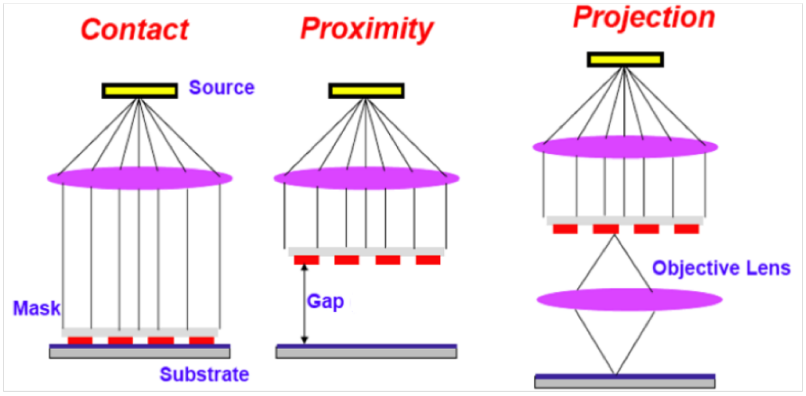

Figure 3.5: *The three modes for light exposure in optical lithography: contact, proximity and projection.*

The maximum achievable resolution is indicated as critical dimension (CD) and corresponds to the linear dimension of the smallest object that can be transferred. The resolution is limited by diffraction and affected by the quality of the mask and the contrast of the photoresist. In case of contact printing the limit is CD ~ λ.

The mask used to transfer the image is made up of quartz and patterned with a thin Cr layer. The metalized regions absorb the radiation, preventing the underlying resist from chemical modifications so that, after the light, a copy of the pattern is left. To correctly align the mask to the substrate, a mask-aligner system is employed. In this work the Karl Suss MA6 (Figure 3.6) is used. It allows to perform both contact and proximity printing on different sizes of mask (5” or 7”) and substrate (up to 6”). The UV radiation comes from 1000 W mercury arc lamp and in particular the Hg I line ($\lambda = 365$ nm) is exploited.

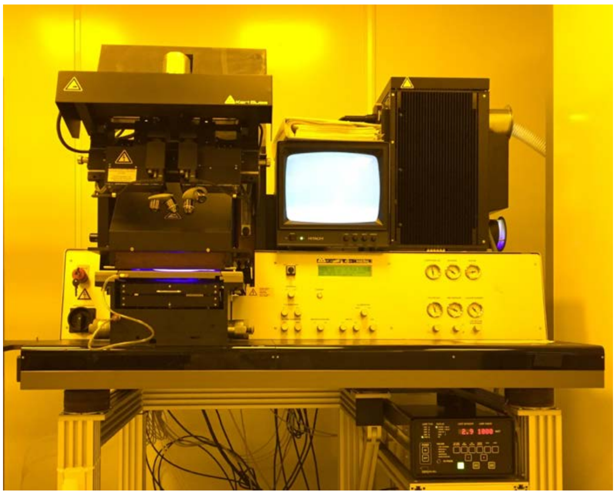

Figure 3.6: Karl Suss MA6.

-**Resist development:** during this phase, a suitable solvent, the developer, removes the positive resist made soluble by light, leaving the unexposed material unchanged. In case of negative photoresist, the opposite mechanism would occur. The solvent used to develop the AZ5214E is the AZ726MIF.

-**Sample patterning:** once the unwanted resist has been removed, the sample can be further processed in two ways:

- Subtractive process: material from the sample is removed, for example through ion beam etching, described in detail in the next paragraph. In this case the resist protects the underlying material from erosion.
- Additive process: new material is added, for example by magnetron sputtering, on the region not covered by the resist.

At the end of the processing, the residual resist is definitely removed in the so-called “stripping” or “lift-off”, using a suitable solvent, the AZ 100 Remover.

3.2.2 Image reversal lithography

In order to facilitate the lift-off procedure, it is desirable to have slits in the newly deposited material so that the solvent can easily reach the lowest layers of resist causing its detachment from the sample. Such favorable profile is obtained with a negative resist or an image reversal of the positive resist. In this work the latter is used.

As shown in Figure 3.7(a-d), the only differences with respect to the direct process lay in the exposure step. Once UVs light the sample, a post-exposure baking causes cross-linking of the exposed polymer making it insoluble and insensitive to further irradiation. The sample is then exposed to UV light without any mask performing the so-called flood exposure. In this way, the resist that was not exposed in the previous step becomes soluble. As a result, the image contrast of the mask is reversed on the sample and an undercut profile (walls inclined more than 90°) is obtained, providing the slits to facilitate the lift-off.

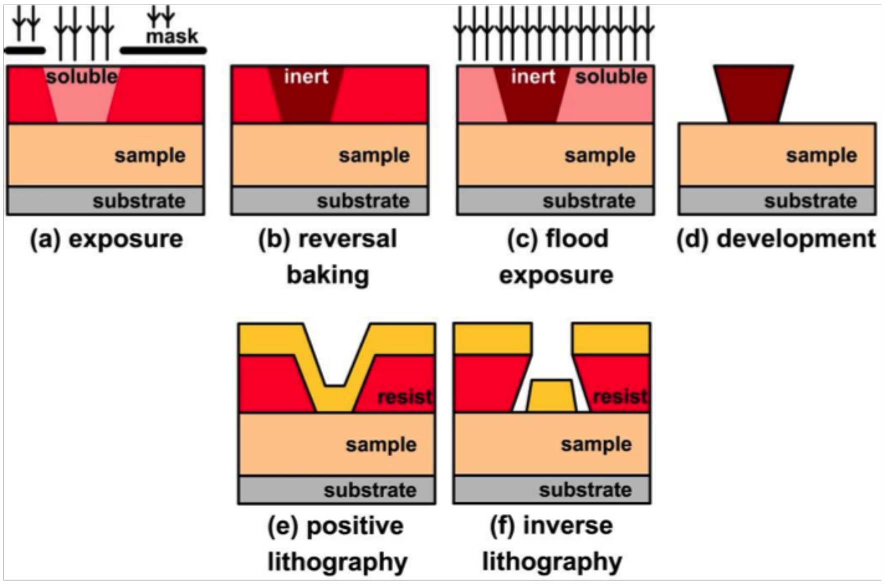

Figure 3.7: *Exposure step of an inverse photolithography (a-d). In e and f a comparison between overcut and undercut effects on deposition is reported. The undercut profile makes it easier for the solvent to reach the resist.*

3.3 Ion beam etching

Ion Beam Etching (IBE) is a physical dry etching technique where Ar+ ions are accelerated towards the sample in a vacuum chamber. As for the magnetron sputtering, material from the sample is removed by energy transfer between Ar^+ ions and atoms on the surface. Ar+ ions are generated from inert Ar gas through a discharge current. Here, a filament run by current, which is the cathode, emits electrons by thermoionic effect. These electrons, accelerated towards the anode by the potential difference between the electrodes (discharge voltage), hit and ionize the Ar atoms giving rise to Ar+ ions and free electrons. These free electrons, which are also accelerated by the potential difference, contribute to maintain the plasma. Some of the Ar+ ions are then accelerated toward the sample by a grid set at a negative potential (accelerator voltage).

Figure 3.8 shows the Sputtering and Ion Beam Etching Kenosystec VS80, which is used for IBE during this thesis. The VS80 system consists of a chamber for sputtering and ion beam etching processes, equipped with different sputtering sources and an ion beam etching source (KDC 160 Ion Source). A fast entry chamber is employed for fast insertion and extraction of samples. The sample holder can fit samples up to 6” diameter and is mounted on a motorized stage that can be translated, rotated and tilted in front of the etching/sputtering sources, in order to ensure uniform ablation/deposition over the whole sample area. Usually during operations, a tilting angle of 30° or 60° is recommended to avoid re-deposition of etched material.

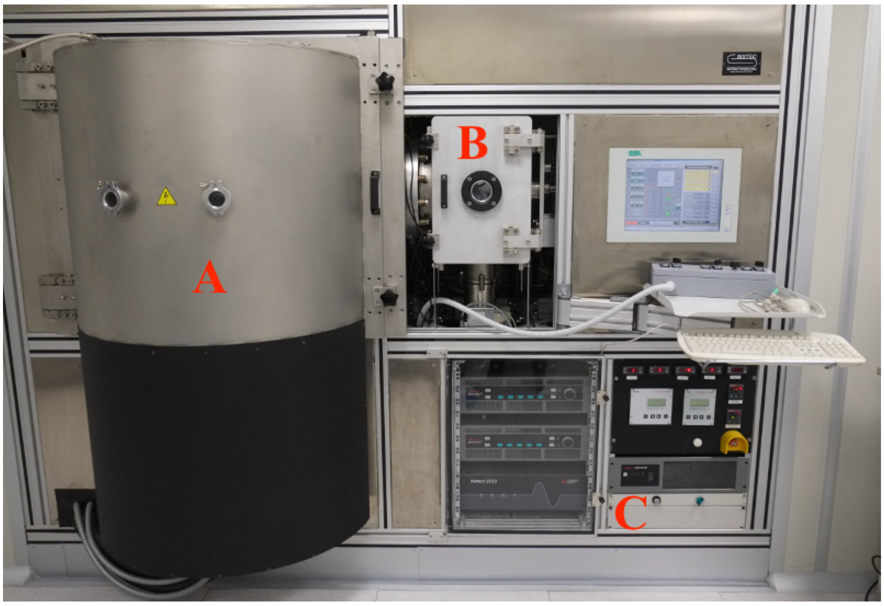

Figure 3.8: *Ion Beam Etching Kenosystec VS80. (A) Main chambers. (B) Load-lock chamber. (C) Generators and controllers.*

The etching rate depends on many factors, including the etched material. If the sample, as in this case, consist of a multilayer stack of different materials with different growth conditions, it is rather complicated to precisely calculate the etching time. This is why a visual method based on calibration samples is employed to determine the duration of the process (Figure 3.9). The calibration sample is an exact replica of the structure to be etched, grown on a transparent glass substrate. Calibration and real sample are mounted together on the holder of the machine to ensure the same etching conditions. When the transparent substrate becomes visible as in Figure 3.9(c), the process is stopped. In this way one is sure that the corresponding material of the sample has been removed.

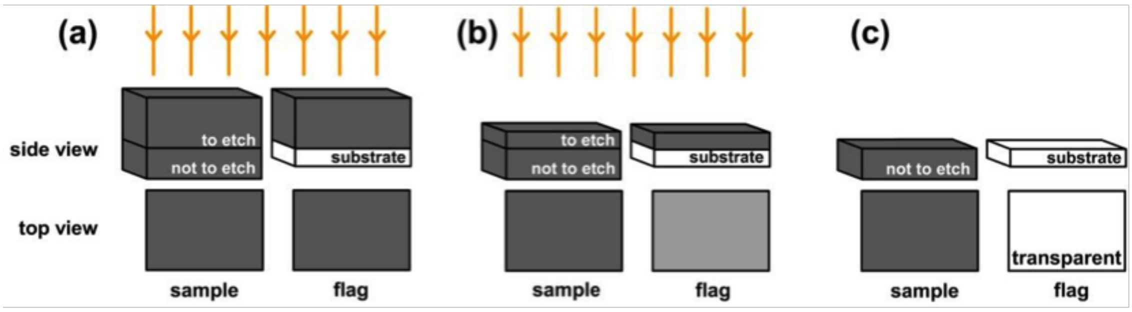

Figure 3.9: *Visual method based on the use of flags to determine the etching duration.*

3.4 Field annealing in vacuum

As explained in the previous chapter, the magnetic sensor needs to be annealed before the use. Care must be taken during this process since excessive annealing temperature or time can damage the sensor. The experimental setup for vacuum field annealing is shown in Figure 3.10. It consists of a vacuum chamber, pumped by a turbopump down to 10^{-6} mbar, to which a transparent quartz bulb, where the sample is placed, is connected. The bulb contains a holder with a resistive filament. The sample is glued to a boron nitride tablet with a thermally conductive silver paste, then placed on the holder and heated by the filament through Joule effect. The current flowing into the filament is supplied by a DC generator and regulated by a PID controller, which receives the feedback from a thermocouple in thermal contact with the sample. At the end of the process the sample cools down mainly via irradiation, since in vacuum there is no convection and the heat conduction through the holder is negligible. During the annealing, the magnetic field is provided by a permanent magnet that generates an approximatively uniform film of ~4 kOe, strong enough to align the magnetization of the structure.

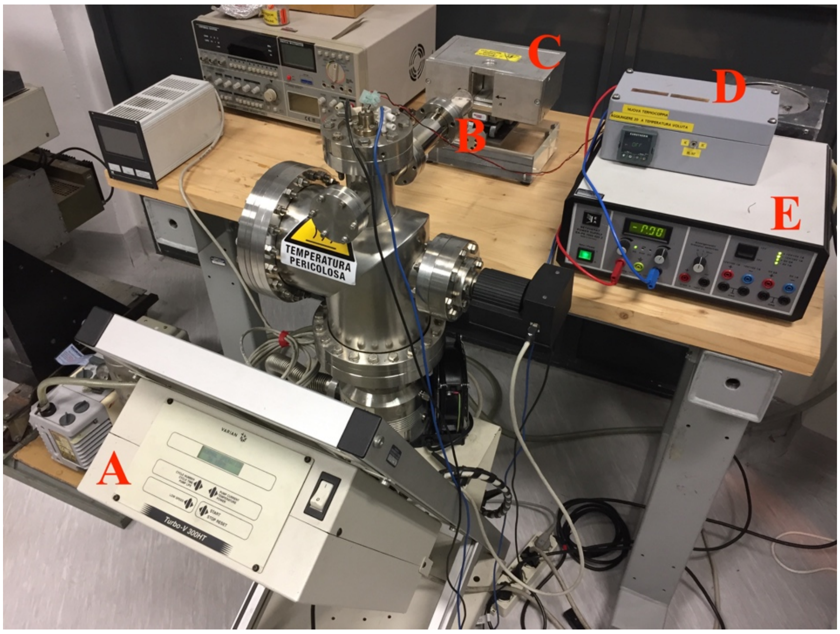

Figure 3.10: *Field annealing setup. (A) Turbopump. (B) Sample holder. (C) Permanent magnet. (D) PID controller. (E) DC generator.*

3.5 VSM

The VSM is a magnetometry technique allowing to measure the magnetization of a sample when it vibrates perpendicularly to a uniform magnetic field [33]. As shown in Figure 3.11, the sample is placed between the two poles of an electromagnet and a pair of pick-up coils, and it is mechanically put in vibration in the transversal direction. The measurement is based on Faraday’s law of induction, that is the evaluation of the voltage induced in the detection coils by a time-varying magnetic flux:

$$\nabla \times \boldsymbol{E}$$

$$= -\frac{\partial \boldsymbol{B}}{\partial t} \qquad (3.2)$$

When placed in a uniform magnetic field **H₀**, the sample acquires a magnetization **M**. Then the resulting magnetic flux is:

$$\boldsymbol{B} = \mu_0(\boldsymbol{H_0} + \boldsymbol{M}) \qquad (3.3)$$

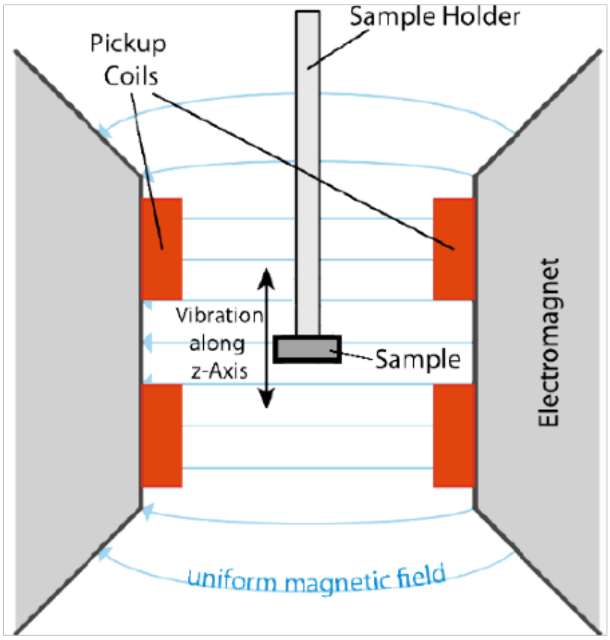

Figure 3.11: Schematic of the VSM principle.

Since **H₀** is uniform:

$$\frac{\partial \boldsymbol{B}}{\partial t} = \mu_0 \frac{\partial \boldsymbol{M}}{\partial t} \qquad (3.4)$$

and then:

$$\nabla \times \boldsymbol{E} = -\mu_0 \frac{\partial \boldsymbol{M}}{\partial t} \qquad (3.5)$$

This implies that also the electromotive force induced in the coils is proportional to the magnetization of the sample and depends on its orientation with respect to the coils

$$e.m.f = \oint \boldsymbol{E} dl = -\mu_0 \iint \frac{\partial \boldsymbol{M}}{\partial t} dS \qquad (3.6)$$

A pair of coils is used to minimize the noise caused by the external sources of magnetic field: the variations of the external field add to the signal of one coil and subtract from the signal of the other one. A transimpedance and a lock-in amplifier are used for the amplification of the induction current.

In this work, the commercial Microsense EZ9 (Figure 3.12) is used. Its fully automated controlling software allows to sweep the magnetic field from -2.25 T to +2.25 T, acquiring the M vs H plot. This system is able to measure magnetic moments down to 1 emu, hysteresis loop of thin films and it can be used to study magnetic properties of liquids, powders or bulk samples. Furthermore, it is possible to make magnetic measurement as function of temperature (from 100 K up to 1000 K), current and voltage. The maximum sample dimensions allowed are 10x10 mm^2 for room temperature measurements and 5x5 mm^2 using temperature control. Automated rotation of the sample is provided for polar characterization.

Figure 3.12: Commercial Microsense EZ9 VSM.

3.6 Electrical transport measurements

Electrical measurements are performed to study the I-V characteristic and the magnetoresistive properties of the sensors. In a two-point probe measurement (Figure 3.13(a)), one contact injects the current into the device under test (DUT), while the other measures the resulting tension in order to obtain R_{DUT}. What we actually measure is the total resistance R_T:

$$R_T = \frac{V}{I} = 2R_W + 2R_C + R_{DUT} \qquad (3.7)$$

where R_W is the resistance of the wires and R_C is the resistance of the contacts. Therefore, the result is accurate only if $R_{DUT} \gg R_W + R_C$. In the case of tunneling junctions, the tunneling resistance is usually high enough to satisfy such condition.

If this is not the case, the problem of parasitic resistance can be tackled using four-point probe measurements (Figure 3.13 (b)). In this case, the voltage is measured by the second set of probes on a parallel circuit. The very high input impedance of the voltmeter ($\sim 10^{12}\Omega$) guarantees a negligible voltage drop on wire and contact resistances, resulting in a more accurate measure of R_{DUT}.

The setup for TMR measurements is shown in Figure 3.13 (c). The sample is placed in an electromagnet, which generate the magnetic field. The current in the electromagnet is supplied by a KEPCO bipolar generator. A Keithley 2601 source meter provides both the probing current and the voltage detection for the magnetoresistive measurements. The data are collected by a Labview software that control all the instruments.

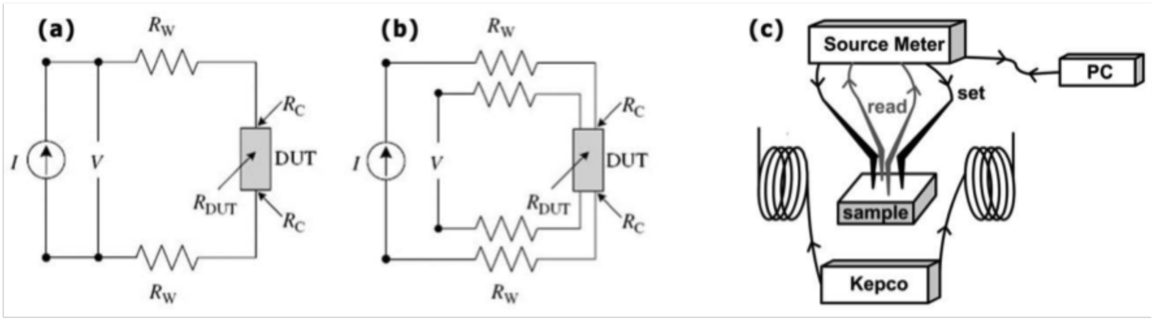

Figure 3.13: *Two-points probe (a) and four-point probe resistivity measurements (b). (c) Sketch of a four-point system for TMR measurements.*

An alternative setup, based on the use of a customized lock-in amplifier was developed for the acquisition of the low signals expected from the biological experiments. This setup is indeed optimized for going beyond commercial amplifiers in terms of signal-to-noise ratio. A more detailed description of the setup will be provided in Chapter 4.

Chapter 4: Towards low-field sensitive sensors for neuronal signal detection

In the framework of the project UMANA, highly sensitive sensors are developed in order to detect the small magnetic signals generated by the propagation of action potentials along the neuronal axon. These signals present an amplitude that ranges from 1 nT to 10 nT and a duration of few ms [22] as shown in Figure 4.1. For this reason, to follow the signal propagation, the requirements in terms of bandwidth are BW~1 kHz, while the sampling frequency must be of the order of tens of kHz. Before performing the *in-vitro* experiments with brain slices, preliminary studies have to be done in order to optimize the sensors, the electronics and the biology.

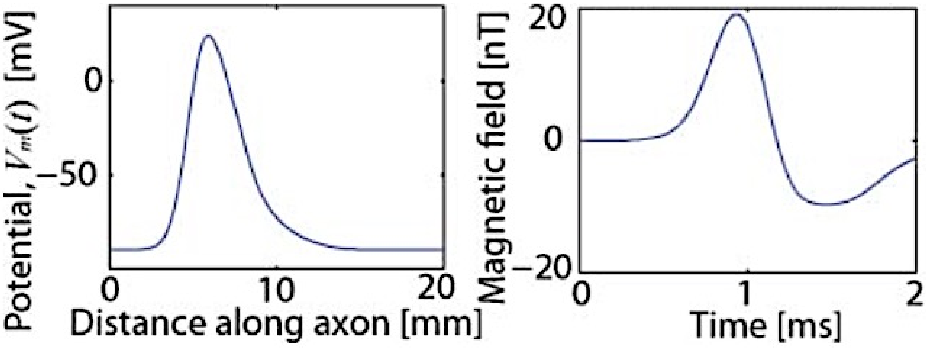

Figure 4.1: *(left) Transmembrane potential distribution along the axon. (right) Time-dependent magnetic field produced by the propagation of the action potential along the axon. From* [22].

The aim of these measurements was the analysis of the sensors' performances in terms of noise and minimum detectable signal, in order to find the optimum sensor to perform the detection experiments. In this thesis work, four different sensor architectures were investigated.

In the first part of this chapter, the four architectures are presented. In the second part, the electronic setup is described. Finally, the results of the performance analysis are reported.

4.1 Sensor architecture and characterization

The four different layouts were labelled as: MTJ-LOCSENS, MTJ-SPINBIOMED, MTJ-AlOx and GMR-SV. The former two were grown at PoliFAB during previous works, while the latter ones were provided by the INESC laboratory in Braga. Each of them represented a different working principle or a different technological implementation. Therefore, we will expect very different behavior both in terms of MR features and of noise. The MTJ-based devices will present the best MR properties; in turn, the GMR-based sensor will show the lowest noise figure, since the tunneling barrier intrinsically introduces additional noise.

4.1.1 Sensor layouts

In the following, the features and the main differences between them will be explained:

-MTJ-LOCSENS: magnetic tunneling junction based on a MgO barrier. Each 10x10-mm^2 chip contains an array of 12 MTJs (Figure 4.2) with active area of 30x40 μm^2. The whole stack is reported hereafter (thickness in nm): Ta (5)/ Ru (18)/ Ta (3)/ $Ir_{0.2}Mn_{0.8}$ (20)/ $Co_{0.6}Fe_{0.4}$ (1.8)/ Ru (0.9)/ $Co_{0.4}Fe_{0.4}B_{0.2}$ (2.7)/ MgO (1.26)/ $Co_{0.4}Fe_{0.4}B_{0.2}$ (1.25)/ Ru (5)/ Ta (20). The MgO insulating layer was 1.26 nm thick, while the reference and free $Co_{0.4}Fe_{0.4}B_{0.2}$ layers 2.7 nm and 1.25 nm respectively. As explained in Paragraph 2.3, the reference layer was pinned by means of a synthetic antiferromagnet (SAF) structure composed by an $Ir_{0.2}Mn_{0.8}$ AFM layer exchange biased to a $Co_{0.6}Fe_{0.4}$ layer, which in turn was antiferromagnetically coupled to the reference $Co_{0.4}Fe_{0.4}B_{0.2}$ layer via bilinear coupling. The free $Co_{0.4}Fe_{0.4}B_{0.2}$ layer was thin enough to be superparamagnetic. This means that the magnetic response shows a remarkable linearity as illustrated by the R vs H characteristic in Figure 4.8(a). Moreover, a good value of TMR ratio is achieved thanks to the spin-filtering effect of the crystalline barrier. This value is quite far from the three-digit figures of the state-of-art MTJs employed as memories [17], because TMR has been traded for the linearity. However, the most important figure of merit for a sensor is the sensitivity S_{sens}, which measures how much the resistance changes upon a variation of the applied magnetic field. It is defined as:

$$S_{sens} = \frac{dR}{R_0}\frac{1}{dH} \tag{4.1}$$

where R_0 is the resistance at zero external field and dR is the sensor resistance change for an external field variation dH. The sensitivity is usually expressed in %/mT. This kind of sensor can attain values of the order of 10%/mT.

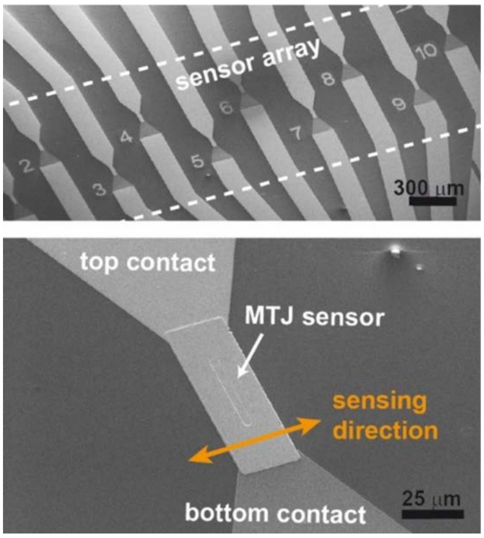

Figure 4.2: *SEM images of the MTJ-LOCSENS. (top) Sensor array and (bottom) particular of the junction. From [43].*

-MTJ-SPINBIOMED: also a MgO-based sensor. It is grown on a 5x5-mm^2 chip and presents an 8-junction array (Figure 4.3). The structure is very similar to the MTJ-LOCSENS, having the same SAF. The big difference with respect to the MTJ-LOCSENS was that the MgO thickness was 2 nm and that the free $Co_{0.4}Fe_{0.4}B_{0.2}$ layer was 1.4 nm thick, enough to overcome the superparamagnetic limit and due to the micron sized dimension of the junction (2,5x120 μm^2), magnetic domains were formed. In this case, the magnetization reversal occurs by domain wall motion instead of coherent rotation. As a consequence, its magnetic response is more hysteretic but in turn the TMR ratio and the sensitivity are much higher, the latter reaching values as high as 32%/mT (Figure 1.7(b)).

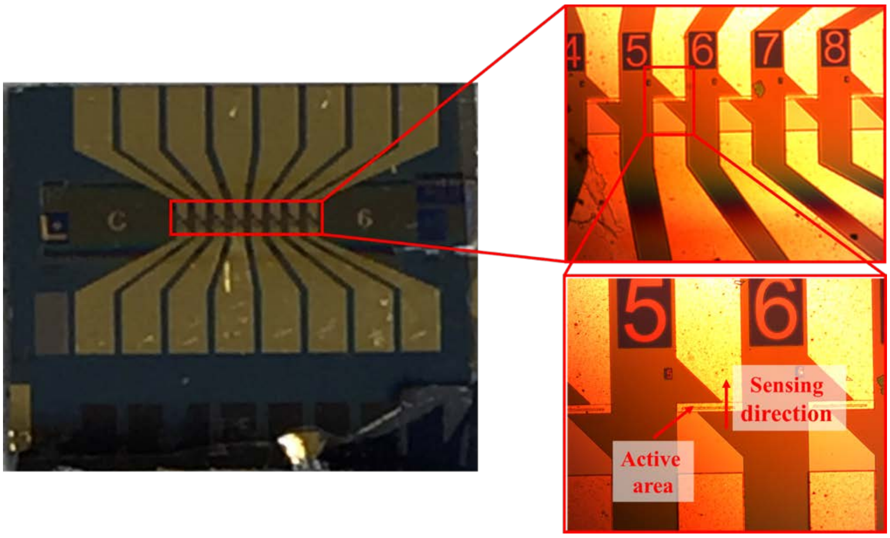

Figure 4.3: *Optical images of the MTJ-SPINBIOMED. The insets show the array and the particular of a single junction.*

-MTJ-AlOx: a TMR-based device with the same properties and geometry as MTJ-LOCSENS (Figure 4.4), but with the fundamental difference of an amorphous aluminum oxide (AlOx) barrier. The stack consisted in (thickness in nm): [Ta (5)/ Ru (15)]x4/ NiFe (6)/ $Co_{0.4}Fe_{0.4}B_{0.2}$ (3)/ AlOx (1.8)/ $Co_{0.4}Fe_{0.4}B_{0.2}$ (4)/ Ru (0.6)/ $Co_{0.6}Fe_{0.4}$ (3)/ $Ir_{0.2}Mn_{0.8}$ (18)/ Ru (15). The junction had a 1.8-nm-thick tunneling barrier and relatively thick $Co_{0.4}Fe_{0.4}B_{0.2}$ reference and sensing layers, 3-nm-thick and 4-nm-thick respectively. However, due to the lack of coherent spin filtering, it follows that the TMR ratio is much smaller and so is the sensitivity (see Section 2.1.4). The presence of a soft pinning of the free layer, by means of the NiFe layer, can affect the dynamic range of the sensor.

-GMR-SV: a GMR-based sensor in the spin valve (SV) CIP configuretion (Figure 4.5). The whole stack was (thickness in nm): Si/ Al_2O_3 / Ta (1.5)/ NiFe (4.5)/ CoFe (0.5)/ Cu (1.9)/ CoFe (2.5)/ $Ir_{0.2}Mn_{0.8}$ (7)/ Ta (2) / $TiWN_2$ (15). Here the thicknesses were 1.9 nm for the Cu spacer, 2.5 nm for the reference layer and 0.5 nm for the free layers. Since it exploited a different physical effect (see Paragraph 2.2), the MR ratio and the sensitivity are inherently smaller. Such a thin sensing layer points towards a superparamagnetic response.

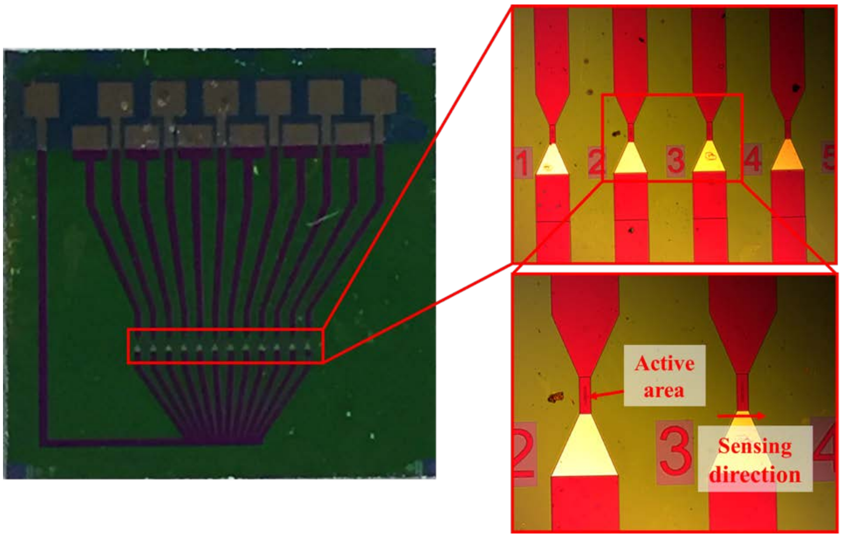

Figure 4.4: *Optical images of the MTJ-AlOx. The insets show the array and the particular of a single junction.*

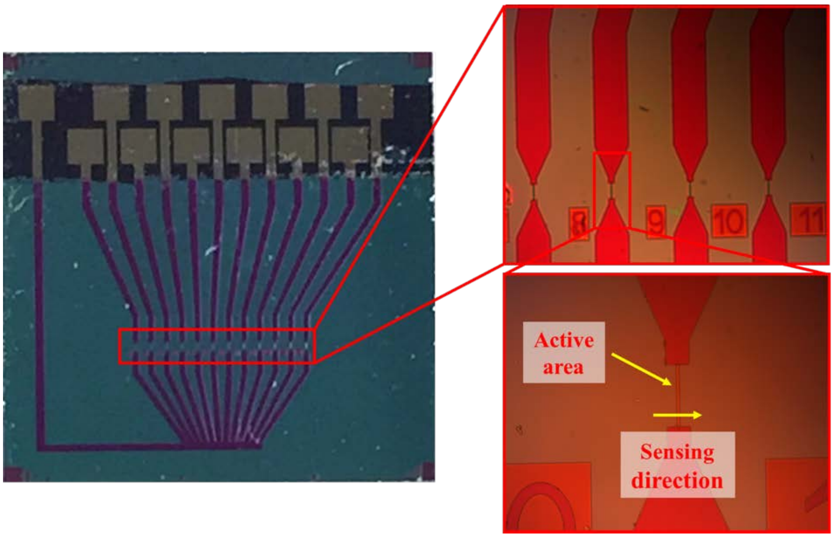

Figure 4.5: *Optical images of the GMR-SV. The insets show the array and the particular of a single junction.*

4.1.2 Preliminary characterization

Before the noise analyses, the sensors were preliminary characterized in terms of magnetoresistance, sensitivity, dynamic range and coercive field. The measurements were performed applying a 50-mV bias modulated at 40 kHz across the sensors, except for the GMR recorded at 100 mV, in a static magnetic field.

In Figure 4.6 the sensors' transfer curves are reported. As expected, the MTJ-LOCSENS and the MTJ-SPINBIOMED exhibit a different behavior. First of all, the difference in MgO barrier thicknesses accounts for the large difference in the resistances, respectively 266 Ω and 5710 Ω. Both values are in good accordance with the behavior of the tunneling current, which is exponential with the height of the potential barrier and linear with the area of the junction [47]. Besides, the thicker $Co_{0.4}Fe_{0.4}B_{0.2}$ layer in the MTJ-SPINBIOMED results in the highest TMR ratio of 62.5%, while the MTJ-LOCSENS presents just a 27% of TMR. In turn the MTJ-LOCSENS achieves a very good linear response with a coercivity of less than 1 mT (=10 Oe); actually, this value is the coercive field of the electromagnet. Since their dynamic ranges (i.e. the field regions where the response is linear) are comparable (~1 mT) because of the same SAF, the sensitivity of the MTJ-SPINBIOMED is much higher as well.

The MTJ-AlOx has a resistance of only 128 Ω. It presents low MR ratio of 11.5%, as predicted, and an even worse sensitivity (1.74%/mT), the dynamic range being quite large (~4 mT). These features can be accounted for by the amorphous tunneling barrier and the soft pinning.

The GMR-SV has very poor MR properties, featuring values more than one order of magnitude below those of the other sensors: 1.74% of TMR ratio and 0.2%/mT of sensitivity. In turn, the coercivity is quite good, being comparable to the MTJ-LOCSENS.

Table 4.1 sums up the main features of the four devices. Figure 4.7 illustrates the comparison between the for characteristics.

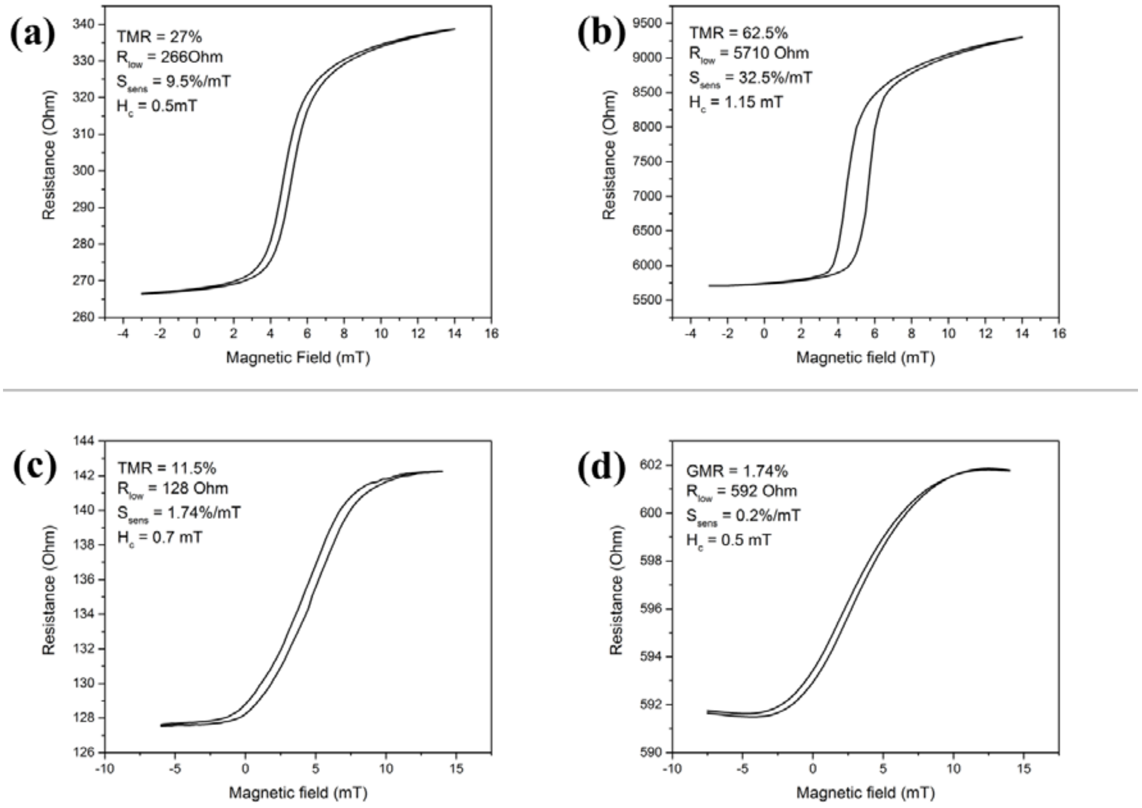

Figure 4.6: *R vs H characteristics of (a) MTJ-LOCSENS, (b) MTJ-SPINBIOMED, (c) MTJ-AlOx, (d) GMR-SV sensors, measured at 50 mV (100 mV for the GMR-SV).*

Table 4.1: *Main features of the sensors under investigation.*

	MTJ-LOCSENS	***MTJ-SPINBIOMED***	***MTJ-AlOx***	***GMR-SV***
TMR/GMR ratio (%)	*27*	*62.5*	*11.5*	*1.74*
Lowest resistance (Ω)	*266*	*5710*	*128*	*592*
Sensitivity (%/mT)	*9.5*	*32.5*	*1.74*	*0.2*
Dynamic range (mT)	*1.16*	*1*	*4.1*	*3.2*
Coercivity (mT)	*0.5*	*1.15*	*0.7*	*0.5*

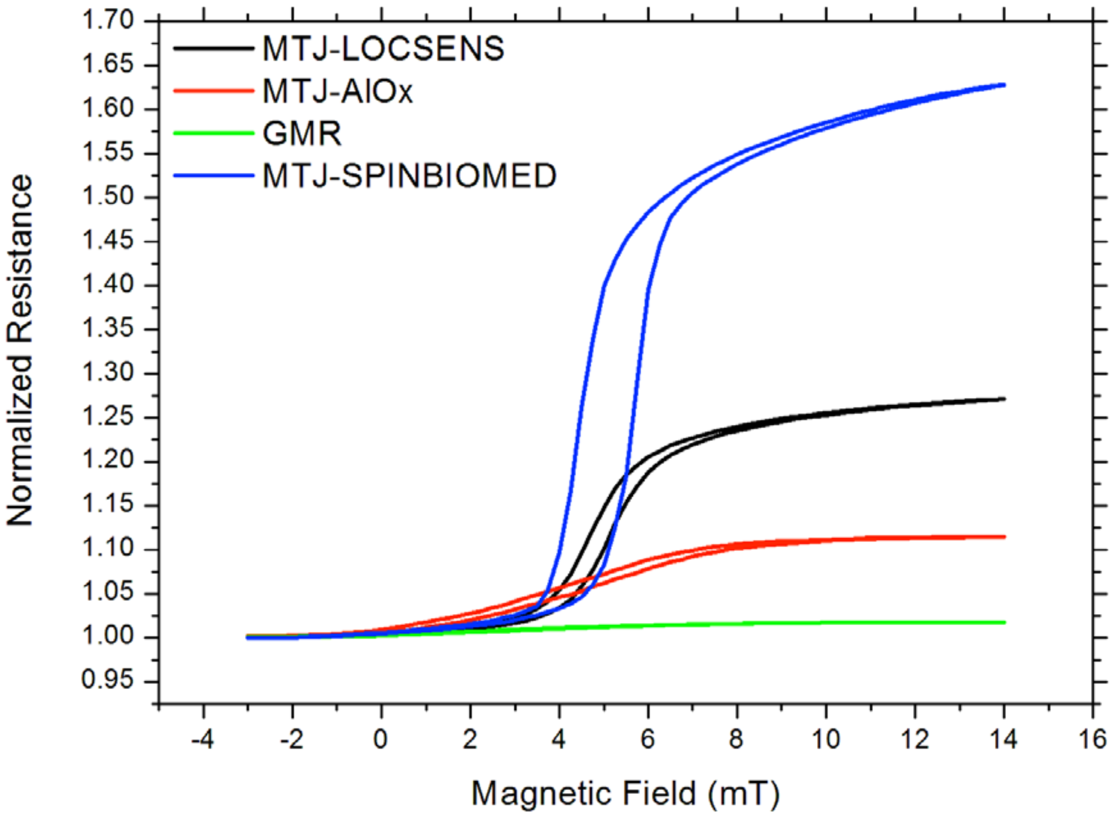

Figure 4.7*: Comparison of the four characteristics.*

As seen, the MTJs exploiting a crystalline barrier have by far the best MR properties.

Nevertheless, an exhaustive noise analysis is still necessary since the sensors may perform differently in terms of noise and hence minimum detectable field.

4.2 Noise analysis

Noise is a fundamental and unavoidable phenomenon in physics and electronics. Noise corresponds to random fluctuations of a macroscopic quantity (such as the output voltage of a sensor) around its mean value and it is present in all electronic devices (either active or passive components). Such fluctuations can be evaluated and characterized to quantify the Signal-to-Noise Ratio (SNR) of a device. To measure a magnetic signal of interest, its amplitude must be substantially higher than the device's noise level (SNR > 1). The noise of a MR sensor comes mainly from magnetic fluctuations associated to magnetic domain nucleation and displacement within the sensing layer, but also the electronic noise plays a relevant role.

In this paragraph, first, the main noise terms will be reviewed and then the noise signatures of the sensors will be analyzed.

4.2.1 Noise sources

Magnetoresistive sensors present several types of noise:

-**Thermal noise:** Two components can be distinguished: electronic and magnetic. Thermal electronic noise, also called Johnson-Nyquist noise [81], arises from the random thermal motion of electrons inside electronic devices, regardless of the applied voltage or current. Johnson noise is a white noise, which means it is frequency-independent. The voltage noise Power Spectral Density (PSD, $\left[\frac{V^2}{Hz}\right]$) of a resistance R ([Ω]) at temperature T ([K]) is given by:

$$S_V = 4k_B TR \tag{4.2}$$

where k_B is the Boltzmann's constant. As the dimensions of a MR sensor are decreased, random fluctuations of the sensing layer magnetization occur under thermal excitation, becoming comparable with the thermal electronic noise. These thermally activated fluctuations are the source of thermal magnetic noise, which is frequency independent and inversely proportional to the sensing layer volume [82]–[84].

-**Flicker (or $1/f$) noise:** The flicker noise is a pervasive phenomenon observed in a large variety of systems, from geology to biology. It follows a $1/f$ power law, which means that it is dominant at low frequencies. The electronic $1/f$ noise arises from voltage fluctuations related to charge trapping in crystal defects. The PSD of $1/f$ noise can be empirically expressed as [85]:

$$S_{1/f}(f) = \gamma_H \frac{V^2}{NAf} \tag{4.3}$$

where γ_H is the Hooge constant, which depends on the material, and N is the total number of charge carriers and A is the area of the pilar. The noise in a GMR device is the electronic one commonly found in any metallic wire of the same size but in TMR sensor it is much higher. This is mainly due to inverse dependence on the number of carriers. In fact, the tunnel barrier, combined with the spin-filtering effect and the small section of the pillar, considerably reduces the number of carriers involved in the process. As consequence, consistent contribution of $1/f$ noise is expected for MTJs in the following analysis. Moreover, a magnetic component of the flicker noise can be identified. The oscillations in the sensing layer magnetization caused by domain wall pinning and depinning at defect sites are behind the origin of the magnetic flicker noise [86]. Therefore, the maximum density of $1/f$ magnetic noise occurs in the linear transition of the sensor, where the magnetization of the sensing layer is switching between the two saturation states. The $1/f$ magnetic noise is dominant in the sensor linear range and is mostly suppressed in the saturation states [86].

-**Random Telegraphic Noise (RTN):** Random Telegraphic Noise corresponds to fluctuations between two or several discrete levels with comparable energies, due to the presence of defects in the conductor. This is usually the main source of noise in semi-conductors. The random magnetization fluctuations in the sensing layer are the origin of RTN (or Barkhausen effect) in MR sensors, which exhibits a Lorentzian type frequency behavior. The fluctuations can have either electrical or magnetic origin. The former are caused by a repeated capture of electrons into trapping centers (spin-independent) [87], the latter by the displacement of domain walls (spin-dependent) [82], [88] RTN is not always evident, being shadowed in the low-frequency band by the $1/f$ magnetic noise.

4.2.2 Noise measurements

The field noise spectral density was measured with a Cross-correlation Spectrum Analyzer (CSA) setup and the integrated spectrum was calculated [89]. Since the typical duration of the neural action potential is in the millisecond length, a kHz range was mainly taken into consideration.

A voltage of 100 mV (50 mV for the MTJ-AlOx) was applied to the devices under test (DUTs). An external magnetic field generated by an electromagnet was used to bias the sensors in different points of their R vs H transfer curve. The measurement scheme is represented in Figure 4.8. The cross-correlation is a technique that allows to go well below the measuring possibility of a conventional spectrum analyzer. In order to achieve that, the signal to be measured from the DUT (in this case the noise power spectral density) is therefore processed in phase by two parallel channels. The outputs of the channels are therefore multiplied frequency by frequency to give at the output of the multiplier a signal with mean value proportional to the DUT input signal at the selected frequency. The frequency components of the noises of the two input amplifiers, instead, are uncorrelated to each other (out of phase) and, after having followed the same path as the DUT signal, give a signal at the output of the multiplier with zero mean value and standard deviation equal to the input amplifier noise power density at the selected frequency. The final averaging will reduce these fluctuations to any low value by properly extending the measuring time and allow to evaluate the DUT signal with increasingly high precision.

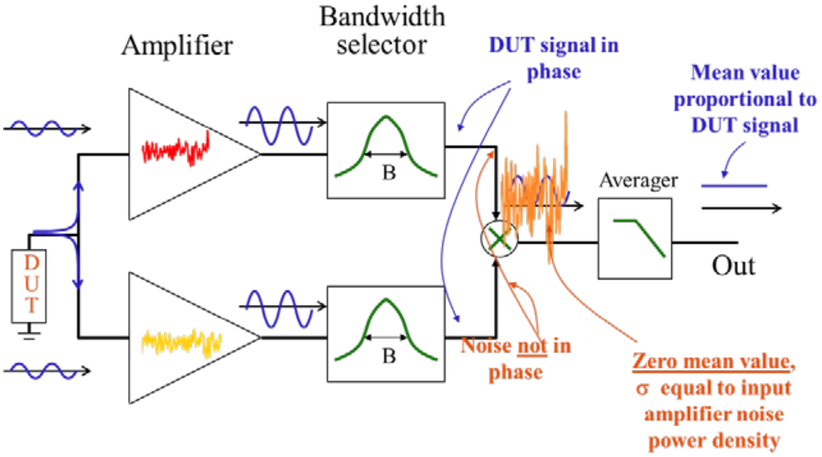

Figure 4.8: *Electronical scheme of the noise measurement [90]. The two parallel channels consist of an amplifier and a bandwidth selector to perform the frequency-by-frequency multiplication. A low-pass filter follows the multiplier and carry out the averaging of the amplifiers' noise.*

The voltage resolution achievable from an arbitrary measurement with the sensor can be obtained by integrating the noise spectrum in the range of the magnetic frequency of interest. The conversion in terms of minimum detectable magnetic field was performed calculating the value of the sensitivity in the considered working points, i.e. in the different points of the transfer curve, by means of Eq. 4.4, and assuming to apply a fixed current as in the real measurements.

$$\delta H_{min} = \frac{\delta R_{min}}{R_0}\frac{1}{S_{sens}} = \frac{\delta V_{min}}{V_0}\frac{1}{S_{sens}} \tag{4.4}$$

where V_0 is the applied voltage and δV_{min} is the voltage resolution.

4.2.3 Results and discussion

In this section, the noise figures of each sensor are reported.

Figure 4.9 refers to the MTJ-LOCSENS. As expected, the most sensitive point of the *R(H)* curve (blue line in Figure 4.9(a)) exhibits the highest voltage noise level due to the magnetic noise. At 1 kHz the noise figure is still dominated by the $1/f$ noise. In fact, the thermal noise is about 2 $\mathrm{nV}/\sqrt{\mathrm{Hz}}$ and the corner frequency is about one decade above. Calculating the modified Hooge constant $\alpha_H=\gamma_H/N$ from the experimental data, one finds $\alpha_H=7.68\cdot10^{-8}$ $\mu\mathrm{m}^2$, a value in accordance with the literature [91]. Nevertheless, when the noise figure is converted in minimum detectable field (Eq. 4.4), the weight of the sensitivity changed the situation substantially (Figure 4.9(c-d)). Thus, a noise spectral density of about 5 nT/√Hz is found for a 5-mT magnetic bias, compared to about 20 nT/√Hz for a 1.5-mT bias. An integrated value of about 250 nT was calculated in a 1 Hz-1 kHz bandwidth (Figure 4.9(d)). The reported values are comparable with or lower than the resolutions found in previous works [92], [93].

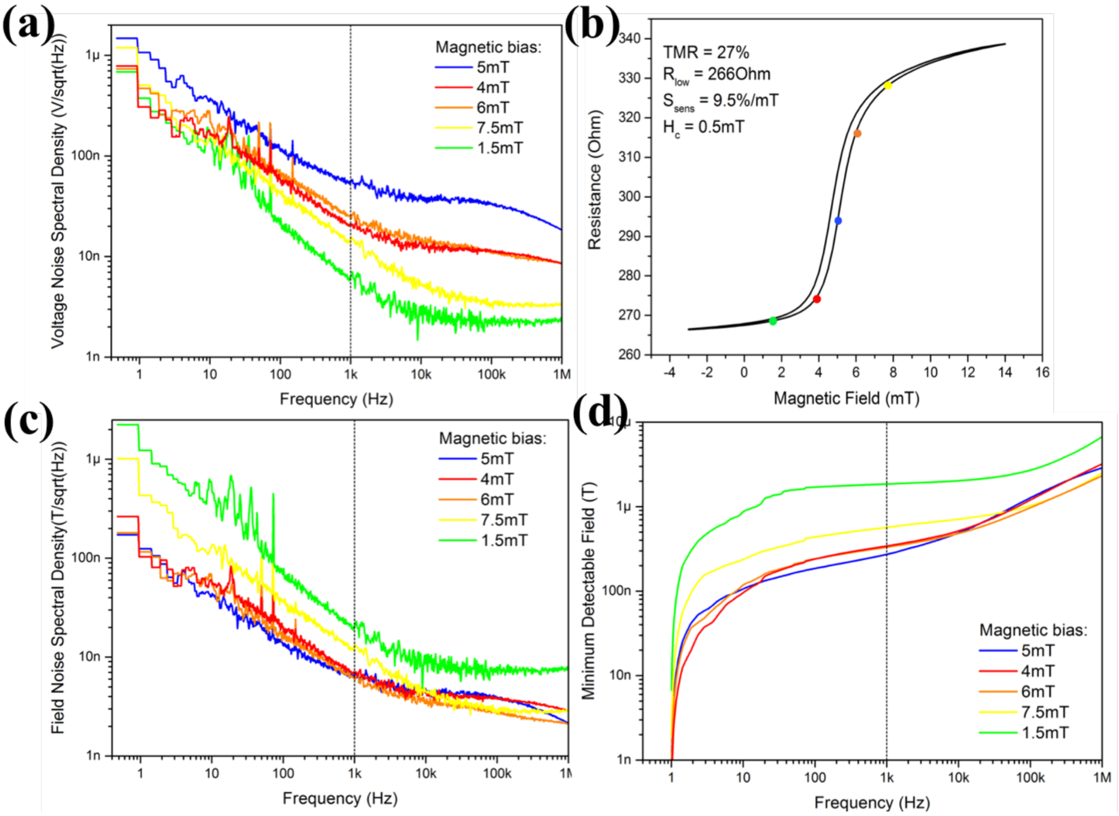

Figure 4.9: *Noise figure of the MTJ-LOCSENS. (a) Noise spectral density recorded at different magnetic bias, (b) corresponding to different points on the R(H) curve. (c) Conversion of the voltage noise in magnetic units by means of the sensitivity giving the resolution in 1Hz-bandwith. (d) Integrated spectrum giving the resolution for broad band measurements.*

A similar situation was found for the MTJ-SPINBIOMED. However, due to the thicker free layer, the switching dynamics is different, involving wall domain motion. This causes a higher $1/f$ respect with the LOCSENS case. The thermal noise is greater as well, since the sensor's resistance is much higher, giving a value of about 10 $\mathrm{nV}/\sqrt{\mathrm{Hz}}$. Then, in the saturated regions, where flicker noise is lower, the corner frequency is 1 kHz, while in the linear regions, where $1/f$ is much relevant, the corner goes beyond 100 kHz (Figure 4.10(a)). Even though the noise figure is the worst, as for the MTJ-LOCSENS, the sensitivity of the linear region reverts the situation, leading to a noise spectral density of 7 $\mathrm{nT}/\sqrt{\mathrm{Hz}}$ and an integrated value of about 430 nT (Figure 4.10(c,d)).

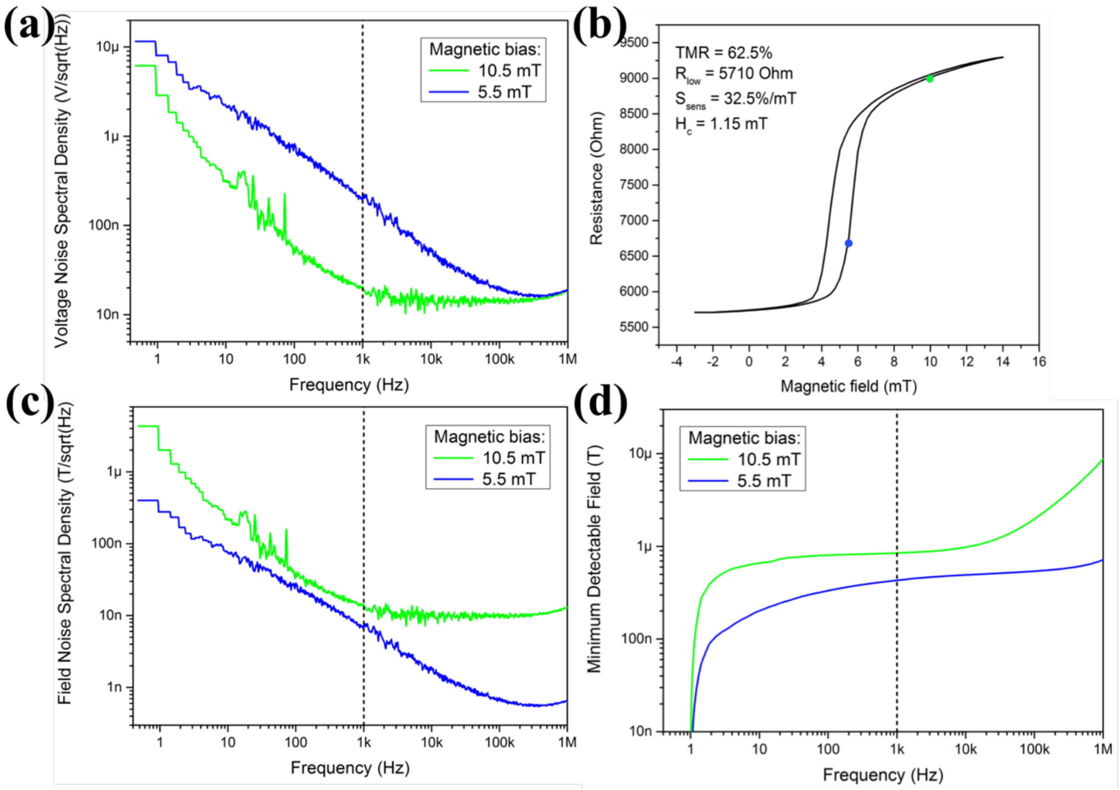

Figure 4.10: *Noise figure of the MTJ-SPINBIOMED. (a) Noise spectral density recorded at different magnetic bias, (b) corresponding to different points on the R(H) curve. (c) Conversion of the voltage noise in magnetic units by means of the sensitivity giving the resolution in 1Hz-bandwith. (d) Integrated spectrum giving the resolution for broadband measurements.*

Regarding the MTJ-AlOx, the noise signature was dominated by low frequency noise similarly to the previous devices and the noise level was comparable as well. Actually, in this case there is a strong contribution from RTN, which goes ~f^{-2}. This is why the corner frequency is shifted at higher frequency (~100 kHz). However, due to the poorer sensitivity, the field noise was quite higher ($76\ \mathrm{nT}/\sqrt{\mathrm{Hz}}$), resulting in an integrated noise of 6 μT (Figure 4.11(d)).

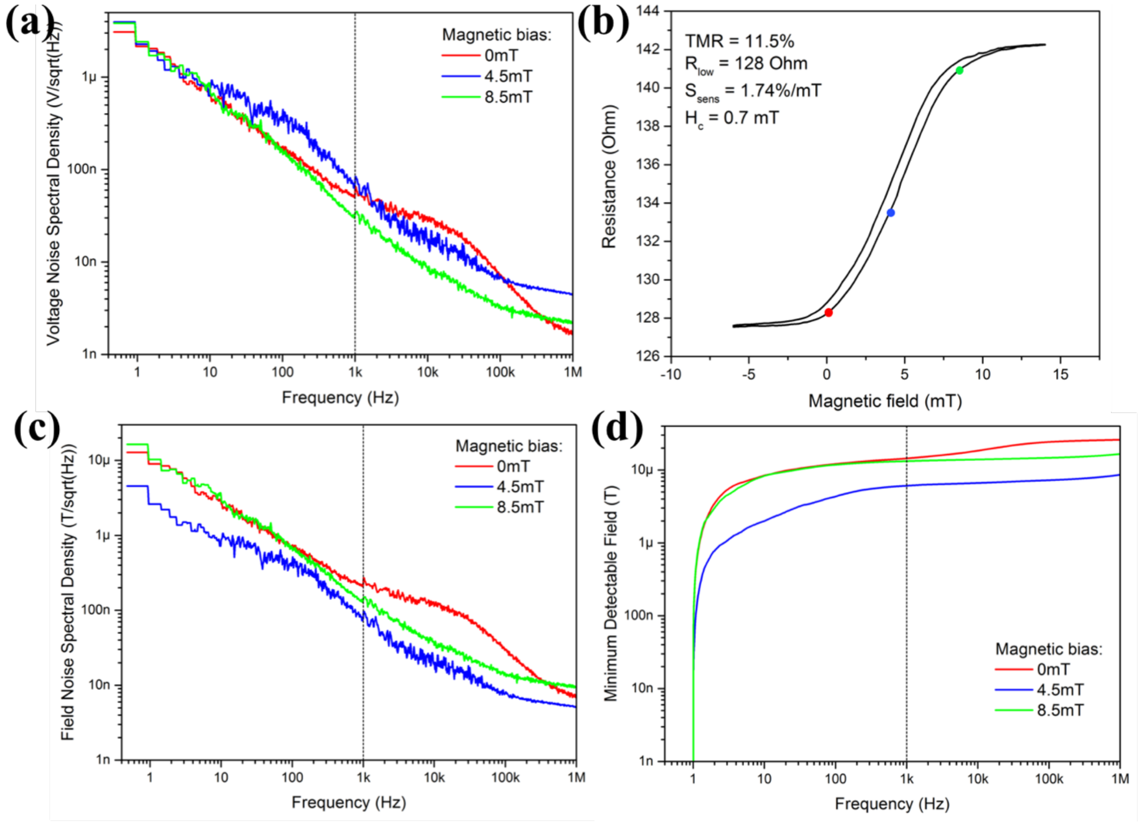

Figure 4.11: *Noise figure of the MTJ-AlOx. (a) Noise spectral density recorded at different magnetic bias, (b) corresponding to different points on the R(H) curve. (c) Conversion of the voltage noise in magnetic units by means of the sensitivity giving the resolution in 1Hz-bandwith. (d) Integrated spectrum giving the resolution for broad band measurements.*

Finally, the GMR-SV presented a remarkably low $1/f$ noise. Such difference could be accounted for by the low electric noise related to the absence of the tunneling barrier. This, combined with an intermediate resistivity, gives a corner frequency of only 300 Hz. Nevertheless, the very modest sensitivity made the field noise spectral density hardly comparable to that of the MgO-based MTJs. Then a Limit Of Detection (LOD) of about 1.15 µT was obtained (Figure 4.12(d)).

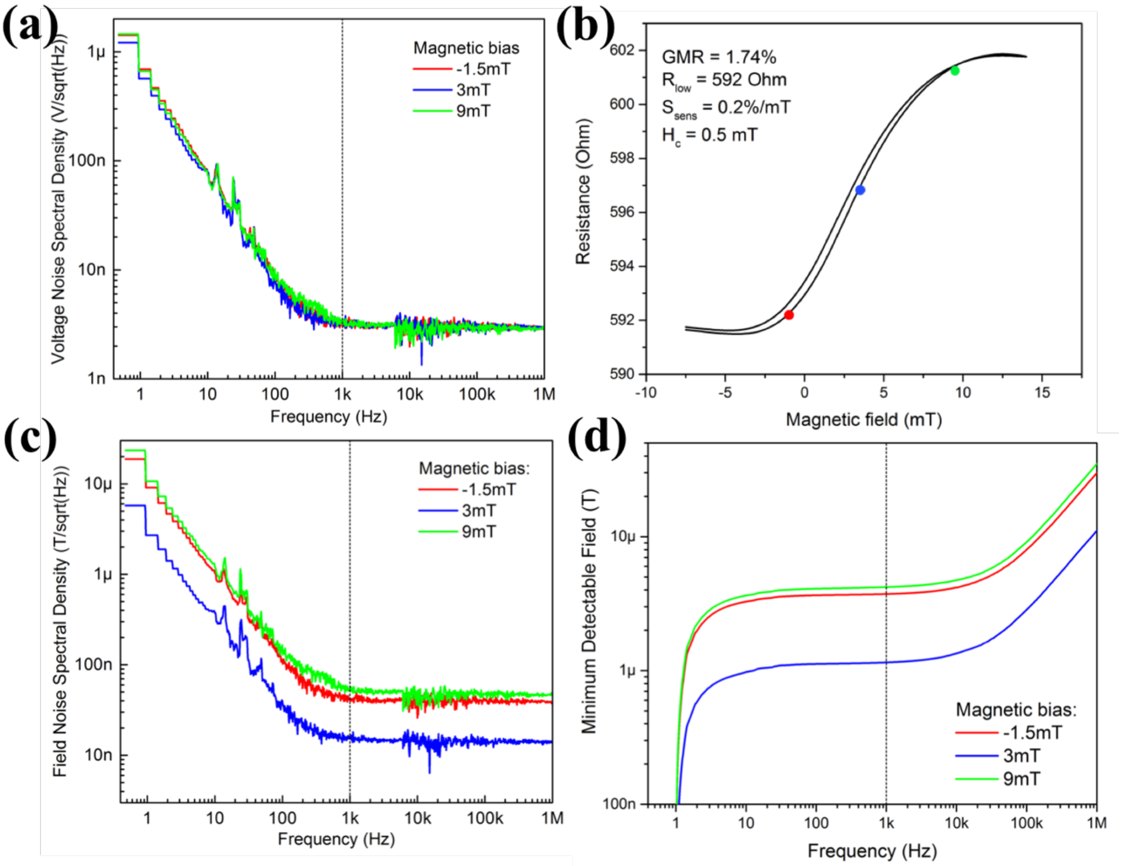

Figure 4.12: *Noise figure of the GMR-SV. (a) Noise spectral density recorded at different magnetic bias, (b) corresponding to different points on the R(H) curve. (c) Conversion of the voltage noise in magnetic units by means of the sensitivity giving the resolution in 1Hz-bandwith. (d) Integrated spectrum giving the resolution for broad band measurements.*

4.2.4 Conclusions

It is worth noting that in all MTJ-based sensors under investigation, the spectra were largely dominated by the $1/f$ noise, at least in the bandwidth of interest. One should therefore concludes that the resistance of the sensor and the white noise do not affect at all the resolution. On the contrary, the $1/f$ noise contains a contribute which is proportional to the resistance. Furthermore, extending the integration at higher frequency, the contribution of white thermal noise becomes predominant. Thus, in the design stage of a sensor, one should consider the tradeoff between good MR properties (high resistance) and low noise figures (low resistance). The GMR-SV showed a very low flicker noise contribution. However, such difference could not compensate for the large difference in sensitivities. Regarding the MTJ-AlOx, the RTN was found to be the dominating term. This can be due to the combination of an amorphous tunneling barrier and thick magnetic electrodes, which increases the occurrence of noise-related phenomena.

Finally, it is worth remarking that above 1 MHz, the spectra become strongly affected by the noise from the analyzer.

Figure 4.13 shows the comparison between the minimum detectable field of the four sensors.

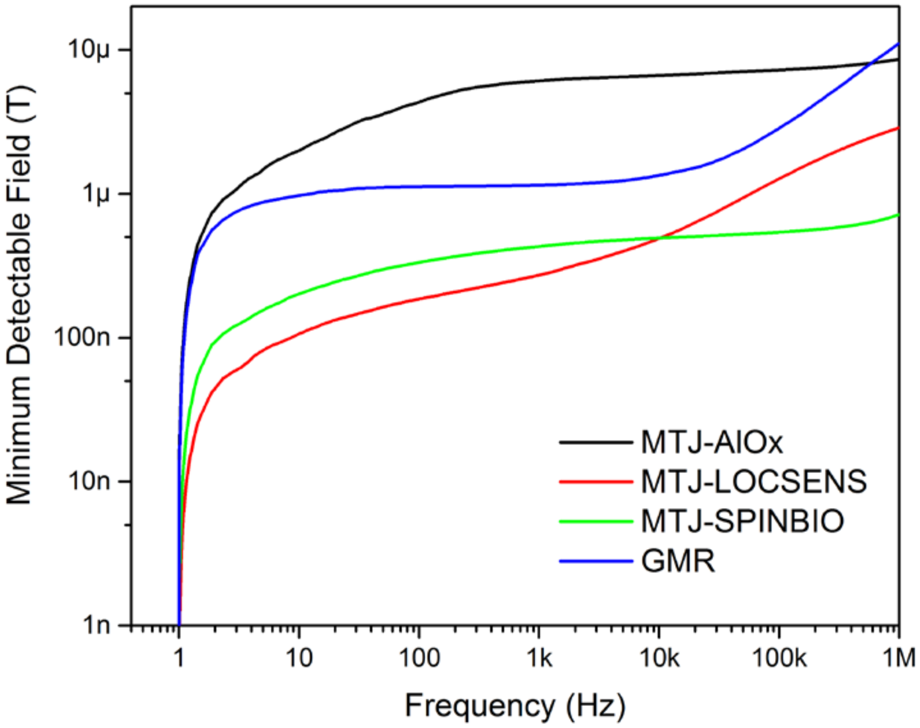

Figure 4.13: *Comparison between the minimum detectable fields of the four sensors.*

As a matter of fact, since the typical magnetic field, expected to be generated from a single neuron firing, ranges from 2 nT to 10 nT, only a narrow-band measurement would result in a successful detection. The latter configuration would also require a modulation of the magnetic field, and such feature is still under development [20], [94]. On the other hand, a broad-band measurement configuration could be well utilized when an assembly of neurons are analyzed. The latter condition is verified when brain slices are considered, where several hundreds of cells potentially fire synchronously, resulting in much higher currents, and thus, magnetic field.

To sum up, the MgO-based MTJs turned out to be the most promising candidates in term of theoretical minimum detectable field (Table 4.2).

Table 4.2: *Comparison of the voltage and field NSD at 1 kHz and theoretical limits of detection (LODs) in 1Hz-1kHz broad band for the best operating point.*

	MTJ-LOCSENS	***MTJ-SPINBIOMED***	***MTJ-AlOx***	***GMR-SV***
Voltage NSD (nV/√Hz)	*54*	*202*	*62*	*3.2*
Field NSD (nT/√Hz)	*5*	*7*	*76*	*15*
Theoretical LOD (nT)	*250*	*430*	*6000*	*1150*

It is important to remark that the low noise figure of most of the sensors is lower or comparable to the noise levels of commercial electronics (noise > 5 $\mathrm{nT}/\sqrt{\mathrm{Hz}}$ at 10 kHz). As outlined in previous works [95], this is actually a strong limitation for the experiments. This is the reason why a customized dedicated electronic setup was developed with a noise of 3 $\mathrm{nT}/\sqrt{\mathrm{Hz}}$ at 1kHz (see Section 4.3.2).

4.3 Minimum detectable signal analysis

The noise analysis gives the theoretical limit of detection of the sensors under investigation. Then, to find out the actual resolution of the devices, we tried to simulate a bundle of neuronal axons by means of current lines fabricated on top of the sensors in which a current pulse propagated (Figure 4.14). The final sensitivity of the sensors was measured by using the platform described in Section 4.3.2 and a software (see Section 4.3.3) developed in order to perform automatic measurements of the limit of detection of the sensors in different conditions.

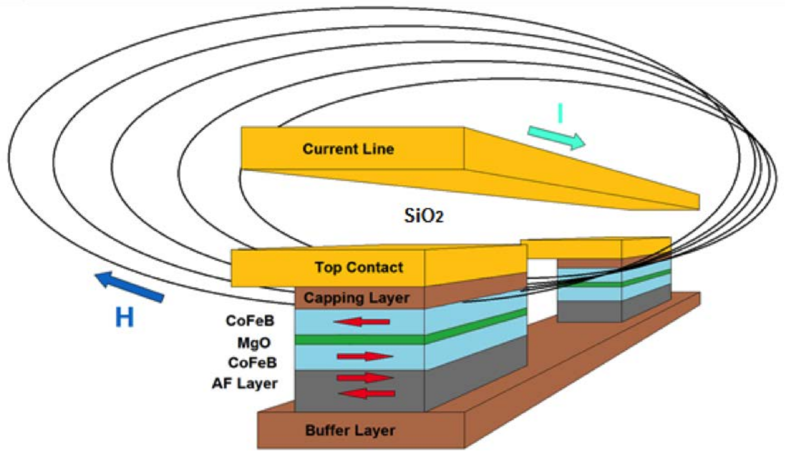

Figure 4.14: *3D representation of the field generated by a current line placed above the sensor.*

4.3.1 Current line fabrication

The realization of the current lines, fabricated on the top of the sensors, requires additional lithographic steps: a planarization process and the actual deposition of the line.

First of all, the sensors, due to the two etching steps (see Paragraph 5.2), present a quite uneven surface. In fact, between the junction and the surrounding SiO_2, there is a height difference of about 40 nm given by two consecutive etching (of 90 and 60 nm respectively) and a 110-nm SiO_2 deposition. Even though the oxide layer is quite uniform, the underlying steps could lead to short-circuits between the current line and the underlying electrodes. To solve the problem, a direct lithographic process with mask 3 (see Section 5.5.2) was performed to cover all the electric contacts with resist. Then a SiO_2 layer about 70 nm thick was deposited to make the surface more planar. Finally, to insulate the current line from the electric contacts of the chip, a 300 nm-thick SiO_2 capping layer was deposited. At this point, the surface was flat enough to proceed to the next phase.

The current line was realized with an image reversal lithographic process using mask 4 (Figure 4.15) to define the path. The line was made up of a Ti(7 nm)/Au(200 nm) bi-layer. The dimension of the linear path (10x230 μm^2) were chosen consistently with the dimension of the biological specimen. Indeed, an axon can have a diameter ranging from μm 1 to 25 μm and can reach length of several hundred of mm. With this geometry, the line can be approximated to an infinite wire with respect to the underlying sensor (3x40 μm^2).

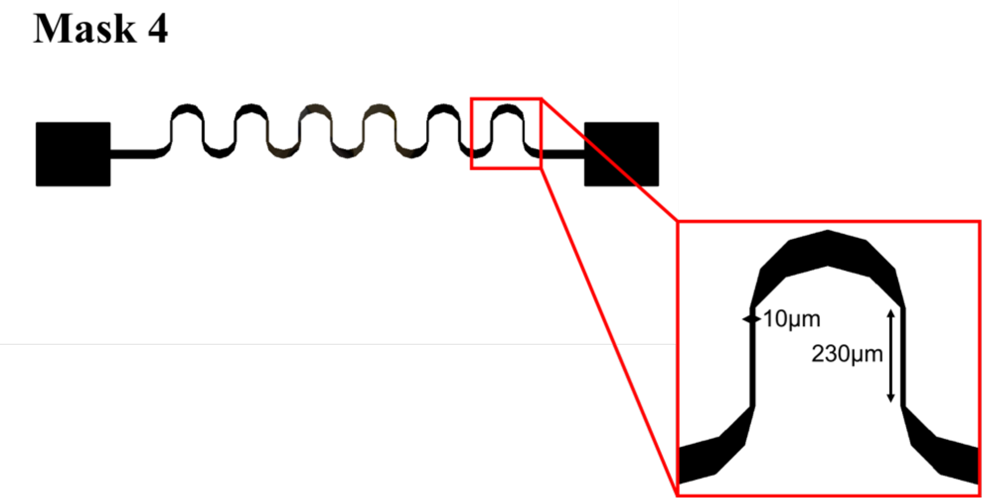

Figure 4.15: *Mask 4 for the realization of current lines.*

Since directionality is fundamental for the correct sensing, the vertical sides of the line were carefully aligned to the long side of the sensors (Figure 4.16(a)). It is worth noting that the different geometry of the MTJ-SPINBIOMED sensor required a different mask (Figure 4.16(b)). Such musk presented a double current line, because it was designed for different purposes. To perform the experiments in the same geometry with respect to the other sensor, only one of the two current lines, 5-μm wide, was aligned to the sensor.

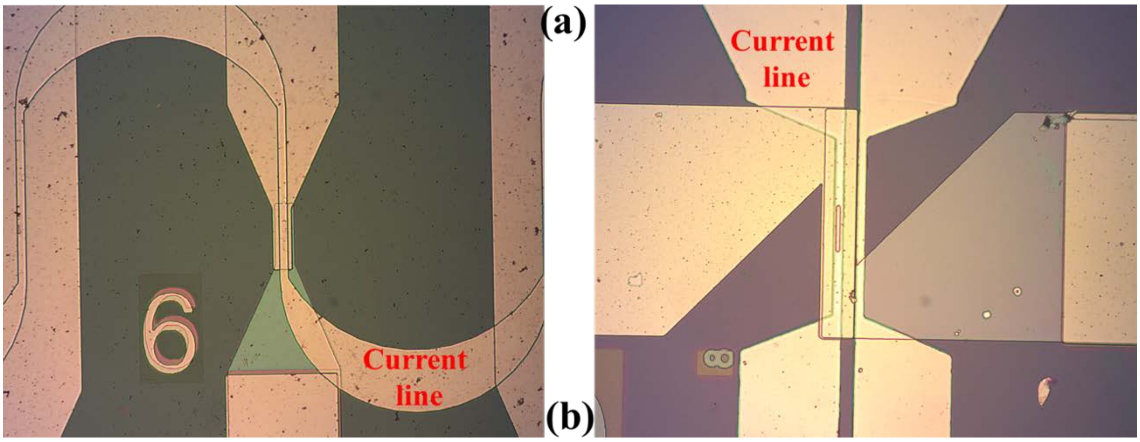

Figure 4.16: *Particular of the alignment of the current lines on (a) MTJ-LOCSENS and (b) MTJ-SPINBIOMED.*

4.3.2 Electronic platform

The characterization in term of noise, minimum detectable signal and the final experiments were performed with a customized acquisition board, named *Nabucodonosor*, designed and built by Giacomo Gervasoni from the I3N group of the Dipartimento di Elettronica, Informazione e Bioingegneria (DEIB). It is basically a four-channel lock-in amplifier, with the four low-noise acquisition channels working in parallel. A generation channel drives the magnetic sensors with a sinusoidal voltage signal of selectable amplitude (from few tens of μV up to 100 mV) and frequency (from few Hz up to 100 kHz). For the experiment of detection of the signal generated by current lines, it supplies an AC current ranging from -1 mA to +1 mA with a resolution down to the μA range. Moreover, the system can control a Kepco generator in order to pilot an electromagnet to perform magnetic field sweeps in the ±14 mT range. The front-end of each acquisition channel consists of a transimpedance amplifier with a remarkably low input voltage noise of about $3\frac{\mathrm{nV}}{\sqrt{\mathrm{Hz}}}$, (AD745 OpAmp from Analog Devices), followed by a Programmable Gain Amplifier, an anti-aliasing filter and an ADC operating at 833 kS/s. Exploiting the parallelism of a Field Programmable Gate Array (FPGA), the four acquired signals are simultaneously processed: phase/quadrature demodulation, selectable filtering and decimation. Finally, data are sent to the PC through a USB connection, where they are managed by a dedicated software.

The device under test (DUT) can be connected to the acquisition system through a VGA port, as for the *in-vitro* experiment, or mounted directly onto the board, as in the earlier characterization stage.

The whole setup is located in a metallic box in order to ensure the electromagnetic screening (Figure 4.17).

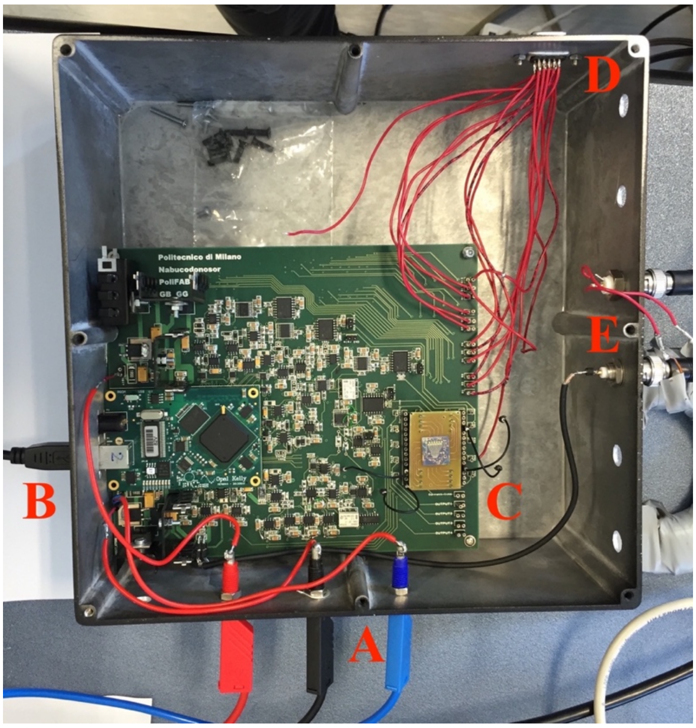

Figure 4.17: *Customized electronic platform Nabucodonosor. (A) Electrical supply. (B) USB port. (C) DUT directly pinned on the board. (D) VGA port. (E) KEPCO input/output.*

4.3.3 Algorithm and simulations

To perform the analysis, the software implemented a binary search algorithm. The current line was fed with a current offset, starting from 500 µA. If the corresponding magnetic field was (not) deemed detected with SNR ≥ 3, then the offset was decreased (increased) by half of its value. If again the signal was (not) detected, the offset was reduced (increased) by half of the previous decrement (increment). This process was iterated until the limit of the detection was reached (SNR = 3). Figure 4.18 illustrates the procedure.

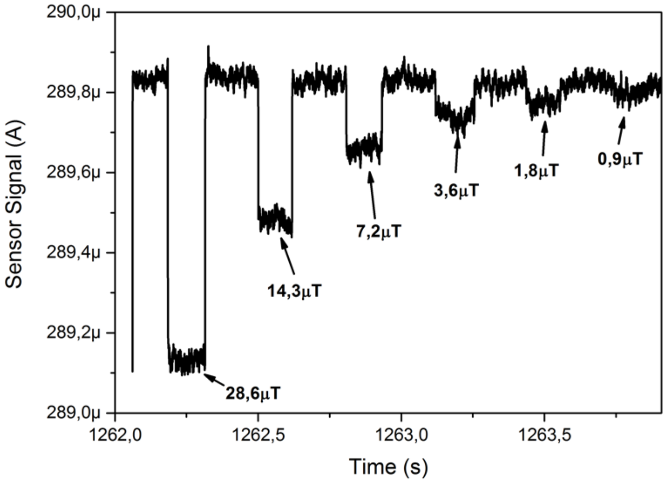

Figure 4.18: *Illustration of how the algorithm works. Each downward pulse is the current variation recorded by the electronic platform due to resistance variations in the magnetic sensor. The pulses are labelled with the amplitude of the magnetic field generated.*

To understand the actual magnetic field in correspondence of the sensor generated by the current supplied into the line, a MATLAB function was implemented. As input parameters, the current flowing in the line (y direction), its section dimensions (thickness and width) and the position (x and z coordinates) with respect to the surface were chosen. The calculation, then, provided the magnetic field component H_x parallel to the surface of the sensor in that given point. Assuming the Au line to be much longer than the sensor in order to neglect border effects, the function decomposed it in infinitesimal wires, each run by a uniform density of current $J = I/A$. Each single wire generated a magnetic field according to the Biot-Savart law and then all these contributes were integrated over the whole section of the current line. The calculations were based on the formula:

$$H_x = \frac{J}{2\pi} \int_{width} \int_{thickness} \frac{(z_0 - z)}{(x_0 - x)^2 + (z_0 - z)^2} dxdz \tag{4.4}$$

Figure 4.19 shows the magnetic field distribution generated by a 30 μA current flowing into the line as a function of the distances from the central axis (horizontal axis) and from the surface (vertical axis). The real distances and dimensions of the sensor are indicated as well. In the sensor structures used for this work, the total distance between the surface of the current line and the active layer of the sensor is about 600 nm.

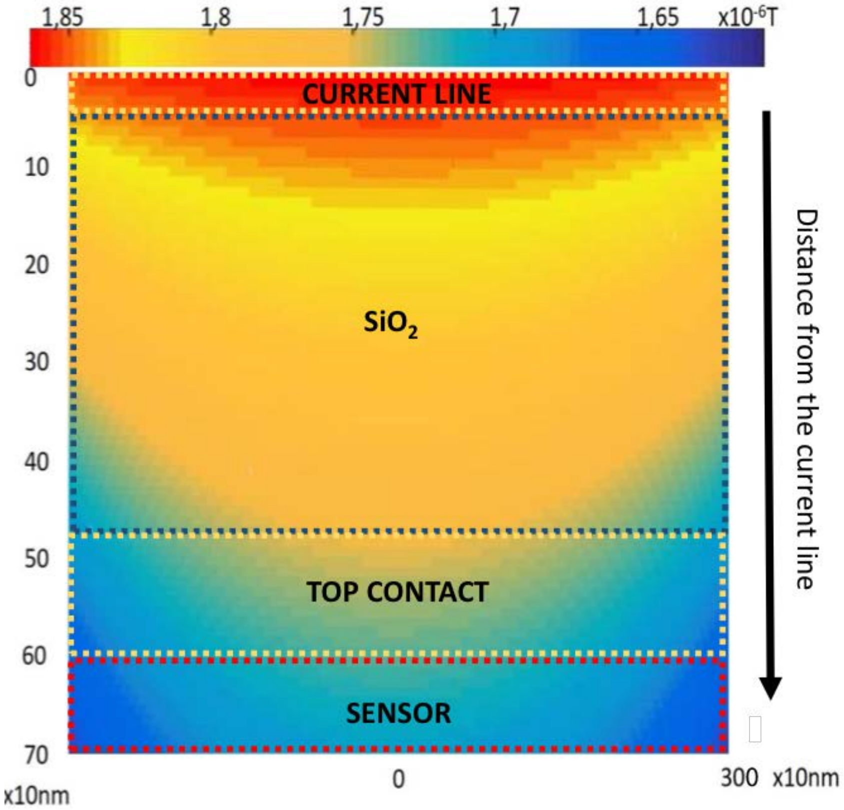

Figure 4.19: *Distribution of the magnetic field generated by a rectangular-shaped wire run by a 30μA current. The active layer of the sensor is about 600nm apart from the surface of the wire.*

As one can see, the decreasing of the field with *z* is quite slow, at least until 700 nm. Besides, the uniformity in the *x* direction is good, in particular in the region around the central axis, where the sensor lays (±1.5 µm).

4.3.4 Results and discussion

The measurements were performed in the more feasible conditions of a broad bandwidth (1 Hz-1 kHz) with the voltage applied to junction ranging from 10 to 90 mV. The platform generated 120-ms rectangular current pulses and acquired the signal with a variable gain, in the range -16/0 dB. The results are presented as contour plots where the horizontal axis is the polarizing magnetic field, the vertical axis is the voltage bias applied to the sensor and the contour lines represent the minimum detected currents (magnetic fields), the color coding going from blue (high field) to red (low field).

In Figure 4.20, the results in case of the MTJ-LOCSENS are reported. As expected from the noise analysis, the best resolution is achieved in the linear region of the characteristic where the sensitivity is the highest. From the graph, it is clear that the region with the best sensitivity is from 4 to 6 mT and that in this region, the minimum detectable current is basically independent on the applied voltage This device is able to detect up to 7 µA, corresponding to about 400 nT, with SNR = 1.

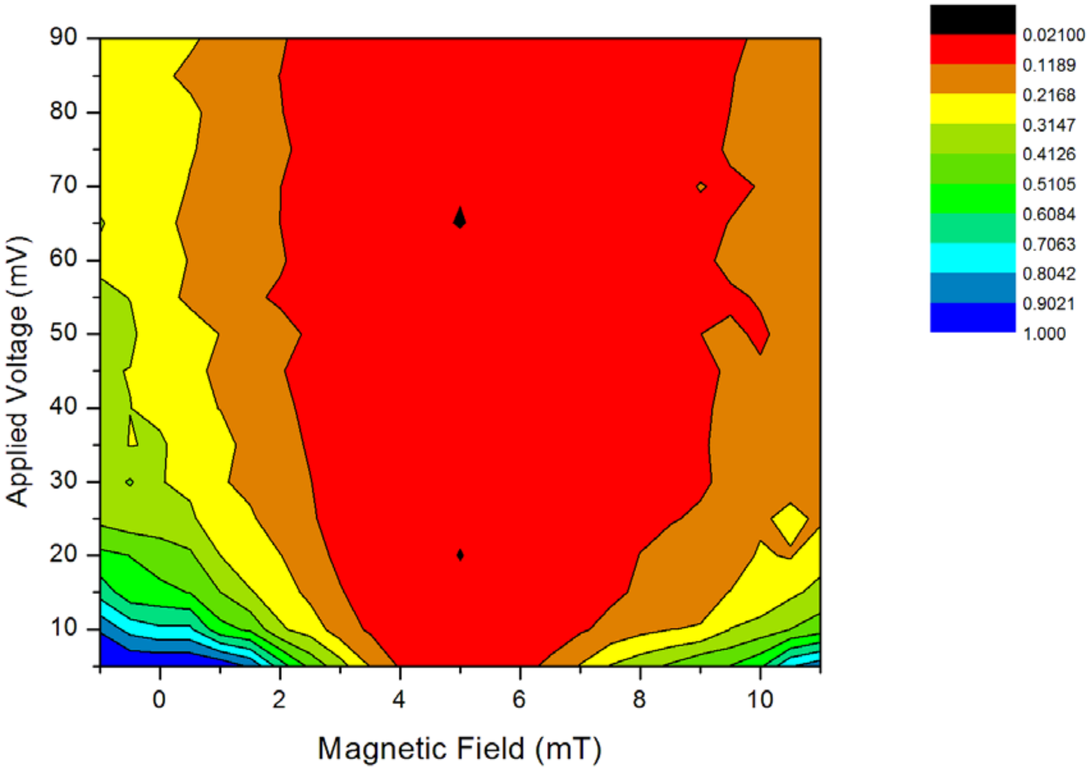

Figure 4.20: *Contour plot of the minimum detectable current as a function of magnetic bias and applied voltage for the MTJ-LOCSENS.*

Despite the performances comparable to those of the MTJ-LOCSENS evinced from the noise characterization, the MTJ-SPINBIOMED shows very poor field detectivity. The map reported a minimum current of about 41 μA, corresponding to 2.3 μT (Figure 4.21(a)). Moreover, one expected the most sensitive region to be the linear one around 4.5 mT (Figure 4.21(b)), however the better sensitivity is achieved operating in the saturated condition at 8.5 mT (Figure 4.20(b)). A possible explanation of these results can be found in the dynamics of the sensor. Figure 4.21(c) presents the magnetic response of the sensor to different magnetic field pulses as a function of time. Starting from the saturated, low-resistance condition of the sensor (external field of -3 mT), the magnetic field was increased with step of 1 mT. Once the new value of magnetic field was applied, the signal of the sensor was acquired until it reached a constant value. From the measurements, it emerges that a very slow dynamic appeared just in the region of maximum sensitivity. A possible explanation is the presence of a sort of magnetic viscosity due to the magnetic domains that obstruct the rotation of the magnetization. Work is in progress to understand the physical phenomena behind this behavior. In the experiments with the current line, the duration of the current pulses (120 ms) is small compared to the magnetic dynamic, which in the order of few seconds, so that a not complete rotation of the magnetization was achieved during a single pulse. As a conclusion, in the region of maximum sensitivity the expected response in term of magnetoresistance is never reached due to the incomplete rotation of the free layer, whereas in the saturated regions, the dynamic is faster and the sensor behavior is similar to the theoretical one. On top of that, the non-negligible hysteresis does not allow fast and sequential measurements as the algorithm perform.

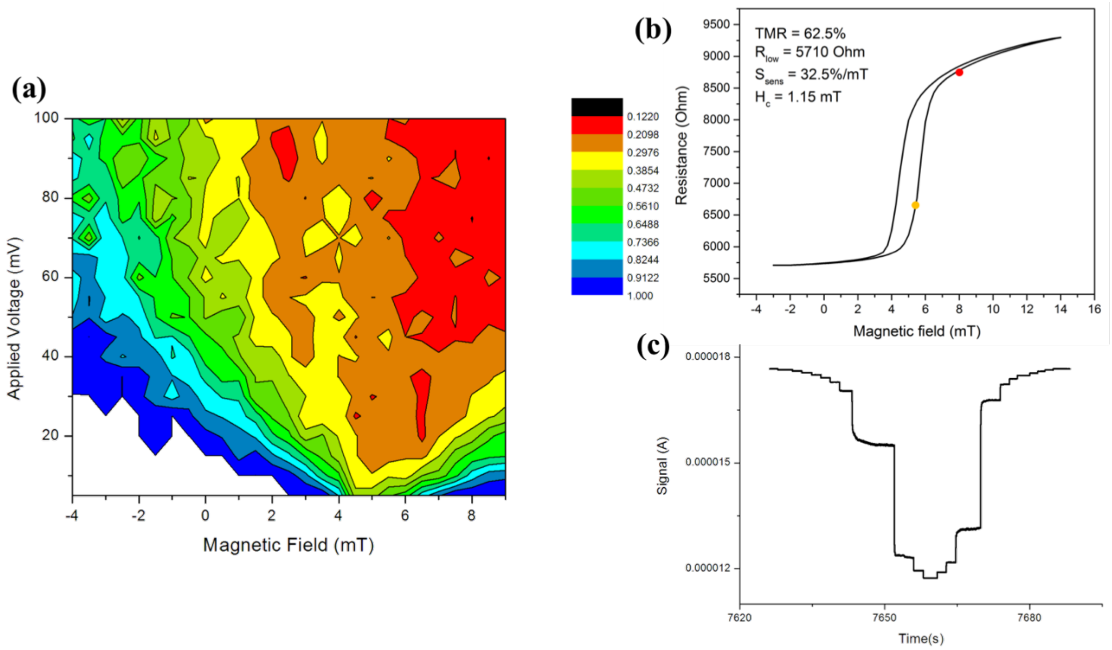

Figure 4.21: *(a) Contour plot of the minimum detectable current as a function of magnetic bias and applied voltage for the MTJ-SPINBIO. (b) Position on the R(H) curve of the actual (red point) and expected (orange point) most sensitive region. (c) Time-domain graph showing the dynamics of the sensing layer.*

The MTJ-AlOx shows a behavior very similar to the MTJ-LOCSENS, with the best resolution in correspondence of the linear region (4-6 mT). However, the signal is altered by a strong random telegraphic noise (RTN), which interferes with the correct performance of the algorithm (Figure 4.22(b)). As one can see from the red circle in the inset, the RTN gives disturbance on a temporal scale comparable to that of the current pulses. As a result, the minimum detected signal is about 37 μA (2.1μT).

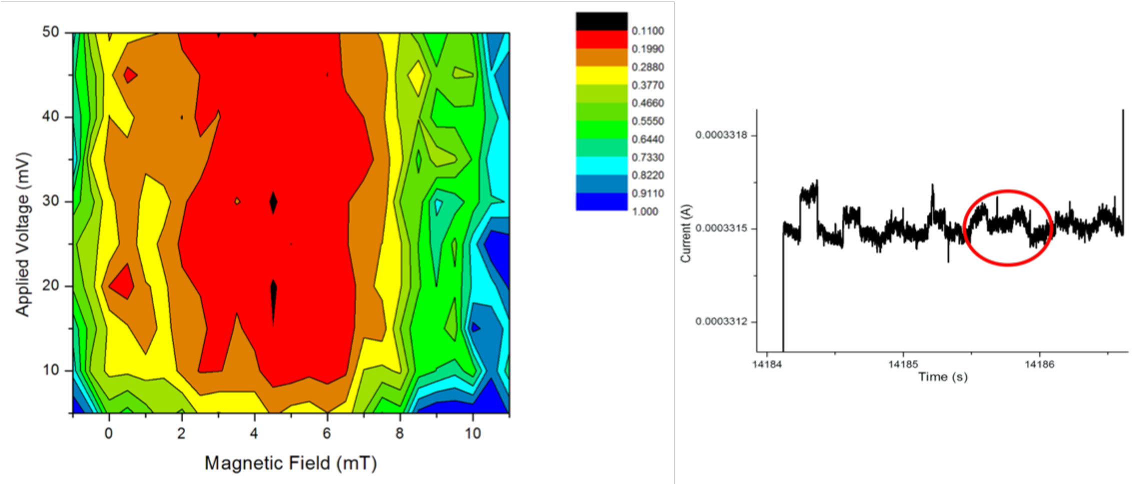

Figure 4.22: *(a) Contour plot of the minimum detectable current as a function of magnetic bias and applied voltage for the MTJ-AlOx. (b) Time-domain graph showing the consistent RTN disturbing the algorithm.*

Differently from the other sensors, the GMR-SV sensitivity shows a quite strong dependence on the applied voltage, as well as on the external magnetic field. For low voltages, the resolution grows proportionally with the applied voltage. However, after a certain threshold, the growth of the $1/f$ noise, proportional to V^2 limits the gain. In the linear zone at 3 mT, with 80 mV applied voltage, the limit of detection is 4 μT, resulting the worst among the analyzed devices (Figure 4.23).

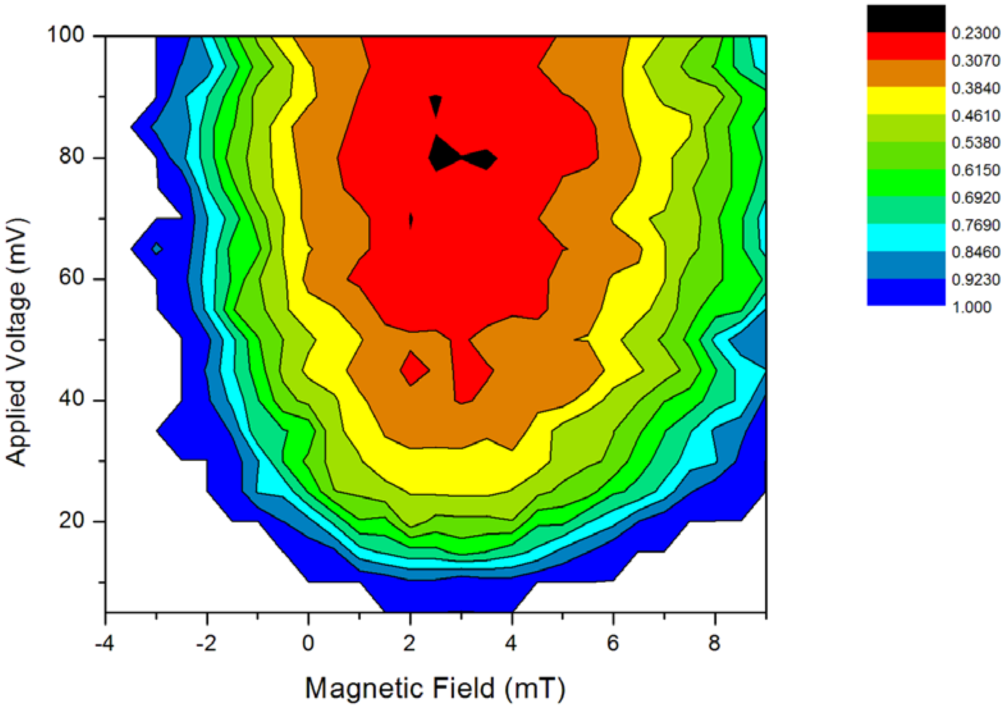

Figure 4.23: *Contour plot of the minimum detectable current as a function of magnetic bias and applied voltage for the GMR-SV.*

4.4 Conclusions

Despite the noise figures, the dynamics of the MTJ-SPINBIOMED limits its actual resolution. Regarding the MTJ-AlOx, its sensitivity, measured with the current lines measurements (2.1 μT), appears better than that predicted by the noise analysis (6 μT). Since the other sensors show consistent results between noise measurements and current lines experiments, one can exclude a failure in the calculation of the minimum detectable field starting from the minimum detected current. Therefore, the explanation of this inconsistency can be found in the random telegraphic noise, which accidentally adds to the real signal arising from the sensors, so that the software recognizes ad “detected” signal well below the theoretical LOD of the sensors. On the other hand, the current lines measurements confirm that, despite having good noise performances, the GMR-SV results too limited by its scarce sensitivity. Finally, the better results are achieved by the MTJ-LOCSENS.

Furthermore, it must be noted that the minimum detectable signals were always greater than the theoretical limits. The reasons for that might be due to unavoidable disturbances in the connections and also to some uncertainty on the applied field.

Table 4.3 gives an overview of the minimum detectable fields and reports also the theoretical LODs as a comparison.

Table 4.3: *Experimental resolutions in 1 Hz-1 kHz BW. The theoretical limit of detection is reported as a comparison.*

	MTJ-LOCSENS	***MTJ-SPINBIOMED***	***MTJ-AlOx***	***GMR-SV***
Current resolution @SNR=1	*7 μA*	*41 μA*	*37 μA*	*77 μA*
Field resolution @SNR=1	*400 nT*	*2.3 μT*	*2.1 μT*	*4 μT*
Theoretical LOD	*250 nT*	*430 nT*	*6 μT*	*1.15 μT*

Chapter 5: In-vitro *measurements*

This chapter deals with the realization of the platform for the recording of neural signals arising from rat hippocampal slices. These biological samples feature a dense assembly of fibers which, when electrically stimulated, result in a potentials activation of several hundred cell bodies, giving rise to a much stronger magnetic field with respect to the single neuron case. The target signals can be the fast spiking activity due to neuronal action potentials or slow local field potential in the extracellular space around the neurons. J. Amaral et al. evaluated the extracellular signal to be over 2.5 µT [44] at 10 µm. The brain slice is therefore an interesting tool in order to validate a MTJ-based platform for the neural activity recording.

A compact acquisition setup was developed, enabling us to integrate the biological techniques with the electronic instrumentations. The magnetic measurements from the sensors were supported by standard Local Field Potential (LFP) recordings in order to verify the signal quality and to have reference values.

In the following, firstly the biological system is presented. Then the technological issues are discussed. Finally, the results of the measurements are reviewed.

5.1 Hippocampal brain slices

Since the direction of the magnetic signal is a critical requirement in our recording platform, in order to carry out our experiments we needed a biological system where the neuronal fibers were all parallel and as linear as possible. Keeping into account this requirement, the hippocampus was recognized by the neurophysiological group as the most promising biological structure to study.

5.1.1 Hippocampus anatomy

The hippocampus is a major component of the brain of humans and other vertebrates and plays an important role in many activities, such as memory consolidation and spatial navigation. Since different neuronal cell types are neatly organized into layers in the hippocampus, it has frequently been used as a model system for studying neurophysiology.

The anatomy of the hippocampus is illustrated in Figure 5.1. A neuronal signal comes in from the Entorhinal Cortex (EC) through the Perforant Path (PP) and stimulates all the granule cells in the Dentate Gyrus (DG). Their responses go to the pyramidal cells in the proximal region of the Cornu Ammonis (CA3) and then they travel along a bundle of fibers, called Schaffer Collaterals (SC), until they reach the distal region of Cornu Ammonis (CA1).

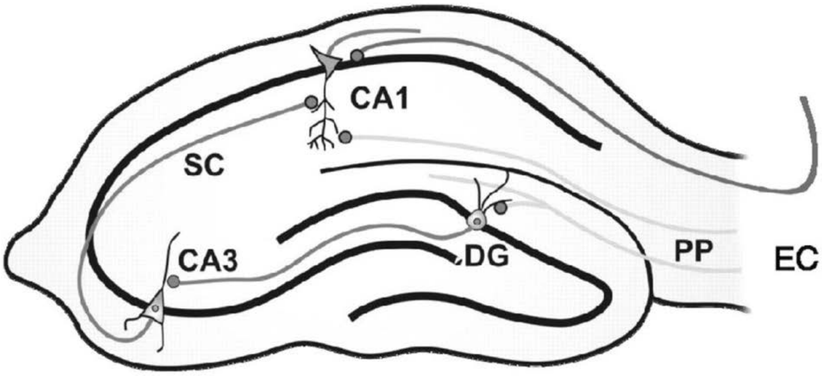

Figure 5.1: *Sketch of the rat hippocampal formation. A neuronal signal comes in from the Entorhinal Cortex (EC) through the Perforant Path (PP) and stimulates all the cells in the Dentate Gyrus (DG). Their responses go to the pyramidal cells in the proximal region of the Cornu Ammonis (CA3) and then they travel along a bundle of fibers called Schaffer Collaterals (SC) until they reach the distal region of Cornu Ammonis (CA1).*

In this framework, the most suitable regions to investigate were DG and CA1. Since the Neurophysiology group was more familiar with the handling of DG, the latter was chosen. In this region, it is possible to investigate the incoming axon from the PP synapsing onto the granule cells of DG.

In order to operate in the best possible conditions, the cells in the slices can be doped by administrating bicuculline. Bicuculline is a phthalide-isoquinoline compound that acts as a competitive antagonist of GABA receptors. Since it blocks the inhibitory action of GABA receptors, the action of bicuculline mimics epilepsy. Therefore, it was used to enhance the excitatory response of the neurons.

To distinguish biological signals from electrical ones, the tetrodotoxin (TTX) was used. TTX is a powerful neurotoxin, which inhibits the firing of action potentials in nerves by binding to the voltage-gated sodium channels in cell membranes and blocking the passage of sodium ions (responsible for the rising phase of an action potential) into the neuron [96]. Then if a signal disappears after the administration of TTX, it will probably have a biological origin.

5.1.2 Local field potential recordings

To investigate the propagation of the neuronal signal in the hippocampus, the Local Field Potential (LFP) technique was employed. The LFP is the electric potential recorded in the extracellular space in brain tissue, typically using micro-electrodes. Many studies demonstrated that action potentials have a limited participation to the genesis of the LFP [97]–[99]. Currently, it is thought that it mainly arises from the summation signal of excitatory and inhibitory dendritic potentials from a large number of neurons in the neighborhood of the recording site [29]. A possible explanation is that brain tissue exerts strong frequency-filtering properties. High frequencies (greater than ≅100 Hz), such as that produced by axonal action potentials (of the order of 1kHz), are subject to steep attenuation, while low-frequency events, such as synaptic potentials, attenuate less with distance. Consequently, the extracellular image of action potentials is visible only for electrodes immediately adjacent to the recorded cell, while synaptic events may propagate over large distances in extracellular space [100].

Figure 5.2 shows an example of a LFP detection scheme [29]. Within a 50-μm radius, the four-wire electrode is still able to detect the spiking activity (~60 μV), originating from about 100 neurons. On the other hand, looking at the slow extracellular potentials, neurons within a radius of 140 μm, containing ~1000 neurons in the rat cortex, can be detected.

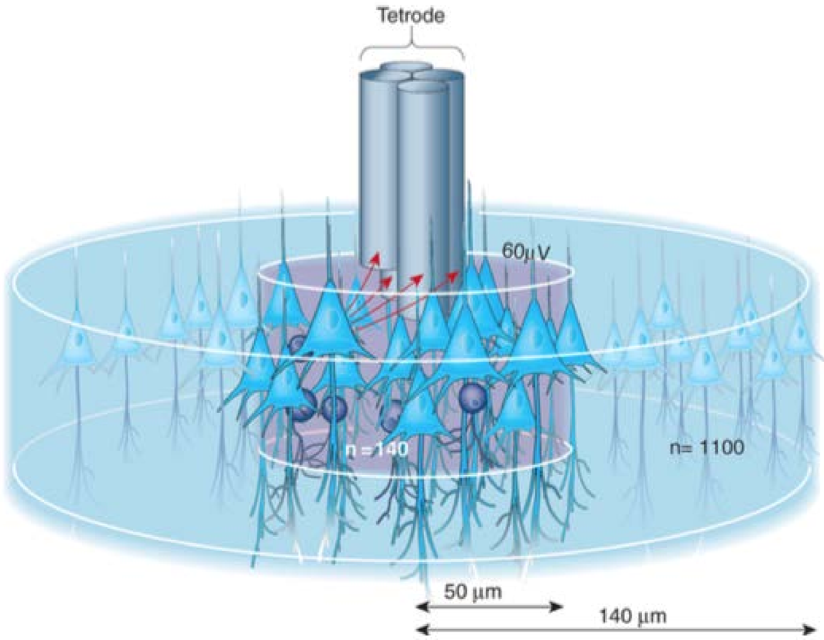

Figure 5.2: *Example of a LFP detection scheme. Within a 50-μm radius, the four-wire electrode is still able to detect the spiking activity (~60 μV), originating from about 100 neurons. On the other hand, looking at the slow extracellular potentials, neurons within a radius of 140 μm, containing ~1000 neurons in the rat cortex, can be detected. From [29].*

5.1.3 Slice preparation

Concerning the preparation of the brain slices, the biological samples came from C57BL/6J mice of either sex aged 3 weeks to 6 months (Charles River Laboratories International, Wilmington, MA, USA). All the experiments were carried out in accordance with the guideline as established by the European Community Council (Directive 2010/63/EU of September 22nd, 2010) and experimental protocols were approved by the Italian Ministry of Health. Animals were anaesthetized with isoflurane prior to decapitation. Transverse hippocampal slices (350 μm thick) were cut using a Microm HM 650 V microtome equipped with a Microm CU65 cooling unit (Thermo Fisher Scientific, Waltham, MA). Slices were cut at ≅2°C in a high-sucrose protective solution containing (in mM): 87 NaCl, 25 $NaHCO_3$, 2.5 KCl, 0.5 $CaCl_2$, 7 $MgCl_2$, 25 glucose, 75 sucrose, and saturated with 95%

O_2 and 5% CO_2. Slices were incubated for 30–45 min at 35 °C and for at least another 30 min at room temperature in an artificial cerebrospinal fluid (ACSF) containing (in mM): 125 NaCl, 25 $NaHCO_3$, 25 glucose, 2.5 KCl, 1.25 NaH_2PO_4, 2 $CaCl_2$, and 1 $MgCl_2$ (bubbled with 95% O_2–5% CO_2). During the recording sessions, the ACSF was perfused at a rate of 2.5 ml/min [101].

5.2 MTJ sensor fabrication

From the analysis performed in the previous chapter, MTJ-LOCSENS resulted to be the best kind of sensor in term of sensitivity. However, the sensors were further improved in terms of performances and layout. These sensors were labelled MTJ-UMANA. After a fine tuning of the layers' thickness, they achieved a TMR ratio of about 50% and a sensitivity of 12-13%/mT, at the same time maintaining an almost hysteresis-free behavior.

As discussed in Paragraph 2.4, for sensing applications a linear sensor response with low hysteresis is desirable because it allows a straightforward relationship between the external magnetic field and the electric signal acquired from the sensor. Since the magnetization of the reference layer is pinned through the synthetic antiferromagnet (SAF) and exchange bias and it is insensitive to the external magnetic field (at least for small values), the sensor characteristics R(H) is determined by the hysteresis loop of the free layer. For obtaining the desired magnetic response of the free layer, different strategies can be employed. The method used in this work relies on the use of shape anisotropy and superparamagnetic transition of $Co_{0.4}Fe_{0.4}B_{0.2}$ to achieve a configuration where the magnetization of the sensing layer lays perpendicularly to that of the reference layer (see Paragraph 2.4).

The following paragraphs describe all the steps involved in the realization of the MTJ biosensors:

-Growth by magnetron sputtering of the sensors stack;

-Microfabrication of the sensor arrays;

-Thermal annealing and sensors characterization.

5.2.1 Growth of the stack

The AJA Orion 8 magnetron sputtering system described in Section 3.1 was used for depositing the sensor structures. The deposition conditions were optimized in terms of low surface roughness and uniform topography [66]. The sensor layers were deposited at base pressure of about 10^{-9} Torr. $Co_{0.6}Fe_{0.4}$ and MgO layers were sputtered in RF mode, while all the other layers in DC mode. During deposition, a 30 mT magnetic field was applied in-plane with respect to the sensor surface to fix the direction of the magnetocrystalline anisotropy in the ferromagnetic layers. Table 5.1 summarizes the growth conditions for each layer. These requirements are crucial for promoting the correct crystallization of the layers, thus ensuring a high quality of the tunneling barrier, and for avoiding Néel coupling and shortcuts between the ferromagnetic electrodes of the junctions, both arising from a rough surface.

Table 5.1: *Optimal sputtering growth conditions for each layer.*

Layer	*Ar pressure (mTorr)*	*Target power (W)*	*Dep. Rate (Å/min)*
Ta	*3*	*100 (DC)*	*37.2*
Ru	*3*	*50 (DC)*	*22.5*
$Ir_{0.2}Mn_{0.8}$	*3*	*50 (DC)*	*32*
$Co_{0.6}Fe_{0.4}$	*12*	*200 (RF)*	*19*
$Co_{0.4}Fe_{0.4}B_{0.2}$	*3*	*58 (DC)*	*12.3*
MgO	*2*	*220 (RF)*	*3.2*
SiO_2	*2*	*280 (RF)*	*5.5*
Au	*5*	*10 (DC)*	*41*
Ti	*5*	*20 (DC)*	*7.9*

MTJs were fabricated on top of Si/SiO_2 3-inch wafers. The wafer was first cleaned with acetone and IPA. Before depositing the sensor stack, the substrate underwent a soft etch in vacuum (20 minutes at 20W in RF mode, Argon pressure of 2 mTorr) in the same sputtering system, in order to remove contamination from the exposition to air (CO, CO_2, N_2, O_2, H_2O molecules and other particles).

The structure of the MTJ stack has been described in section 2.3, focusing on the role played by each functional layer. A careful optimization of the thickness of the layers and of the field cooling process was required, in particular for $Ir_{0.2}Mn_{0.8}$/ $Co_{0.6}Fe_{0.4}$/ Ru/ $Co_{0.4}Fe_{0.4}B_{0.2}$ synthetic antiferromagnet in order to maximize the magnetic coupling and obtain the desired magnetic response and of the $Co_{0.4}Fe_{0.4}B_{0.2}$ free layer, in order to achieve a superparamagnetic status, while preserving the magnetoresistance ratio (see Section 2.3.3). The complete stack consisted of the following layers (with thicknesses expressed in nm): Ta (5)/ Ru (18)/ Ta (3)/ $Ir_{0.2}Mn_{0.8}$ (20)/ $Co_{0.6}Fe_{0.4}$ (1.7)/ Ru (0.9)/ $Co_{0.4}Fe_{0.4}B_{0.2}$ (2.7)/ MgO (2.2)/ $Co_{0.4}Fe_{0.4}B_{0.2}$ (1.25)/ Ru(5)/ Ta (20). The MgO thickness is determined by previous calibrations performed by NaBiS group, in order to obtain a junction resistance of few kΩ, as required in order to have small thermal and flicker noise (see Paragraph 4.2).

The microfabrication process used to pattern the sample will be described in the following section.

5.2.2 Microfabrication of sensor arrays

After deposition, the sensor stack was patterned by a multistep procedure which consisted of 3 optical lithographic processes, 2 ion milling steps and 2 sputtering depositions. Figure 5.3 shows the final layout of the sensors array. On a 14 mm x 17 mm chip, an array of 12 MTJ-based sensors was realized, each provided with a top contact and a common bottom contact (ground). In this way, each sensor could be addressed independently. The wafer used as substrate allowed us to produce ten chips in parallel, resulting in a total of 120 discrete sensors.

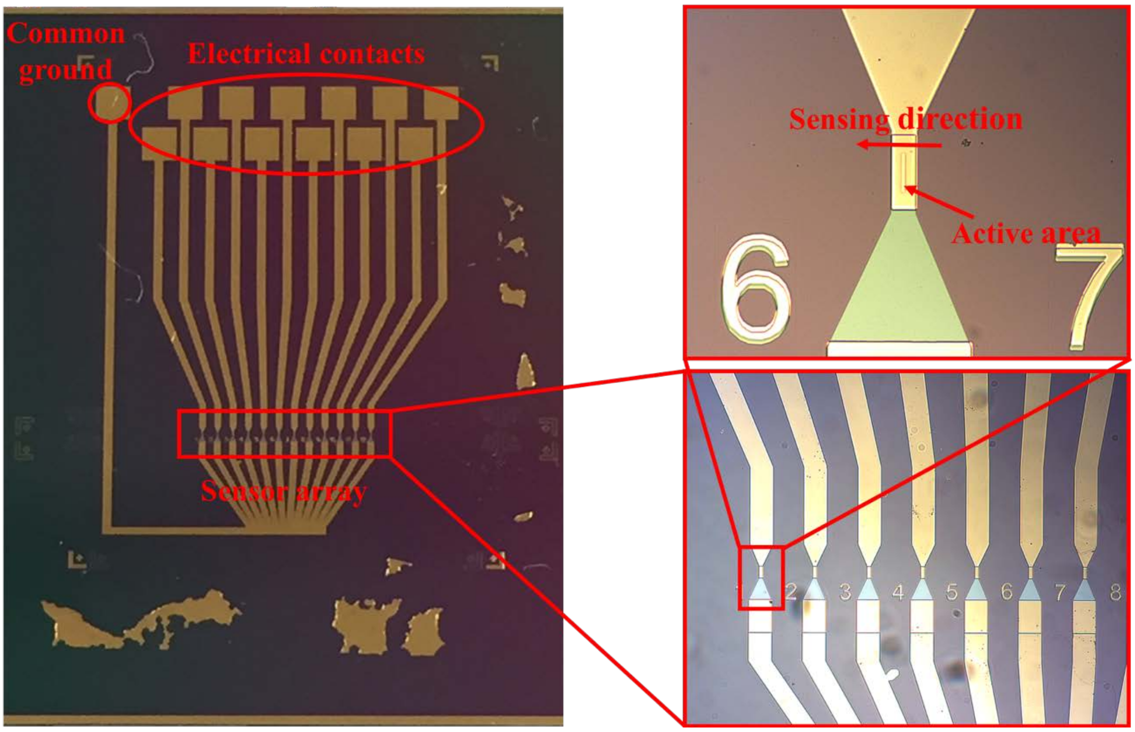

Figure 5.3: *Layout of a single chip with zooms on the sensors array.*

The following three steps were performed to fabricate the sensors:

-Step 1: definition of MESA and bottom contact (mask 1).

-Step 2: definition of junction geometry (mask 2).

-Step 3: definition of electrical contacts (mask 3) and contact deposition.

-Step 1: the definition of the MESA, which included the junction area and the bottom contacts area, was realized through a direct lithographic process and an ion milling step.

First, the sample was cleaned with acetone and IPA. Then the photoresist was spin-coated on the sample and then the sample was pre-baked on a hot plate. Subsequently, the sample was exposed using mask 1 (Figure 5.4) and developed. The following ion beam etching process defined the MESA. The whole stack was etched until the SiO_2 substrate is exposed and finally the resist was lifted-off. Table 5.2 shows the optimized parameters employed in this step.

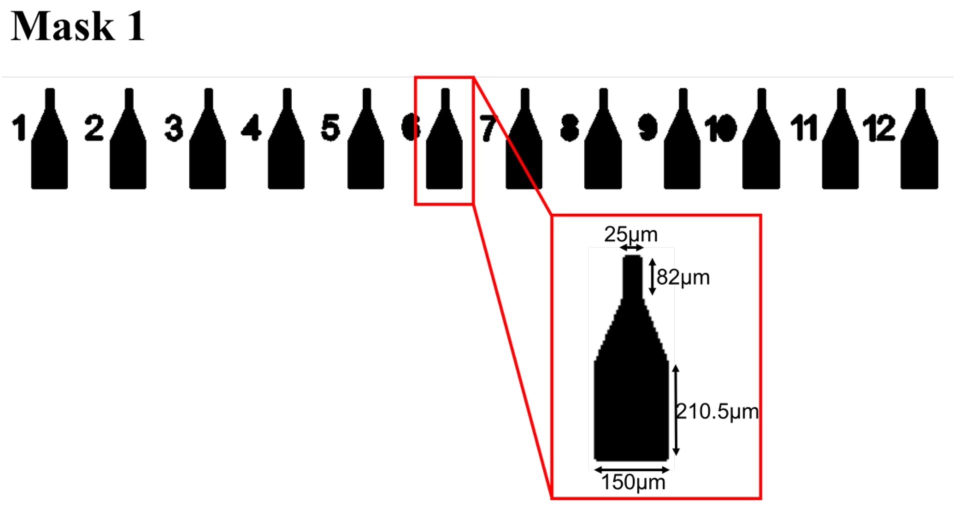

Figure 5.4: *Mask 1 for the definition of the MESA.*

Table 5.2: *Optimized parameters for the first step.*

Phase	***Parameters***
Spin Coating And Baking	*AZ5214E positive resist, 1.4-µm thick, baked at T=110°C for 90s*
Exposure	*Dose =* $128 mJ/cm^2$
Development	*35” in pure AZ726MIF Developer*
Etching	$V_{dis}=200$ *V,* $V_{acc}=600$ *V*
Lift-Off	*AZ100 Remover at 70°C*

-Step 2: In this step, the actual shape of the sensing area was defined carving a pillar in the MESA. This process involved a direct lithography process, ion milling and a sputtering deposition of an insulating material. The lithographic steps were the same as those of the MESA definition, apart from the use of mask 2 (Figure 5.5). The subsequent etching procedure was the crucial step for the sensor functionality. The pillar had to be etched down to the $Ir_{0.2}Mn_{0.8}$ layer while over or under-etching could, respectively, result in a too high resistance of the bottom contact or in shortcuts between the top and bottom contacts. Therefore, calibration samples were employed during the etching process. The junction area had a quite high aspect ratio ($3x40\ \mu m^2$) in order to exploit the shape anisotropy to achieve a linear response of the sensor to the external magnetic field, arising from crossed anisotropies of the free and reference layer. In particular, the magnetization of the free layer laid parallel to the long edge of the junction, while the reference layer was pinned in the orthogonal direction by the SAF, thus defining the sensing direction (see Paragraph 2.4).

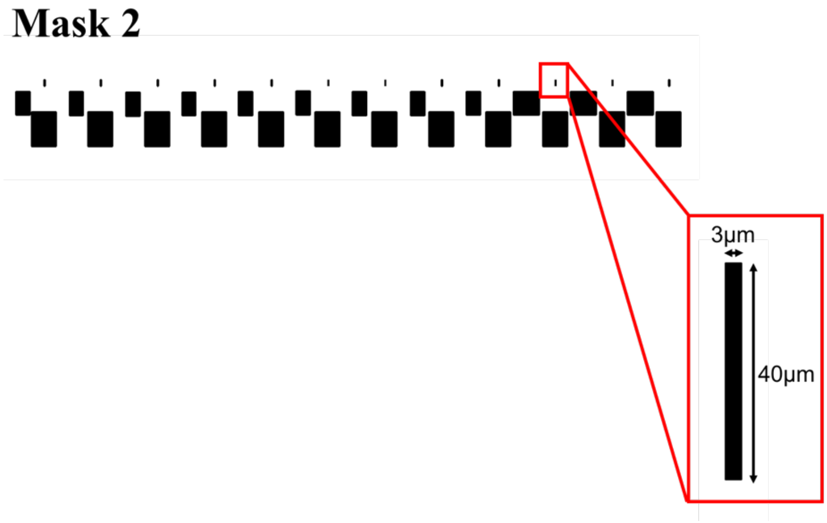

Figure 5.5: *Mask 2 for the definition of the junction.*

For the junction definition, the ion beam etching was performed tilting the sample at 30° and subsequently at 60° with respect to the beam direction, in order to avoid re-deposition of the etched material and to define sharper sensor edges. In Table 5.3, the optimized parameters of this step are listed.

Table 5.3: *Optimized parameter for the second step.*

Phase	***Parameters***
Spin Coating And Baking	*AZ5214E positive resist, 1.4-µm thick, baked at T=110°C for 90s*
Exposure	*Dose = 128mJ/cm*^{2}
Development	*35" in pure AZ726MIF Developer*
Etching	V_{dis}*=200 V,* V_{acc}*=600 V*
Lift-Off	*AZ100 Remover at 70°C*
SiO_2 *Deposition*	*100nm, optimized conditions (Table 3.1)*

After the etching, a 100-nm SiO_2 insulating layer was deposited by magnetron sputtering to electrically insulate the bottom contacts from the top ones. When the resist was stripped, the bottom contacts and the junction area were exposed for the subsequent contact definition step.

-Step 3: In this step, the areas for the deposition of the metal contacts were defined through an image reversal lithographic process using mask 3 (Figure 5.6). After this last lithographic step, a 30 minutes soft etch was performed before the contact deposition, in order to remove eventual residuals of resist or the thin layer of Ta oxidized due to air exposure. The contacts were made up of a Ti (7nm)/Au 200(nm) bi-layer. The Ti and the first 20 nm of Au were deposited by sputtering in the AJA Orion system, while the process is ultimate with the Leybold machine. The thin titanium layer favors the adhesion of Au to the underlying Ta surface. The optimized parameters are listed in Table 5.4.

Table 5.4: *Optimized parameters for the third step.*

PHASE	***PARAMETERS***
Spin Coating And Baking	*AZ5214E positive resist, 1.4-µm thick, baked at T=110°C for 90s*
Exposure	*Dose = 128mJ/cm^2*
Reversal Baking	*T=115° for 90s*
Flood Exposure	*Dose = 254mJ/cm^2*
Development	*35” in pure AZ726MIF Developer*
Soft Etch	*30min at 10W, 2mTorr Ar pressure*
Ti Deposition	*100nm, optimized conditions (Table 3.1)*
Au Deposition	*100nm, optimized conditions (Table 3.1)*
Lift-off	*AZ100 Remover at 70°C*

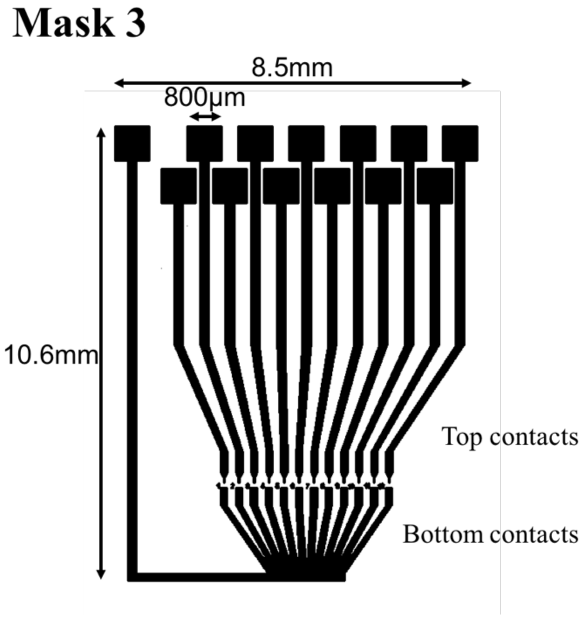

Figure 5.6: *Mask 3 for the definition of electric contacts.*

Figure 5.7 shows a lateral view of a sensor after the microfabrication process. The top pad was in ohmic contact with the top $Co_{0.4}Fe_{0.4}B_{0.2}$ electrode of the MTJ, while the bottom contact, deposited on the MESA, provided the contact with the bottom $Co_{0.4}Fe_{0.4}B_{0.2}$ electrode by tunneling through MgO. Because of the large MESA area, in the bottom contact the MgO film was likely to have a larger number of defects with respect to the sensor area, therefore the current found conductive paths making the bottom contact resistance negligible with respect to the junction, which was defined on a much smaller area.

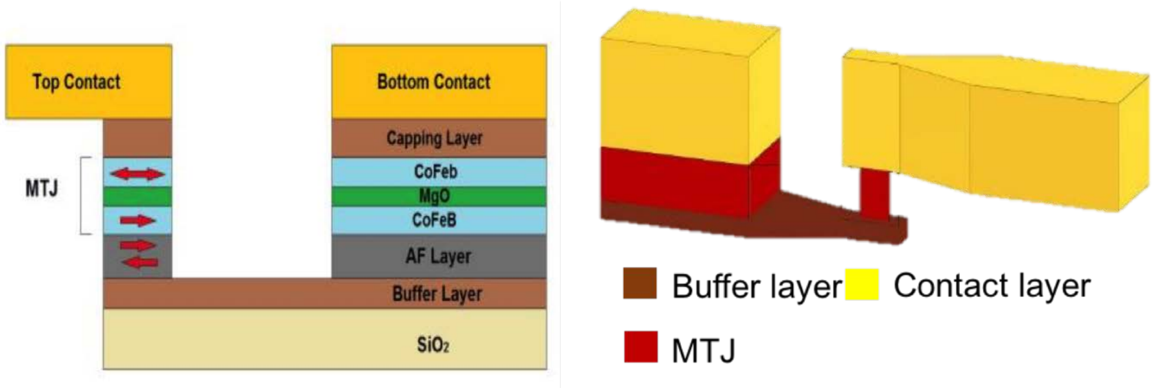

***Figure 5.7:** (left) Lateral and (right) 3D representation of a sensor after the contact deposition. The surrounding is filled with SiO_2.*

Finally, in order to assure biocompatibility and to protect the sensors from the biological environment, the chips were terminated with a SiO_2(50)/Si_3N_4(50)/SiO_2(50) tri-layer capping deposited by Chemical Vapor Deposition (CVD).

5.2.3 Thermal annealing

After the lithographic processes, an annealing was performed in order to improve the crystalline quality of the sample. It consisted in a 1-hour baking in vacuum at a temperature carefully chosen. The temperature should be high enough to guarantee a significant improvement in the crystalline quality of the MgO and $Co_{0.4}Fe_{0.4}B_{0.2}$ layers; in turn, a too high temperature would disrupt the properties of the stack, mainly due to interdiffusion of atoms between the layers. From previous works, it is known that the optimal annealing temperature is around 270 °C.

Since the annealing temperature was above the blocking temperature of the antiferromagnet, the annealing was followed by a field cooling process in order to fix the direction of the reference layer. To do so, a field of ~0.4 T was applied by a permanent magnet in the direction parallel to the short edge of the junction.

The used setup is the one described in Paragraph 3.4.

5.2.4 Characterization

Once the fabrication process was completed, the MR properties of the sensors were characterized. A R(H) curve was recorded with a two-point measurement, both before and after the annealing to check the actual improving of the performances (**Figure 5.8**). The final result is a device with a TMR ratio of about 50% and a sensitivity of some 30% larger than that of a MTJ-LOCSENS.

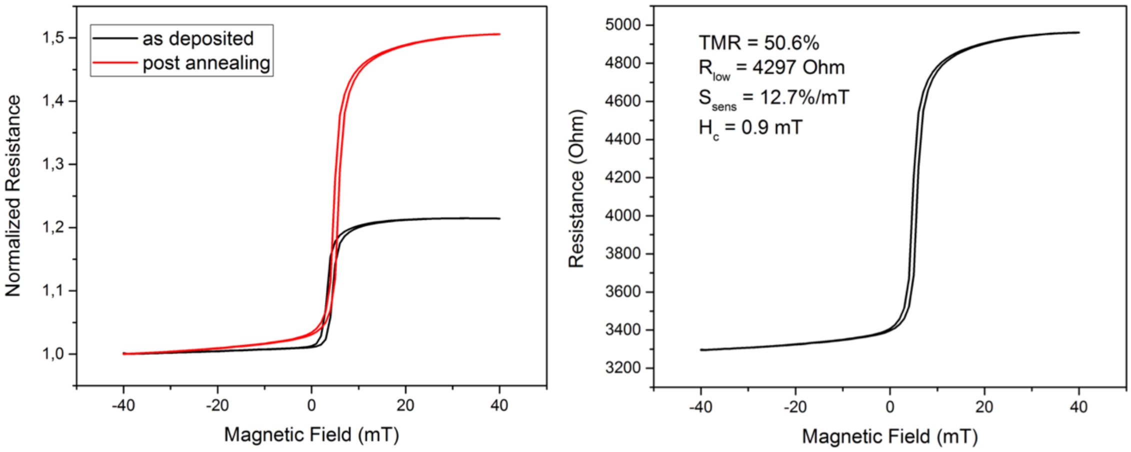

Figure 5.8: *(a) Comparison between the characteristics of the as-deposited (black) and post-annealing (red) states. The TMR ratio increases significantly during the process, from about 20% up to touching 50%. (b) MR properties of the annealed sensor.*

5.3 Acquisition setup

The experiments required the realization of a dedicated acquisition setup, which involved the optimization of several aspects.

A custom two-faces printed circuit board (PCB), with a mass plane on one side and copper contact pads on the other, was designed in order to provide compatibility with LFP recording and to allow the insertion of a culture chamber in which the brain slices were maintained in the cerebrospinal fluids. Two different solutions to connect the chips to the PCBs were studied.

In the first one, the PCB pads were aligned to the sensors pad and the attachment was realized by means of an anisotropic conductive tape (Adafruit 3M). The PCB was holed in correspondence to the active area of the sensors and a culture chamber was sealed on top. The sealing was performed through the silicon-based organic polymer PolyDiMethylSiloxane (PDMS), which was fabricated by mixing the elastomer and the curing agent in a 10:1 ratio and cured at 60°C for two hours (**Figure 5.9**).

The alternative solution consisted in wire-bonding the chip to the PCB conductive tracks. Then, to protect the bonds from the biological environment, they were covered by a two-component epoxy (SC2001 Electrolube), which was realized mixing the resin and the hardener in a 1:1 ratio and curing at 70°C for 25 minutes. The PCB was holed so that to accommodate the whole chip and a second PCB was attached beneath as a support. In this case, the culture chamber was not needed because, once sealed with PDMS, the hole was large enough to act as a culture chamber itself (Figure 5.10).

During the early characterization stages, it was found that after some time of operation the conductive tape lost its conductive properties. This fact could be due to the overheating that disrupted the molecular order of the material. In fact, the glue of the tape contained micro-particles that, suitably oriented in space, allowed the conduction only along the *z* direction.

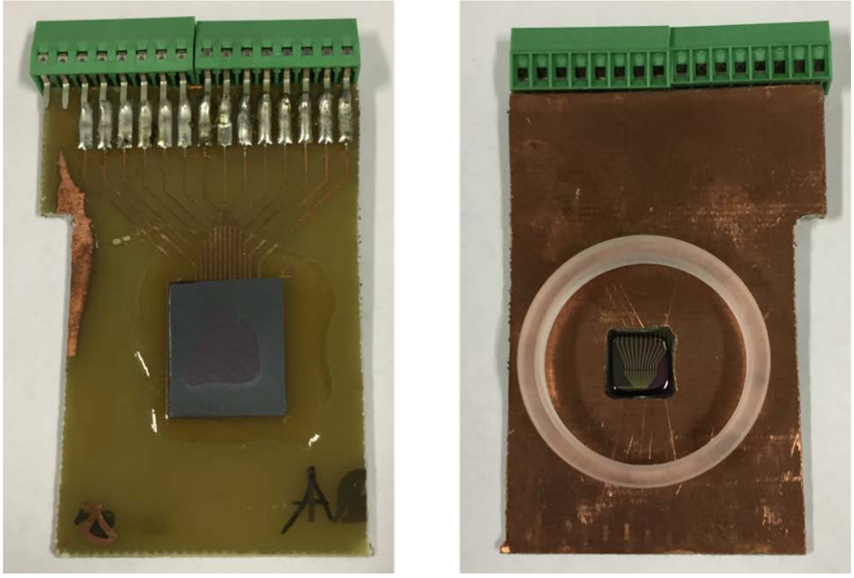

Figure 5.9: *Chip attached to the PCB with anisotropic conductive tape. The hole was sealed with PDSM and on top the culture chamber was glued.*

Figure 5.10: *Chip bonded to the pads of the PCB. Then in order to protect the bonds from the biological environment, they were covered in a two-component epoxy. The hole, sealed with PDMS, is large enough to act as culture chamber itself.*

Consequently, we discarded the latter option and opted for the bonding, which offered stable and durable operative conditions.

In both cases, the PCB pads were then connected to the electronic board *Nabucodonosor* (see Section 4.1.2) through a VGA port, allowing to remotely control the acquisition procedure.

The detection scheme exploited the sensitivity of the junction's free layer to detect the neuronal magnetic field. This resulted in a variation of the sensor's resistance and the platform read the consequent changes in the current, plotting the data in real-time. The platform can acquire 4 channel in parallel.

To prove the magnetic origin of the signal recorded by the platform, it was necessary to perform two measurements: one with the sensor polarized in the linear region and one at saturation (control) (Figure 5.11). In fact, if signals of the same entity are recorded in both the conditions, i.e. when the magnetic sensitivity is maximum or basically null, one can conclude that its origin is mainly due to a capacitive coupling. For capacitive coupling, it is meant that the biological medium acts as a dielectric between two electrodes, represented by the sensor's metallic paths and the stimulation electrode itself. Then an AC electrical bio-signal or the stimulation signal can pass through it, from one electrode to the other, independently form the magnetic response of the slice.

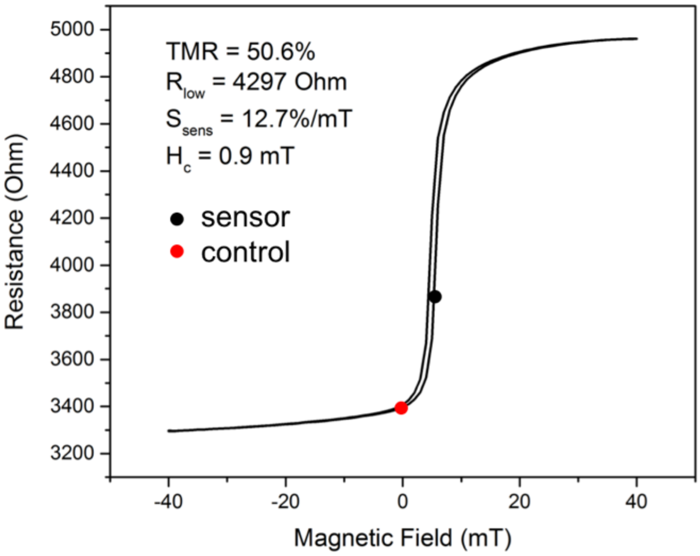

Figure 5.11*: Graphical illustration of sensor's and control's operating points of.*

The magnetic polarization was achieved by means of an electromagnet. Originally, the idea was to use two permanent magnets, suitably placed to obtain the desired magnetic field, because of the low noise introduced in the measurement. However, the difficulties encountered in vary at will the magnitude of the bias convinced us to employ the electromagnet.

The workstation at the IIT's facility consisted in an optical bench surrounded by a Faraday cage, on which an upright optical microscope for electrophysiology and the setup for slice stimulation were placed (Figure 5.12).

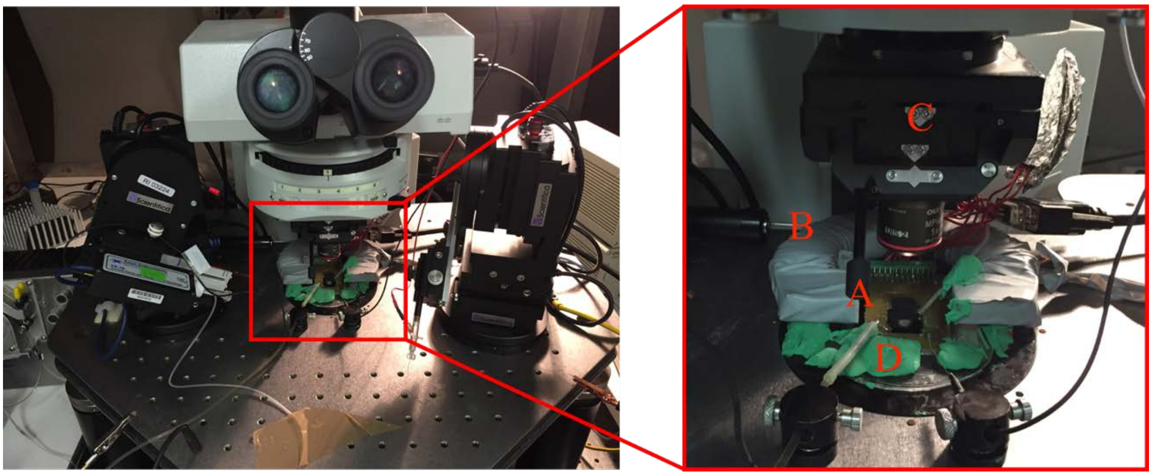

Figure 5.12: *Work station at the IIT's facility. On an optical bench were placed: (A) the sensor platform, (B) the electromagnet, (C) the microscope and (D) the stimulation electrodes.*

5.4 Recording from hippocampal brain slice

In this paragraph, the process leading to the recording of neural signal arising from rat hippocampal slices is described. The results are then analyzed and discussed.

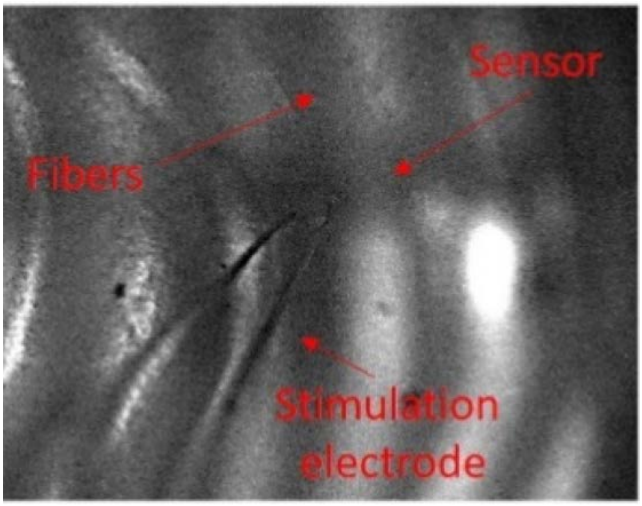

Figure 5.13: *Optical image of the brain slice under the workstation. The fibers and the electrodes were visible as well as the underlying sensors thank to the thinness of the slices.*

5.4.1 Stimulation and recording

The culture chamber was filled with ACSF and the hippocampal brain slice was put inside. The slice was positioned in such a way that the fibers were aligned to the sensors (Figure 5.13). Extracellular local field potentials were recorded using a borosilicate glass electrode (Kimble Chase) of 1-2 MΩ filled with artificial ACSF. Evoked post synaptic potential (EPSP) were provoked in granule cells layer in response to extracellular stimulation of the medial PP with a monopolar glass electrode filled with ACSF and connected with an isolated pulse stimulator (A-M Systems). The cells were stimulated with rectangular-shaped current pulses of intensity 150-500 μA and duration 150 μs.

In Figure 5.14 the LFP extracellular recording signal, averaged over 30 acquisitions, is presented. The artefact is shortly followed (after less than 1 ms) by the signal, which has a duration of approximately 2.4 ms. Two different biological signals can be clearly recognized following the artefact: the fast population spike and the very slow EPSP. The population spike arises from the collective response of the neuronal axons composing the fiber. The EPSP is caused by the presynaptic neuron releasing neurotransmitters from the bouton at the end of an axon into the synaptic cleft. The two signal have comparable amplitude, about 1 mV, but the population spike lasts only 2.4 ms, while the EPSP extends over 15 ms. Time durations are compatible with what discussed in Section LFP about the frequency range of the biological signal. It must be noted that the presence of the sensors does not influence the signal, which can be used to validate the magnetic platform.

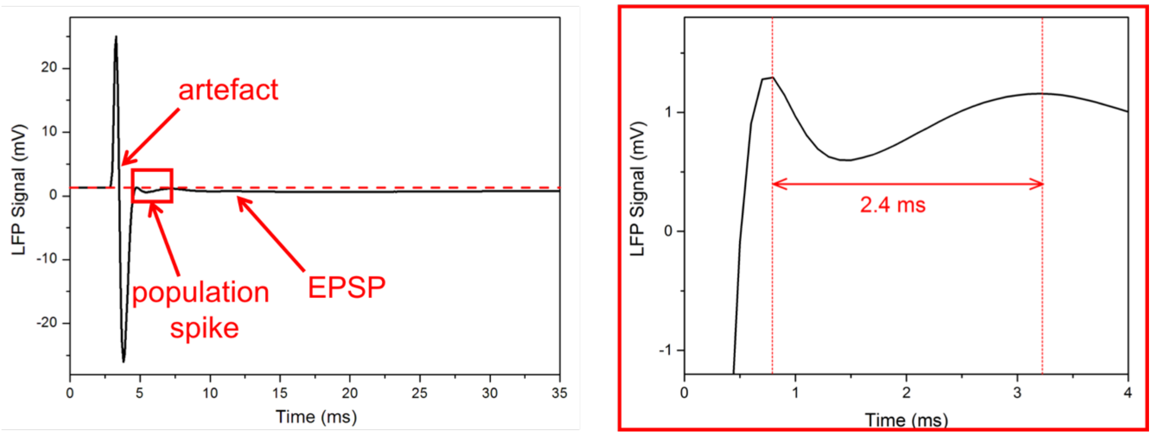

Figure 5.14: *LFP recording showing the artefact, the fast population spike and the slow excitatory postsynaptic potential (EPSP). On the right, the magnification of the population spike, which lasts about 2.4 ms.*

For the magnetic measurement, in order to minimize any interference raising from the stimulation signal, the chip and the power supplier were connected to a common ground. Unfortunately, the recording electrode was found to add a considerable amount of noise to the magnetic measurement thus it was removed from the biological solution after the preliminary LFP recordings. This made impossible to perform the electrical and magnetic measurements in parallel. The peristaltic pump as well needed to be switched off during the detection. In turn, all these expedients allowed us to obtain an excellent noise figure, well below 100 parts per million (ppm), calculated as the ratio between the standard deviation and the amplitude of the recorded signal.

The recording protocol consisted of a train of 32 pulses with a fixed period of 1.2s. For about 16 pulses, the magnetic field polarized the sensor in the best working point, afterwards the bias was manually switched off, bringing the sensor towards the saturation. The measurements were performed applying to the junction a voltage ranging from 10 to

80 mV at a modulation frequency of 40 kHz. The sampling period was 60 µs. The software read the variations of current flowing in the sensor, which were later converted in resistance values. All the recordings were performed under administration of BIC.

5.4.2 Analysis and results

The recorded data are shown in Figure 5.15, where a typical single trace acquired over 32 periods. The high ‘jump’ in the middle of the trace is due to the sudden removal of the polarizing magnetic field, bringing the sensor in the saturated condition (“control”). The large spikes come from the stimulation artefacts

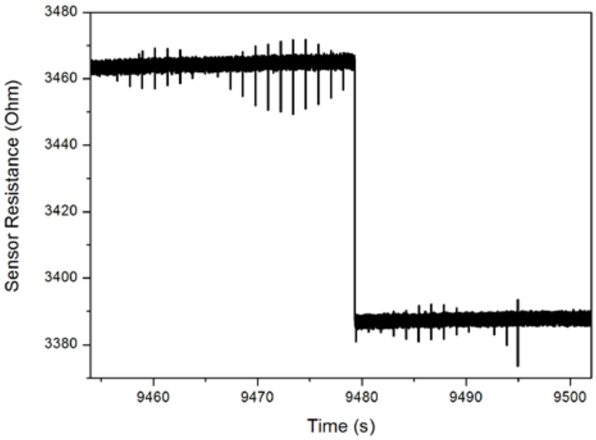

Figure 5.15: *Typical single trace of a measurement. The ‘jump’ in the middle is due to the sudden removal of the polarizing magnetic field.*

The reported data were then analyzed with an ad-hoc developed MATLAB function (see Appendix A). Taking as input the period of the pulse train, the sampling frequency and the data vector, the function readily returns the data averaged on a single period, obtaining a reduction of the noise by several times, as one can see in Figure 5.16. In this, the standard deviation of the signal passes from 0.36 Ω to 0.085 Ω upon averaging over 18 periods.

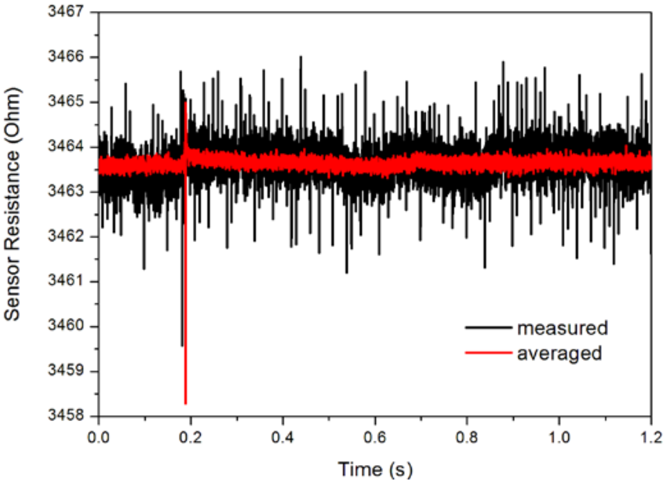

Figure 5.16: *Comparison of the noise before (black) and after (red) the averaging. The standard deviation goes from 0.36 Ω to 0.085 Ω upon averaging over 18 periods.*

As it can be noticed in the previous figures and in Figure 5.17, the artefacts are not of the same amplitude due to a sinusoidal modulation of frequency ≅ 20 mHz. Such modulation might arise from a beat between the frequencies of the stimulation and voltage bias signals. However, their amplitudes are comparable in the two configurations (with and without field), which means that such signals clearly arise from the capacitive coupling between the stimulation electrode and the sensor contact.

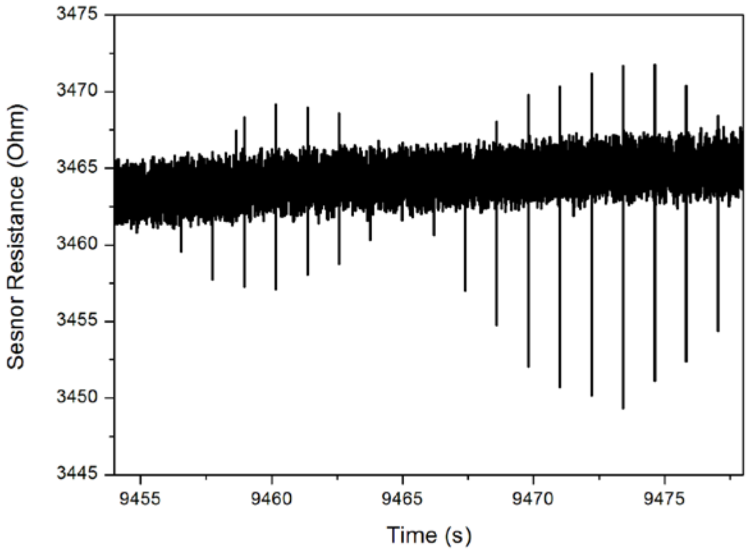

Figure 5.17: *Artefacts modulated by a sinusoidal disturbance of frequency ≅ 20 mHz.*

Furthermore, it is worth noting that the artefacts are not always visible. Since the platform records the current flowing in the sensors, it is sensitive to both the current from the bias voltage (V) and the current from capacitive i_{cap} coupling:

$$I = \frac{V}{R + \Delta R} + i_{cap} \tag{5.3}$$

where R is the nominal sensor's resistance and ΔR the variation due to magnetic detection. Thus, if the first term is high enough, the capacitive current becomes negligible. However, if the stimulation is very strong, the capacitive contribute can be relevant. On the other hand, the artefacts are not the object of our investigations, but they are just useful indicators of where to look for a biological signal. For example, the signal of Figure 5.17 was recorded from a sensor with a resistance of 3460 Ω applying a stimulation pulse of 400-µA. In this case the current from the bias voltage (80 mV applied) was 26 µA, well below the current injected in the system by the stimulation electrode and therefore the artefacts are well distinguishable. In the case of Figure 5.18, with a sensor resistance of only 815 Ω, a bias voltage of 40 mV and a stimulating pulse of 200 µA the artefact was not clearly visible. In this case indeed the weaker stimulation and the higher bias current (49 µA) make the first term in Eq 5.3 dominating.

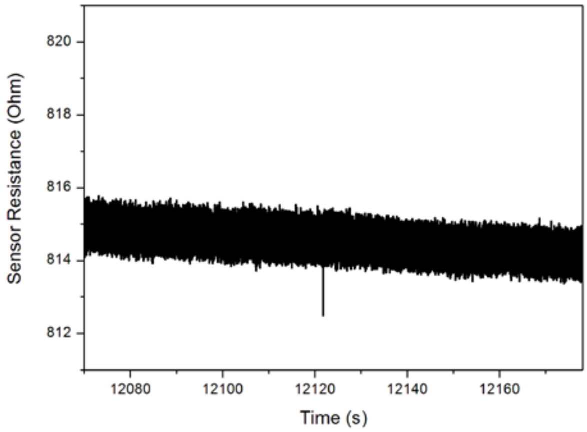

Figure 5.18: *Example of a trace where artefacts were absent.*

The most significant results are reported in the following.

Figure 5.19 reports a recording at 10 mV and 500-μA stimulation. In this case, the signal follows the artefact by 500 μs and lasts about 400 μs. In comparison to the LFP recording, the signal is too distant in time from the artefact and such duration is about 5-6 time shorter than the recorded one. Although this signal can have a biological origin, it is not so straightforward to associate it to the fast axon potential response. Furthermore, in this case the amplitude of the equivalent magnetic signal would be about 15 μT, which is again a too large value to exclude a significant capacitive contribute.

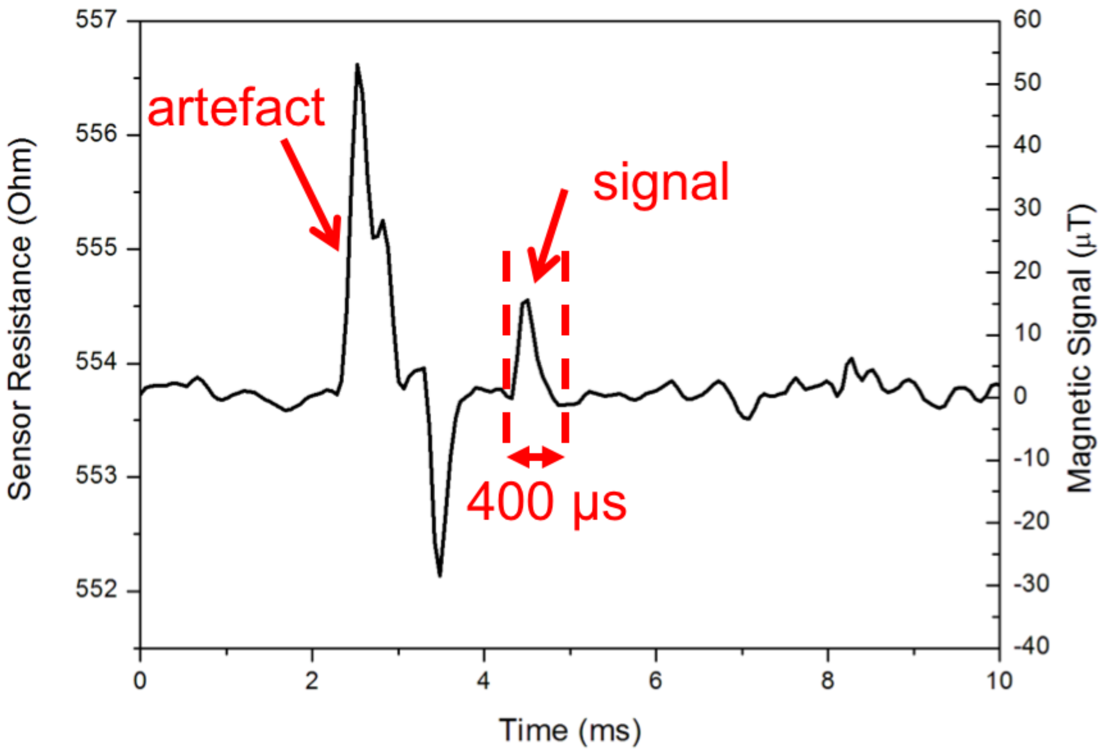

Figure 5.19: *Trace recorded at 40 mV, 500-μA stimulation and averaging over 30 periods. The signal follows the artifact by 500 μs and lasts about 400 μs.*

Figure 5.20 reports a recording at 65 mV and 400-µA stimulation. Immediately after the artifact, one can see a sort of bump in the sensor signal, which is absent in the control. This bump is partially incorporated in the artefacts and last about 1 ms. While the time duration is too short compared to the LFP-measured fast signal, the equivalent magnetic field amplitude of 1.2 µT could be comparable to what obtained by J. Amaral et al. [44]. However, also in this case it is difficult to assess the biological correspondence of the signal.

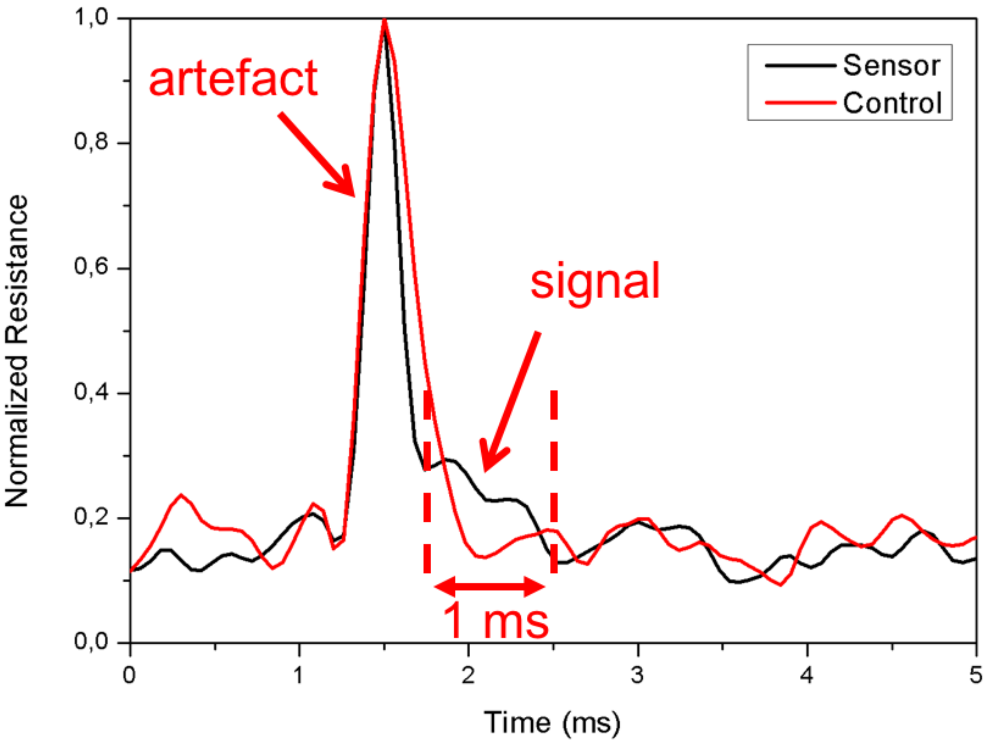

Figure 5.20: *Traces recorded at 65 mV, 400-µA stimulation and averaging over 16 periods. The signal is partially incorporated in the artefact, but is absent in the control. It last about 1 ms.*

Figure 5.21 shows a measurement recorded at 80 mV with 500-µA stimulation. One can see that immediately after the large artefact (less than 1ms) a small signal lasting about 3 ms and resembling the population spike appears. This peak has a signal-to-noise (SNR) equal to 5 that, converted in magnetic field, means a 5.5-µT amplitude. The noise level has been calculated as the standard deviation of the signal over about 13000 points. The time position and time duration thus can be compatible with the biological signal. Actually this signal is twice as big as what reported by J. Amaral et al. [44]. Then it is very likely that the signal was affected by some capacitive coupling. Moreover, one should note that the artefact disappears in the control measurements, therefore is difficult to draw a conclusion.

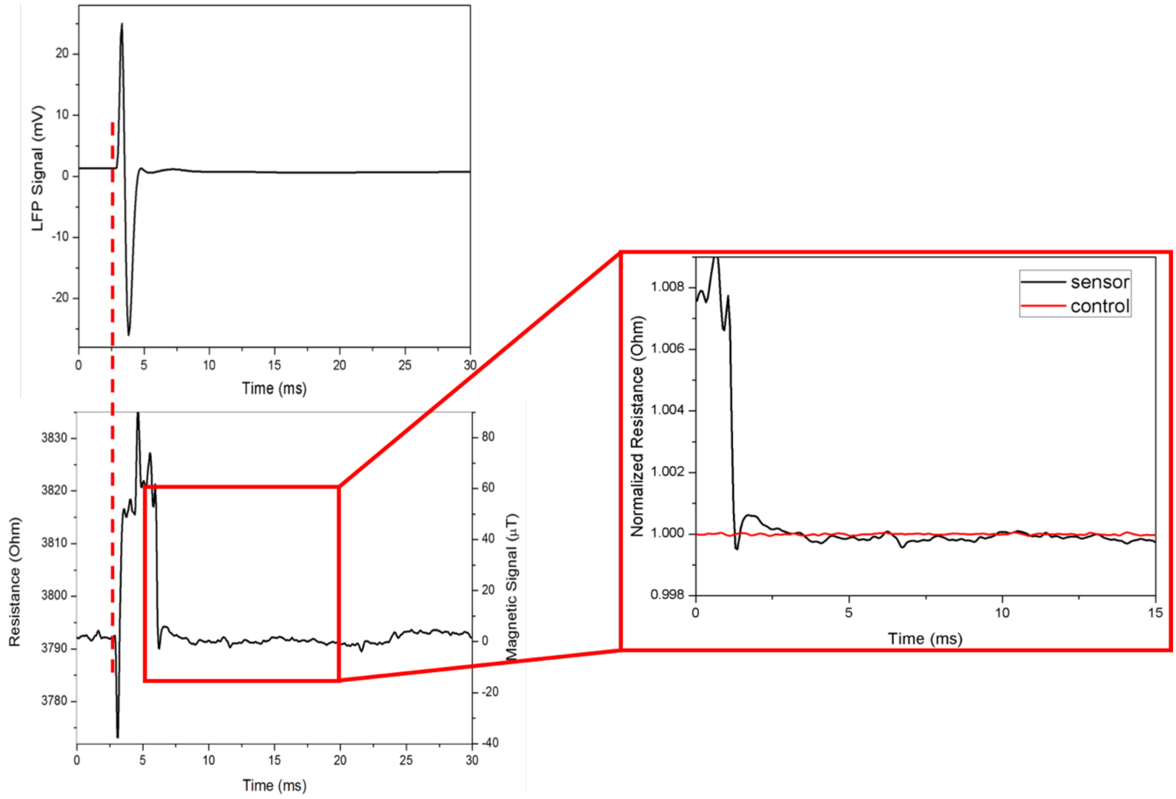

Figure 5.21: *Time comparison between the LFP recording and the magnetic measurements performed at 80 mV and 500-μA stimulation and averaged over 16 periods. A small peak is visible just after the artefact, which resembles the LFP signal.*

An additional cause of divergence is that the LFP measurements are not recorded in exact correspondence of the magnetic sensor and therefore the signal propagating in the biological medium can be distorted, either in time or intensity. The population spikes are fast, but they are strongly dampened during propagation, so that if the sensor is far apart from their origin, it can be not detected. Instead, the slow EPSPs can be considerably delayed in time since they depend on how many synapses are on the way, but, in turn, they are much less attenuated by the biological medium.

Due to the low statistics, however, it is currently not possible to confirm such signal to be the result of a magnetic detection and further work is needed.

5.5 Conclusions and perspectives

The possible reasons why we were not able to clearly detect the neuronal signal are many. First of all, each cut of a brain slice caused a layer of dead cells whose precise thickness was unknown (generally ~10 μm). This led to a substantial uncertainty on the number of neurons activated by the stimulation, which reflected on the impossibility to estimate the magnitude of the expected current. Furthermore, the slice was not perfectly in contact with the sensor then we did not know the exact distance between the sensor and the fibers (~10 μm), preventing a simulation of the magnetic field in correspondence of the active sensing area. However, some improvements and perspectives are envisaged.

In particular, four aspects were recognized as the ones with larger margins for improvements:

- The stimulation setup can be subject to a significant improvement, optimizing the parameters and the position of the stimulation.

- At present times, while for a single neuron well-known models are available, systems such as hippocampal brain slices are relatively less characterized. More accurate simulations will be very useful to understand the recorded signal.

- As an alternative, we could turn other regions of the brain, such as the cerebellum, or to simpler biological models, such as muscle cells since the bigger dimension yields larger signal and the simpler physiology allows a straightforward interpretation of the results.

- As enlightened by noise spectra in Chapter 4, the modulation of the magnetic field, and hence of the current, combined with narrowband measurements (integration over 1-Hz bandwidth) would allow to reach a resolution down to 5 nT. From the biological point of view, it is impossible to modulate the response of a neuron. In turn, such condition can be achieved with technological expedients. Nowadays, two different strategies are under investigations: flux concentrators and MEMS resonators. The former allows to enhance significantly the signal to detect, concentrating the magnetic field in a small gap around the active region of the sensor. Instead, MEMS can vibrate at high frequency enabling the modulation of the magnetic field. Therefore, growing the sensor's stack above such devices enables to shift the operating point to higher frequency getting rid of $^1/_f$ noise. Combining the techniques [91], it is possible to take advantage of both the results, greatly enhancing the detection effectiveness. The employment of such technologies is currently under study by the NaBiS group.

Chapter 6: Conclusions

The aim of this thesis work was the development of a magnetoresistive platform for the detection of signals arising from neuronal networks. In fact, the currents flowing in the axons generate also a magnetic field.

The first part of the work was devoted to the performance analysis, in terms of noise and minimum magnetic detectable field, of four selected sensors: two MgO-based magnetic tunneling junctions (MTJ-LOCSENS, MTJ-SPINBIOMED), a junction with an amorphous barrier (MTJ-AlOx) and a spin valve (GMR-SV). The noise measurements, performed with a cross-correlation spectrum analyzer, revealed that the MTJ-based devices exhibited the highest noise in the bandwidth of the biological signal (1 Hz-1 kHz) due to the flicker noise related to the tunneling barrier. However, weighting the noise spectra with the sensitivity significantly improved the sensors' performances. Despite having very good noise figures, the GMR-SV had a too scarce sensitivity to compete with the MTJ-based sensors. As a result, thanks to the MgO tunneling barrier, the MTJ-LOCSENS, which shows a TMR ratio of 27%, a sensitivity of 9.5%/mT and coercivity of 0.5 mT, turned out to be the most sensitive sensor achieving a 400-nT resolution on a 1 Hz-1 kHz bandwidth. This noise analysis gave the theoretical limit of detection of the sensors under investigation. To find out the actual resolution of the devices, we tried to simulate a bundle of neuronal axons by means of current lines fabricated on top of the sensors in which a current pulse could propagate. To carry out these measurements, a dedicated electronic platform was developed, since commercial electronics limited the performance of the sensors. These simulations substantially confirmed the theoretical results. Actually, some peculiarities were noticed for the MTJ-SPINBIOMED and MTJ-AlOx. The resolution of the former was found to be limited by the slow dynamics of magnetic domains. In turn, the latter was strongly affected by Random Telegraphic Noise (RTN) noise, which altered the measurements algorithm, resulting in a resolution below the theoretical limit.

In the second part of the thesis, the fabrication of MTJ sensors similar to the MTJ-LOCSENS was performed. The characteristic of these sensors were slighter improved with respect to the case of the MTJ-LOCSENS, giving rise to a TMR ratio of 27%, a sensitivity of 12.7%/mT and coercivity of 0.5 mT. Then, we moved to the realization of the platform for the *in-vitro* experiments on rat hippocampal slices. A compact acquisition setup, based on the same electronic platform used for the current lines measurements, was developed. This setup enabled the integration of the sensors in the setup used for electrophysiological recording. In this way, the first measurements of the neuronal signal from rat hippocampal brain slices were performed. In order to support the magnetic measurements, Local Field Potential (LFP) recordings were combined to magnetic measurements. The results were promising, with the presence of peaks in correspondence of the LFP signal. However, it should be noted that the measurements were not so reproducible and that the signal was strongly affected by a capacitive coupling due to the stimulation current. In fact, the biological medium acts as a dielectric between two electrodes, represented by the sensor's metallic paths and the stimulation electrode itself. Then an AC electrical bio-signal or the stimulation signal can pass through it, from one electrode to the other, independently form the magnetic response of the slice. In conclusion, due to the low statistics it was not possible to confirm such signal to be the result of a magnetic detection.

Further work will be done to improve the acquisition setup. On the biological side, the stimulation setup can be significantly optimized. Moreover, complex system such as hippocampal brain slices are relatively little characterized. More accurate simulations will be very useful to understand the recorded signal. As an alternative, other regions of the brain could be investigated, such as the cerebellum. From the technological point of view, measurements performed on narrowband could improve the ultimate sensitivity of the sensor, getting rid of the high flicker noise. From the biological point of view, it is impossible to modulate the response of a neuron. This is why two different strategies are under investigations: flux concentrators and MEMS resonators.

Appendix A

In this appendix, the MATLAB function employed to analyze the recorded data is described.

Each single acquisition consists of two parts: about 16 pulses are recorded with the sensor magnetically biased in the linear region of its characteristic, while the rest in the saturation region (“control” condition), upon switching off the magnetic bias. This sudden removal of the field results in an upward “jump” of the current signal recorded by the platform (Figure 5.17). The program must be able therefore to distinguish the two situations.

The function takes as input the period of the pulse train (in µs), the sampling rate (in µs) and the vector of data to analyze and returns two vectors, one for each configuration. The basic idea is to divide the data in many pieces corresponding to a single period of stimulation and then to average over all of them.

The program automatically finds the first artefact and starts averaging. To do so, average and standard deviation of the baseline are calculated. A point is deemed belonging to a peak if it is above or below the baseline of a quantity greater than a confidence value ‘conf’. Then, the program searches for the jump as a point 10 times larger than the confidence value above the baseline. All the data between these two points define a new vector. At this point, a matrix is defined, with a number of row equal to the number of point in a period and the number of columns equal to the number of period found in the new vector. The matrix is progressively filled with the data and the average over all the columns are performed, the result is a column vector containing the average over all the period. The same procedure is iterated for the points after the jump.

The whole code is reported below.

```
function [media1, media2] = tesi(periodo, samp, dati)

%Confidence level
lev = 6.07;
%Calculating the number of point in a period
ratio = periodo/samp;
numrighe = floor(ratio);

%Calculating mean and standard deviation of the baseline of the signal
avg = mean(dati(1:20000));
sigma = std(dati(1:20000));
%Confidence used to search for the first peak, expressed in unit of st.
dev.
conf = lev*sigma;

dim = size(dati,1);

%The first peak is defined as a point which is above or below the
baseline
```

```
%of a quantity 'conf'. The positon of the peak in the vector is recorded
as
%'point1'.
for k=2:dim;
    point1 = k-5;
    if (dati(k,1) > (avg+conf)) || (dati(k,1) < (avg-conf));
        break
    end
    if (k==dim);
       fprintf('Signal not found\n');
    end
end

%The second for loop identifies the jump as a point 10 times larger than
%'conf'. Its position is recorded in 'jump'.
for k=2:dim;
        jump = k;
        if (dati(k,1) > (avg+10*conf));
            break
        end
         if (k==dim);
            fprintf('Discontinuity not found\n');
        end
end

%Two new data vectors are built. The first contain all the points before
%the jump, the second all the points after it. the two matrix are
declared
%with a number of row equal to the number of point in a period and the
%number of columns equal to the number of period found in the new
vectors.
end1 = jump-170;
newdati1 = dati(point1:end1,1);
numcol1 = floor(size(newdati1,1)/numrighe);
matrix1 = zeros(numrighe, numcol1);

%The first matrix is built.
for i=1:numcol1;
    for j=1:numrighe;
        cont = round(j+ratio*(i-1));
        if (cont > size(newdati1));
            cont = cont-1;
        end
        matrix1(j,i) = newdati1(cont,1);
    end
end

%Before building the second matrix, a new search for a starting peak is
%performed.
point2 = jump+320;

%Average and st. dev. are recalculated for the new baseline.
avg2 = mean(dati(end-20000:end));
sigma2 = std(dati(end-20000:end));
conf2 = lev*sigma2;

%Searching the second starting poitn.
for k=point2:dim;
    start2 = k-5;
```

```
    if (dati(k,1) > (avg2+conf)) || (dati(k,1) < (avg2-conf2));
        break
    end
    if (k==dim);
       fprintf('Signal not found\n');
    end
end

%The second matrix is built.
newdati2 = dati(start2:end,1);
numcol2 = floor(size(newdati2,1)/numrighe);
matrix2 = zeros(numrighe, numcol2);


for i=1:numcol2;
    for j=1:numrighe;
        cont = round(j+ratio*(i-1));
        if (cont > size(newdati2));
            cont = cont-1;
        end
        matrix2(j,i) = newdati2(cont,1);
    end
end

%The averages over the columns are calculated, giving as a result two
%column vectors.
media1 = mean(matrix1, 2);
media2 = mean(matrix2, 2);
```

Bibliography

[1] D. E. Heim, J. Tsang, V. S. Speriosu, B. A. Gurney, M. L. Williams, and R. E. Fontana, “Design and Operation of Spin Valve Sensors,” *IEEE Trans. Magn.*, vol. 30, no. 2, pp. 316–321, 1994.

[2] E. Albisetti, D. Petti, F. Damin, M. Cretich, M. Bagnati, L. Sola, M. Chiari, and R. Bertacco, “Optimization of the bio-functionalized area of magnetic biosensors,” *Eur. Phys. J. B*, vol. 86, no. 6, pp. 3–7, 2013.

[3] M. Pannetier, C. Fermon, G. Le Goff, J. Simola, and E. Kerr, “Femtotesla magnetic field measurement with magnetoresistive sensors,” *Science (80-.).*, vol. 304, no. 5677, pp. 1648–1650, 2004.

[4] T. R. Mcguire and R. I. Potter, “Anisotropic Magnetoresistance in Ferromagnetic 3D Alloys,” *IEEE Trans. Magn.*, vol. 11, no. 4, pp. 1018–1038, 1975.

[5] V. Gehanno, P. P. Freitas, A. Veloso, J. Ferrira, B. Almeida, J. B. Soasa, A. Kling, J. C. Soares, and M. F. da Silva, “Ion beam deposition of Mn-Ir spin valves,” *IEEE Trans. Magn.*, vol. 35, no. 5, pp. 4361–4367, 1999.

[6] M. N. Baibich, J. M. Broto, A. Fert, F. N. Van Dau, F. Petroff, P. Eitenne, G. Creuzet, A. Friederich, and J. Chazelas, “Giant magnetoresistance of (001)Fe/(001)Cr magnetic superlattices,” *Phys. Rev. Lett.*, vol. 61, no. 21, pp. 2472–2475, 1988.

[7] T. Valet and A. Fert, “Theory of the perpendicular magnetoresistance in magnetic multilayers,” *Phys. Rev. B*, vol. 48, no. 10, pp. 7099–7113, 1993.

[8] N. Hasegawa, F. Koike, K. Ikarashi, M. Ishizone, M. Kawamura, Y. Nakazawa, A. Takahashi, H. Tomita, H. Iwasaki, and M. Sahashi, “Nano-oxide-layer specu- lar spin valve heads with synthetic pinned layer: Head performance and reliability,” *J. Appl. Phys.*, 2002.

[9] M. Lederman, “Performance of metallic antiferromagnets for use in spin-valve read sensors,” *IEEE Trans. Magn.*, vol. 35, no. 2 PART 1, pp. 794–799, 1999.

[10] A. Fert, “The present and the future of spintronics,” *Thin Solid Films*, vol. 517, no. 1, pp. 2–5, 2008.

[11] M. Julliere, “Tunneling between ferromagnetic films,” *Phys. Lett. A*, vol. 54, no. 3, pp. 225–226, 1975.

[12] S. Yuasa and D. D. Djayaprawira, “Giant tunnel magnetoresistance in magnetic tunnel junctions with a crystalline MgO(001) barrier,” *J. Phys. D. Appl. Phys.*, vol. 40, no. 21, p. R337, 2007.

[13] D. Wang, C. Nordman, J. M. Daughton, Z. Qian, and J. Fink, “70% TMR at room temperature for SDT sandwich junctions with CoFeB as free and reference layers,” *IEEE Trans. Magn.*, vol. 40, no. 4 II, pp. 2269–2271, 2004.

[14] M. Bowen, M. Bibes, A. Barthélémy, J. P. Contour, A. Anane, Y. Lemaître, and A. Fert, “Nearly total spin polarization in La2/3Sr1/3MnO3 from tunneling experiments,” *Appl. Phys. Lett.*, vol. 82, no. 2, pp. 233–235, 2003.

[15] W. H. Butler, X.-G. Zhang, T. C. Schulthess, and J. M. MacLaren, “Spin-dependent

tunneling conductance of Fe|MgO|Fe sandwiches," *Phys. Rev. B*, vol. 63, no. 5, p. 54416, 2001.

[16] J. Mathon and A. Umerski, "Theory of tunneling magnetoresistance of an epitaxial Fe/MgO/Fe(001) junction," *Phys. Rev. B*, vol. 63, no. 22, p. 220403, 2001.

[17] S. Ikeda, J. Hayakawa, Y. Ashizawa, Y. M. Lee, K. Miura, H. Hasegawa, M. Tsunoda, F. Matsukura, and H. Ohno, "Tunnel magnetoresistance of 604% at 300 K by suppression of Ta diffusion in CoFeBMgOCoFeB pseudo-spin-valves annealed at high temperature," *Appl. Phys. Lett.*, vol. 93, no. 8, pp. 67–70, 2008.

[18] R. Ferreira, E. Paz, P. P. Freitas, J. Ribeiro, J. Germano, and L. Sousa, "2-Axis Magnetometers Based on Full Wheatstone Bridges Incorporating Magnetic Tunnel Junctions Connected in Series," *IEEE Trans. Magn.*, vol. 48, no. 11, pp. 4107–4110, 2012.

[19] F. A. Cardoso, L. S. Rosado, F. Franco, R. Ferreira, E. Paz, S. F. Cardoso, P. M. Ramos, M. Piedade, and P. J. P. Freitas, "Improved magnetic tunnel junctions design for the detection of superficial defects by eddy currents testing," *IEEE Trans. Magn.*, vol. 50, no. 11, pp. 2–5, 2014.

[20] J. Valadeiro, S. Cardoso, R. Macedo, A. Guedes, J. Gaspar, and P. P. Freitas, "Hybrid Integration of Magnetoresistive Sensors with MEMS as a Strategy to Detect Ultra-Low Magnetic Fields," *Micromachines*, 2016.

[21] D. C. Leitao, E. Paz, A. V. Silva, A. Moskaltsova, S. Knudde, F. L. Deepak, R. Ferreira, S. Cardoso, and P. P. Freitas, "Nanoscale magnetic tunnel junction sensing devices with soft pinned sensing layer and low aspect ratio," *IEEE Trans. Magn.*, vol. 50, no. 11, 2014.

[22] L. T. Hall, G. C. G. Beart, E. A. Thomas, D. A. Simpson, L. P. McGuinness, J. H. Cole, J. H. Manton, R. E. Scholten, F. Jelezko, J. Wrachtrup, S. Petrou, and L. C. L. Hollenberg, "High spatial and temporal resolution wide-field imaging of neuron activity using quantum NV-diamond.," *Sci. Rep.*, vol. 2, p. 401, 2012.

[23] L. Caruso, "Giant magnetoresistance based sensors for local magnetic detection of neuronal currents Université Pierre et Marie Curie," 2015.

[24] Breedlove and Watson, *Biological Psychology*. 2013.

[25] M. R. Cohen and A. Kohn, "Measuring and interpreting neuronal correlations.," *Nat. Neurosci.*, vol. 14, no. 7, pp. 811–819, 2011.

[26] S. Grillner, H. Markram, E. De Schutter, G. Silberberg, and F. E. N. LeBeau, "Microcircuits in action - From CPGs to neocortex," *Trends Neurosci.*, vol. 28, no. 10, pp. 525–533, 2005.

[27] B. J. Roth and J. P. Wikswo, "The magnetic field of a single axon. A comparison of theory and experiment.," *Biophys. J.*, vol. 48, no. 1, pp. 93–109, 1985.

[28] D. B. MacHattie., "Investigation of the Evoked Magnetic Action Flux of Skeletal Muscle," McMaster University, 1987.

[29] G. Buzsáki, "Large-scale recording of neuronal ensembles.," *Nat. Neurosci.*, vol. 7, no. 5, pp. 446–51, 2004.

[30] E. Niedermayer and F. Lopes da Silva, "Electroencephalography: basic principles, clinical applications and related fields," 1982.

[31] G. Pfurtscheller and F. H. Lopes Da Silva, "Event-related EEG/MEG

synchronization and desynchronization: Basic principles," *Clin. Neurophysiol.*, vol. 110, no. 11, pp. 1842–1857, 1999.

[32] M. Pusch and E. Neher, "No Title," 1990.

[33] F. Heer, W. Franks, A. Blau, S. Taschini, C. Ziegler, A. Hierlemann, and H. Baltes, "CMOS microelectrode array for the monitoring of electrogenic cells," *Biosens. Bioelectron.*, vol. 20, no. 2, pp. 358–366, 2004.

[34] L. Berdondini, P. D. Van Der Wal, O. Guenat, N. F. De Rooij, M. Koudelka-Hep, P. Seitz, R. Kaufmann, P. Metzler, N. Blanc, and S. Rohr, "High-density electrode array for imaging in vitro electrophysiological activity," *Biosens. Bioelectron.*, vol. 21, no. 1, pp. 167–174, 2005.

[35] S. Vassanelli and P. Fromherz, "Transistor probes local potassium conductances in the adhesion region of cultured rat hippocampal neurons.," *J. Neurosci.*, vol. 19, no. 16, pp. 6767–73, 1999.

[36] F. Gullo, A. Maffezzoli, E. Dossi, M. Lecchi, and E. Wanke, "Classifying heterogeneity of spontaneous up-states: A method for revealing variations in firing probability, engaged neurons and Fano factor," *J. Neurosci. Methods*, vol. 203, no. 2, pp. 407–417, 2012.

[37] B. J. Baker, E. K. Kosmidis, D. Vucinic, C. X. Falk, L. B. Cohen, M. Djurisic, and D. Zecevic, "Imaging brain activity with voltage- and calcium-sensitive dyes," *Cell Mol Neurobiol*, vol. 25, no. 2, pp. 245–282, 2005.

[38] V. S. Zotev, A. N. Matlachov, P. L. Volegov, H. J. Sandin, M. A. Espy, J. C. Mosher, A. V. Urbaitis, S. G. Newman, and R. H. Kraus, "Multi-channel SQUID system for MEG and ultra-low-field MRI," *IEEE Trans. Appl. Supercond.*, vol. 17, no. 2, pp. 839–842, 2007.

[39] D. Cohen and B. N. Cuffin, "Demonstration of useful differences between magnetoencephalogram and electroencephalogram," *Electroencephalogr. Clin. Neurophysiol.*, vol. 56, no. 1, pp. 38–51, 1983.

[40] J. F. Barry, M. J. Turner, J. M. Schloss, D. R. Glenn, Y. Song, M. D. Lukin, H. Park, and R. L. Walsworth, "Optical magnetic detection of single-neuron action potentials using quantum defects in diamond," *arXiv:1602.01056 [cond-mat, physics:physics, physics:quant-ph, q-bio]*, 2016.

[41] A. Cooper, E. Magesan, H. N. Yum, and P. Cappellaro, "Time-resolved magnetic sensing with electronic spins in diamond," *Nat Commun*, vol. 5, p. 3141, 2014.

[42] P. P. Freitas, R. Ferreira, S. Cardoso, and F. Cardoso, "Magnetoresistive sensors," *J. PhysicsCondensed Matter*, vol. 19, no. 16, p. 165221, 2007.

[43] P. P. Sharma, E. Albisetti, M. Massetti, M. Scolari, C. La Torre, M. Monticelli, M. Leone, F. Damin, G. Gervasoni, G. Ferrari, F. Salice, E. Cerquaglia, G. Falduti, M. Cretich, E. Marchisio, M. Chiari, M. Sampietro, D. Petti, and R. Bertacco, "Integrated platform for detecting pathogenic DNA via magnetic tunnelling junction-based biosensors," *Sensors Actuators B Chem.*, vol. 242, pp. 280–287, 2016.

[44] J. Amaral, S. Cardoso, P. P. Freitas, and A. M. Sebastio, "Toward a system to measure action potential on mice brain slices with local magnetoresistive probes," *J. Appl. Phys.*, vol. 109, no. 7, pp. 2009–2012, 2011.

[45] P. P. Sharma, G. Gervasoni, E. Albisetti, F. D'Ercoli, M. Monticelli, D. Moretti, N.

Forte, G. Ferrari, P. Baldelli, M. Sampietro, F. Benfenati, R. Bertacco, and D. Petti, “TOWARDS A MAGNETORESISTIVE PLATFORM FOR NEURAL SIGNAL RECORDING,” *AIP Adv.*

[46] B. Dieny, V. S. Speriosu, S. S. P. Parkin, B. A. Gurney, D. R. Wilhoit, and D. Mauri, “Giant magnetoresistive in soft ferromagnetic multilayers,” *Phys. Rev. B*, vol. 43, no. 1, pp. 1297–1300, 1991.

[47] D. J. Griffiths, *Introduction to Quantum Mechanics*. 2012.

[48] R. Stratton, “Volt-current characteristics for tunneling through insulating films,” *J. Phys. Chem. Solids*, vol. 23, no. 9, pp. 1177–1190, 1962.

[49] W. F. Brinkman, R. C. Dynes, and J. M. Rowell, “Tunneling conductance of asymmetrical barriers,” *J. Appl. Phys.*, vol. 41, no. 5, pp. 1915–1921, 1970.

[50] J. G. Simmons, “Generalized Formula for the Electric Tunnel Effect between Similar Electrodes Separated by a Thin Insulating Film,” *J. Appl. Phys.*, vol. 34, no. 6, pp. 1793–1803, 1963.

[51] N. F. Mott, “The Electrical Conductivity of Transition Metals,” *Proc. R. Soc. A Math. Phys. Sci.*, vol. 153, no. 880, pp. 699–717, 1936.

[52] Y. Jang, C. Nam, J. Y. Kim, B. K. Cho, Y. J. Cho, and T. W. Kim, “Magnetic field sensing scheme using CoFeB/MgO/CoFeB tunneling junction with superparamagnetic CoFeB layer,” *Appl. Phys. Lett.*, vol. 89, no. 16, 2006.

[53] Y. S. Choi, K. Tsunekawa, Y. Nagamine, and D. Djayaprawira, “Transmission electron microscopy study on the polycrystalline CoFeBMgOCoFeB based magnetic tunnel junction showing a high tunneling magnetoresistance, predicted in single crystal magnetic tunnel junction,” *J. Appl. Phys.*, vol. 101, no. 1, 2007.

[54] S. Zhang, P. Levy, a. Marley, and S. Parkin, “Quenching of Magnetoresistance by Hot Electrons in Magnetic Tunnel Junctions,” *Phys. Rev. Lett.*, vol. 79, no. 19, pp. 3744–3747, 1997.

[55] J. Hayakawa, S. Ikeda, F. Matsukura, H. Takahashi, and H. Ohno, “Dependence of giant tunnel magnetoresistance of sputtered CoFeB/MgO/CoFeB magnetic tunnel junctions on MgO barrier thickness and annealing temperature,” *Japanese J. Appl. Physics, Part 2 Lett.*, vol. 44, no. 16–19, 2005.

[56] G. Binasch, P. Grünberg, F. Saurenbach, and W. Zinn, “Enhanced magnetoresistance in layered magnetic structures with antiferromagnetic interlayer exchange,” *Phys. Rev. B*, vol. 39, no. 7, pp. 4828–4830, 1989.

[57] C. Chappert, A. Fert, and F. N. Van Dau, “The emergence of spin electronics in data storage.,” *Nat. Mater.*, vol. 6, no. 11, pp. 813–823, 2007.

[58] J. Bass and W. P. Pratt, “Current-perpendicular (CPP) magnetoresistance in magnetic metallic multilayers,” *J. Magn. Magn. Mater.*, vol. 200, no. 1, pp. 274–289, 1999.

[59] B. Dieny, “Models in spintronics,” no. Part I. Timisoara, 2009.

[60] A. Barthélémy, A. Fert, J. P. Contour, M. Bowen, V. Cros, J. M. De Teresa, A. Hamzic, J. C. Faini, J. M. George, J. Grollier, F. Montaigne, F. Pailloux, F. Petroff, and C. Vouille, “Magnetoresistance and spin electronics,” *J. Magn. Magn. Mater.*, vol. 242–245, no. PART I, pp. 68–76, 2002.

[61] A. Barthelemy and A. Fert, “Theory of the magnetoresistance in magnetic

multilayers: Analytical expression from a semiclassical approach," *Phys. Rev. B*, vol. 43, no. 16, pp. 124–129, 1991.

[62] R. E. Camley and J. Barnàs, "Theory of Giant Magnetoresistance Effects in Magnetic Layered Structures with Antiferromagnetic Coupling," vol. 63, no. 6, pp. 664–667, 1989.

[63] M. Johnson and R. H. Silsbee, "Coupling of electronic charge and spin at a ferromagnetic-paramagnetic metal interface," *Phys. Rev. B*, vol. 37, no. 10, pp. 5312–5325, 1988.

[64] J. Cao, J. Kanak, T. Stobiecki, P. Wisniowski, and P. P. Freitas, "Effect of buffer layer texture on the crystallization of COFeB and on the tunnel magnetoresistance in MGO based magnetic tunnel junctions," *IEEE Trans. Magn.*, vol. 45, no. 10, pp. 3464–3466, 2009.

[65] H. C. Chung, Y. H. Lee, and S. R. Lee, "Effect of capping layer on the crystallization of amorphous CoFeB," *Phys. Status Solidi Appl. Mater. Sci.*, vol. 204, no. 12, pp. 3995–3998, 2007.

[66] Y. M. Lee, J. Hayakawa, S. Ikeda, F. Matsukura, and H. Ohno, "Giant tunnel magnetoresistance and high annealing stability in CoFeB/MgO/CoFeB magnetic tunnel junctions with synthetic pinned layer," *Appl. Phys. Lett.*, vol. 89, no. 4, pp. 1–17, 2006.

[67] E. Albisetti, "Magnetic tunneling junctions for biosensing and antiferromagnet-based spintronic devices," Politecnico di Milano, 2014.

[68] J. Nogues, I. K. Schüller, J. Nogués, and I. K. Schuller, "Exchange bias," *J. Magn. Magn. Mater.*, vol. 192, no. 2, p. 203, 1999.

[69] W. H. Meiklejohn and C. P. Bean, "New Magnetic Anisotropy," *Phys. Rev. Lett.*, vol. 105, no. 5, pp. 904–913, 1957.

[70] M. Finazzi, "Interface coupling in a ferromagnet/antiferromagnet bilayer," *Phys. Rev. B*, vol. 69, no. 6, p. 64405, 2004.

[71] S. . et al. Scholl, A.; Nolting, F.; Seo, J.W.; Ohldag, H.; Stohr, J.; Raoux, "Domain-size-dependent exchange bias in Co/LaFeO3," *Appl. Phys. Lett. 85(18)4085–4087, 2004.*, 2008.

[72] P. Grünberg, R. Schreiber, Y. Pang, U. Walz, M. B. Brodsky, and H. Sowers, "Layered magnetic structures: Evidence for antiferromagnetic coupling of Fe layers across Cr interlayers," *J. Appl. Phys.*, vol. 61, no. 8, pp. 3750–3752, 1986.

[73] S. S. P. Parkin, N. More and K. P. Roche, "Letters.," *Phys. Rev. Lett.*, vol. 23, no. 2, p. 130, 1990.

[74] M. Stiles, "Exchange coupling in magnetic heterostructures," *Phys. Rev. B*, vol. 48, no. 10, pp. 7238–7258, 1993.

[75] P. Bruno, "Magnetic Coupling," vol. 52, no. 1, 1995.

[76] J. Fassbender, F. Nörtemann, R. L. Stamps, R. E. Camley, B. Hillebrands, G. Güntherodt, and S. S. P. Parkin, "Oscillatory interlayer exchange coupling of Co/Ru multilayers investigated by Brillouin light scattering," *Phys. Rev. B*, vol. 46, no. 9, pp. 5810–5813, 1992.

[77] I. K. S. J. Eisenmenger, "Overcoming thermal fluctuations," *Nat. Mater.*, vol. 2, pp. 437–438, 2003.

[78] W. Shen, B. D. Schrag, A. Girdhar, M. J. Carter, H. Sang, and G. Xiao, “Effects of superparamagnetism in MgO based magnetic tunnel junctions,” *Phys. Rev. B - Condens. Matter Mater. Phys.*, vol. 79, no. 1, pp. 2–5, 2009.

[79] G. Bertotti, *Hysteresis in Magnetism: For Physicists, Materials Scientists, and Engineers*. Academic Press, 1998.

[80] F. Cardoso, “Design, optimization and integration of magnetoresistive biochips,” Instituto Superior Técnico, Lisbon, Portugal, 2010.

[81] H. Nyquist, “Thermal agitation of electric charge in conductors,” *Phys. Rev.*, vol. 32, no. 1, pp. 110–113, 1928.

[82] Z. Q. Lei, G. J. Li, W. F. Egelhoff, P. T. Lai, and P. W. T. Pong, “Review of noise sources in magnetic tunnel junction sensors,” *IEEE Trans. Magn.*, vol. 47, no. 3, pp. 602–612, 2011.

[83] J. G. Zhu, “Thermal magnetic noise and spectra in spin valve heads,” *J. Appl. Phys.*, vol. 91, no. 10 I, pp. 7273–7275, 2002.

[84] W. F. Egelhoff, P. W. T. Pong, J. Unguris, R. D. McMichael, E. R. Nowak, A. S. Edelstein, J. E. Burnette, and G. A. Fischer, “Critical challenges for picoTesla magnetic-tunnel-junction sensors,” *Sensors Actuators, A Phys.*, vol. 155, no. 2, pp. 217–225, 2009.

[85] F. N. Hooge, “1/F Noise,” *Phys. B+C*, vol. 83, no. 1, pp. 14–23, 1976.

[86] C. Ren, X. Liu, B. Schrag, and G. Xiao, “Low-frequency magnetic noise in magnetic tunnel junctions,” *Phys. Rev. B*, vol. 69, no. 10, pp. 1–5, 2004.

[87] S. Kogan, *Electronic noise and fluctuations in solids*. 2008.

[88] G. C. Han, B. Y. Zong, P. Luo, and C. C. Wang, “Magnetic field dependence of low frequency noise in tunnel magnetoresistance heads,” *J. Appl. Phys.*, vol. 107, no. 9, p. 09C706, 2010.

[89] M. Sampietro, L. Fasoli, and G. Ferrari, “Spectrum analyzer with noise reduction by cross-correlation technique on two channels,” *Rev. Sci. Instrum.*, vol. 70, no. 5, pp. 2520–2526, 1999.

[90] G. Bagnati, “No Title,” Politecnico di Milano, 2015.

[91] J. Valadeiro, S. Cardoso, R. Macedo, A. Guedes, J. Gaspar, and P. Freitas, “Hybrid Integration of Magnetoresistive Sensors with MEMS as a Strategy to Detect Ultra-Low Magnetic Fields,” *Micromachines*, vol. 7, no. 5, p. 88, 2016.

[92] P. Wisniowski, J. M. Almeida, and P. P. Freitas, “1 / f Magnetic Noise Dependence on Free Layer Thickness in,” *Current*, vol. 44, no. 11, pp. 2551–2553, 2008.

[93] J. Amaral, V. Pinto, T. Costa, J. Gaspar, R. Ferreira, E. Paz, S. Cardoso, and P. P. Freitas, “Integration of TMR sensors in silicon microneedles for magnetic measurements of neurons,” *IEEE Trans. Magn.*, vol. 49, no. 7, pp. 3512–3515, 2013.

[94] N. A. Stutzke, S. E. Russek, D. P. Pappas, and M. Tondra, “Low-frequency noise measurements on commercial magnetoresistive magnetic field sensors,” *J. Appl. Phys.*, vol. 97, no. 10, pp. 2003–2006, 2005.

[95] M. Scolari, “Magnetoresistive sensors for biological applications,” Politecnico di Milano, 2015.

[96] V. Bane, M. Lehane, M. Dikshit, A. O’Riordan, and A. Furey, “Tetrodotoxin: Chemistry, toxicity, source, distribution and detection,” *Toxins (Basel).*, vol. 6, no.

2, pp. 693–755, 2014.

[97] F. Bremer, “Considérations sur l’origine et la nature des ‘ondes’ cérébrales,” *Electroencephalogr. Clin. Neurophysiol.*, vol. 1, no. 1–4, pp. 177–193, 1949.

[98] G. H. Bishop, “THE INTERPRETATION OF CORTICAL POTENTIALS,” vol. 221, pp. 374–376, 1982.

[99] M. R. Klee, “Cross-Correlation Analysis of Electroencephalographic Potentials and Slow Membrane Transients Abstract.,” no. X 760, pp. 519–521.

[100] A. Destexhe and C. Bedard, “Local field potential,” *Scholarpedia*, 2013.

[101] E. Ferrea, a Maccione, L. Medrihan, T. Nieus, D. Ghezzi, P. Baldelli, F. Benfenati, and L. Berdondini, “Large-scale, high-resolution electrophysiological imaging of field potentials in brain slices with microelectronic multielectrode arrays.,” *Front. Neural Circuits*, vol. 6, no. November, p. 80, 2012.